WAVE CHARACTERISTICS OF TSUNAMIS GENERATED BY LANDSLIDES OF VARYING SIZE AND MOBILITY

by

Gemma Kate Bullard

A thesis submitted to the Department of Civil Engineering

In conformity with the requirements for

the degree of Doctorate of Philosophy

Queen's University

Kingston, Ontario, Canada

(June, 2018)

Abstract

Landslide generated tsunamis are a natural phenomenon, capable of causing catastrophic consequences at the site of impact as well as some kilometers away. In order to increase understanding of these hazards, a series of laboratory experiments were conducted in a large-scale flume investigate the wave characteristics in the near-field and far-field based on a variety of landslides.

The first objective is to examine the difference between the near-field maximum wave amplitude generated by highly mobile (water) and dry granular landslides. The results indicate that quantifying time and length scales are imperative in order to accurately estimate the maximum amplitude for highly mobile flows. The relationship between the time and length scales has a direct influence on the wave amplitude. The dry granular landslide decelerates much faster and therefore produce a smaller near-field maximum wave amplitude than those produced by highly mobile flows.

The second objective is to investigate the relationship between near-field wave shape of an impulse generated wave and the landslide properties. Quantifying the wave shape in terms of asymmetry allowed for the development of a novel framework, which provides a time-series for an impulse wave generated by a landslide with certain characteristics of thickness and velocity.

The third objective explores the near-field maximum wave amplitude generated by a higher mobility granular flow. The impulse waves generated in this study were in between the amplitude of the dry granular and highly mobile flows previously tested. This indicates that mobility can be quantified using the relationship between the time and length scales, and impulse waves generated by the highly mobile (water) flows is an accurate upper-bound of mobility.

Co-Authorship

This thesis is comprised of primarily original work by the author. Chapters 2, 3, 4 and 5 are adapted versions of manuscripts in preparation for submission to journals. This work has also inspired two conference papers, which are also listed herein.

Bullard, G.K., Mulligan, R.P., and Take, W.A. (2018a). Experimental analysis of tsunamis generated by the impact of landslides with high mobility. Submission to *Coastal Engineering*.

Bullard, G.K., Mulligan, R.P., and Take, W.A. (2018b). A novel framework to quantify the shape of landslide-generated tsunamis using wave asymmetry. Submitted to *Journal of Geophysical Research-Oceans*.

Bullard, G.K., Take, W.A., and Mulligan, R.P. (2018c). Influences of time and length scales on waves generated by dry granular landslides. In preparation for submission to *Coastal Engineering Journal*.

Bullard, G.K., Mulligan, R.P., and Take, W.A. (2018d). Waves generated from highly mobile saturated granular flows. In preparation for submission to *Landslides*.

Mulligan, R.P., Take, W.A., and Bullard, G.K. (2018). Landslide generated tsunamis: new laboratory experiments and theoretical developments. CSCE in Fredericton, Canada, June 13-16.

Mulligan, R.P., Take, W.A., and Bullard, G.K. (2018). Modelling tsunami from landslides with different mobility, *Proc*. Coastlab18, Santander, Spain, May 22-26.

Acknowledgements

Queen's Staff: Thank you very much for everything you've done for me to help me get to this point. Special shout out to Willie and Graeme on 'Main Campus', thank you for putting up with me and my disaster of a work area for three years and making sure I stay safe ☺

QWBB: Thanks for letting an ole' gal like me tag along, we made some great memories together.

Ellis 101 and friends: Thank you all so very much for allowing me to con you into thinking shoveling gravel all day was a good idea. I literally couldn't have done it without you. Thanks to all the Civil intramurals for giving me a nice break from the frustrations of research. To Innerboob WaterYolo: we're still undefeated in my books.

Phin: Thank you for being the highlight of most of my days. You always manage to put a smile on my face (despite your rapid mood swings and reluctance to share). Keep on working hard and don't ever let anyone tell you that you need to colour in between the lines.

Ryley and Paige: I think I could write another 100 pages trying to say thank you for absolutely everything (draft pending). You have constantly been such a positive influence on my life and fantastic role models and mentors. Thank you for keeping me on the straight and narrow and for always making sure I stay humble.

Family: Thank you for giving me room to grow and always being there when I needed you. Your unwavering faith and support is the only reason I am here today.

Anna-belle: Thank you for helping me take my mind of off work and towards the next adventure.

Ryan and Andy: An end to a whirlwind of an adventure! Sorry not sorry it wasn't longer. You've encouraged me to do so much critical thinking I've started to question my own identity.

Table of Contents

List of Figures

List of Tables

List of Acronyms

2D: Two-dimensional

3D: Three-dimensional

COM: Centre of mass

F1-F2: Indicates the location of the FARO Focus Laser Scanner for each scan

HH10: Equation 2.5 in this document

HM: High mobility

LB: Low mobility

MT17: Equation 2.12 in this document

P1-P9: Indicates wave probe location where P1 is the nearest to the impact zone and P9 is the farthest

PB: Positively buoyant

PIV: Particle Image Velocimetry

PVC: Polyvinyl chloride

RMSE: Root mean squared error

SWL: Still water level

vec: Vectrino

Z15: Equation 2.9 in this document

List of Symbols

A	Horizontal stretching factor for leading edge of the wave until the wave crest	[-]
$\bar{a}$	Near-field maximum amplitude averaged for each source volume	[m]
A_{HH10}	Predicted near-field maximum amplitude based on HH10	[-]
a_m	Maximum wave amplitude	[m]
A_m	Relative maximum wave amplitude ($A_m=a_m/h$)	[-]
a_q	Maximum wave amplitude from quadratic equation	[m]
A_q	Relative maximum wave amplitude from MT17 ($A_q=a_q/h$)	[-]
$a_{q,max}$	Maximum amplitude assuming maximum velocity relationship	[m]
$A_{q,max}$	Relative amplitude assuming maximum velocity relationship ($A_{q,max}=a_{q,max}/h$)	[-]
As	Wave asymmetry	[-]
As_{P1}	Wave asymmetry measured at P1 at *x*= 1.9 m	[-]
As_{P2}	Wave asymmetry measured at P2 at *x*= 3.1 m	[-]
B	Horizontal stretching factor for trailing edge of the wave	[-]
b	Landslide width	[m]
c_s	Wave speed	[ms^{-1}]
e	Void ratio	[-]
F	Landslide Froude number ($F = v_s/\sqrt{gh}$)	[-]
g	Gravitational acceleration	[m^2s^{-1}]
h	Water depth	[m]
h_{cr}	Critical water depth	[m]
H_b	Breaking wave height	[m]
l	Length	[m]
L_e	Effective length of forcing until wave release	[m]
L_m	Total landslide runout distance of granular material	[m]
M	Relative landslide mass ($M = m_s/(\rho_w bh^2)$)	[-]
M_s	Landslide momentum flux	[Pa]
m_s	Landslide mass	[kg]
n	Porosity	[-]
P	Impulse product parameter	[-]
P_s	Impulse product parameter for PB material calculated using thickness	[-]
$P_{\Delta t}$	Impulse product parameter for PB material calculated using time	[-]

R	Maximum horizontal distance of submerged bubble plume	[m]
s	Landslide thickness	[m]
S	Relative landslide thickness ($S = s/h$)	[-]
$\bar{s}$	Average landslide thickness	[m]
t	Time	[s]
Δt_e	Effective time until wave release	[s]
Δt_{M75}	Time for 75% of the landslide momentum to impact the reservoir	[s]
t_{peak}	Time zeroed such that the peak represents t = 0 s	[s]
Δt_s	Length of time until s < 0.008 m	[s]
u	Fluid velocity measured at z = 0.012 m and x = 3 m	[ms^{-1}]
u_m	Maximum fluid velocity measured at z = 0.012 m and x = 3 m	[ms^{-1}]
V	Landslide source volume	[m^3]
v	Submerged landslide velocity	[ms^{-1}]
v_s	Landslide velocity	[ms^{-1}]
$\bar{v_s}$	Average landslide velocity	[ms^{-1}]
x	Horizontal distance	[m]
Δx	Change in horizontal position	[m]
x_b	Horizontal distance until initially breaking waves become solitary waves	[m]
z	Vertical distance where z = 0 m at flume base	[m]
α	Impact angle	[°]
η	Water surface elevation	[m]
η_1	Water surface elevation for the leading edge of the wave	[m]
η_2	Water surface elevation for the crest and tail of the wave	[m]
ι_s	Mobility factor	[-]
μ	Dynamic viscosity	[Pa·s]
ρ	Water density	[kgm^{-3}]
ρ_s	Landslide density	[kgm^{-3}]
φ	Impact shape	[-]

Chapter 1

Introduction

1.1 General

A tsunami is an impulse wave or series of waves, caused by the mass displacement of water. The source of the displacement can originate from different processes including, but not limited to earthquakes, landslides, volcanic eruptions, and snow or debris avalanches. The impulse wave can be huge (on the order of 100 m) and travel long distances causing significant damage to property and loss of human life. Landslide-triggered tsunamis, the focus of this study, are a natural hazard in alpine regions such as in Norway, Greenland, the Pacific Coast of Canada, the USA and mountainous regions of Europe where steep slopes are often found near bodies of water.

A recent example occurred in June 2017 in Greenland and was responsible for the disappearance of four individuals, whom were presumed dead. An estimated 35 - 51 Mm^3 of material impacted the Karrat Fjord and created a wave which propagated 32 km to the village of Nuugaatsiaq (Besset-Kirton et al., 2017). This failure has been analyzed using three-dimensional point cloud data and has now been classified as a "tsunamigenic extremely rapid rock avalanche" (Gauthier et al., 2017). An example of a fast-moving debris avalanche occurred in December 2007 at Chehalis Lake in British Columbia, Canada. In this event, 3 Mm^3 of quartz diorite travelled approximately 800 m before impacting the water surface (Roberts et al., 2013). The resulting wave propagated along the entire 10 km length of the lake, with a maximum run-up observed to be 37.8 m as measured by the trim-line (Roberts et al., 2013). Fortunately, this event did not result in any fatalities, as the campgrounds located within the run up zone were empty as it was the off-season for tourism.

The potential magnitude of the consequences associated with landslide tsunami events have led to risk assessments for this type of hazard becoming more commonly performed in areas of concern (e.g.

Palcacocha Lake, Peru (Klimeš et al., 2016)) and have become a mandatory requirement for dam risk assessments (Achterberg et al., 1998). The quantification of the hazard relies on accurate predictions of landslide parameters upon impact as well as a sufficient understanding of the momentum transfer to the formation of an impulse wave to estimate the near-field amplitude of the resulting wave. Given the unpredictable nature of the timing of landslide triggering, there are very few historical examples where all the parameters (e.g., landslide volume, thickness, and speed immediately prior to the moment of impact) are known or can be reliably estimated and the effects of the wave accurately observed (e.g. magnitude and distribution of runup around the periphery of the water body). Therefore, researchers have very few datasets based on field cases (e.g. Nuugaatsiaq and Chehalis Lake) to compare observations to predictive equations or numerical models of key tsunami properties such as the maximum wave amplitude or runup (e.g. Fritz et al., 2017; Roberts et al., 2013; Wang et al., 2015; Brideau et al., 2012). Therefore, the study of landslide tsunamis often relies on physical models and empirical formulas developed from laboratory experiments to describe the wave properties for tsunamis generated by landslides. This thesis examines the near-field amplitude of the wave at the site of landslide impact, the shape of the near-field wave, and the resulting consequences for the evolution of wave amplitude during propagation into the far-field.

1.2 Near-field Amplitude

Previous experimental studies investigating two-dimensional wave generation have used a range of landslide materials including solid blocks (Kamphuis and Bowering, 1970); granular material that impacts the reservoir as a solid block (Fritz et al., 2004; Heller and Hager, 2010); a long thin granular flow (Miller et al., 2017); and a positively dense material (Zitti et al., 2015; Zitti et al., 2017), which is used to simulate avalanche applications. Solid blocks, or granular material which acts as such, give a much thicker and shorter landslide upon impact, whereas granular flows that are gravitationally accelerated tend to form granular flows that are thinner and longer. In the latter case, not all of the landslide may have reached the elevation of the water reservoir by the time the first wave is released. This phenomenon was

identified by Miller et al. (2017), who referred to the proportion of the sliding mass responsible for wave generation as the 'effective mass'.

Properties of an impulse-generated wave, such as amplitude and wavelength, can be considered to be a function of the following parameters, as described by Kamphuis and Bowering (1970):

$$f(l, b, s, v_s, \varphi, \alpha, n, \rho_s, \rho, \mu, g, h, x, t)$$

These parameters include the length (l), width (b), thickness (s), velocity (v_s), angle of impact (α) of the landslide as well as the angle between the initial impacting front and the horizontal, the porosity (n) and landslide density (ρ_s) as well as the water density (ρ), viscosity (μ), gravitational acceleration (g), depth (h), distance (x) and time elapsed (t). The landslide porosity (n) is a dependent variable and is related to the landslide density upon impact. The impact shape (φ) varies with the impact angle and bulk landslide volume and therefore has not been considered. The landslide length was determined to be negligible by Kamphuis and Bowering (1970) for experiments completed using solid blocks and therefore was not included.

A total of 348 tests using a depth varying from 0.15 m to 0.675 m and a volume ranging from 0.0167-0.0668 m^3 have previously been conducted by both Fritz et al. (2004) and Heller and Hager (2010). Heller and Hager (2010) also investigated the effects of changing the grain diameter (2 mm - 8mm) and slope angle (30° - 90°) on near-field wave characteristics.

The analytical work of Zitti et al. (2015) and Mulligan and Take (2017) try to capture the proportion of the landslide contributing to the wave using the time and length scales of impact. These scale parameters describe how quickly the submerged mass decelerates after impacting the reservoir, which is a measure of landslide mobility. Mobility is a complex phenomenon of interacting processes that depend on the density, porosity, internal shear strength, basal friction, particle collisions, pore pressures and possible fluidization of the material. Highly mobile flows have the potential to be a more severe hazard due to the high landslide speed and the increased area that can be affected (Iverson et al. 2015).

Both Zitti et al. (2015) and Lindstrøm (2016) evaluated the influence of changing landslide mobility indirectly by using positively buoyant particles and a range in landslide porosity. Initial results from Lindstrøm (2016) indicates increasing the landslide porosity results in a decrease in the near-field maximum amplitude due to a larger deceleration upon impact. This potentially lends support to the hypothesis that increasing landslide mobility will result in larger wave amplitudes; however, the influence of landslide mobility has yet to be quantified directly. Mulligan and Take (2017) assumed that the time and length scale of forcing can be related to each other as a function of the initial horizontal component of the slide velocity in order to simplify the momentum transfer equation. However, the time and length scale of forcing have not typically been reported for past studies on the generation of impulse waves, leaving additional experimental data required to validate this simplifying assumption.

1.3 Wave Classification

The shape of landslide-generated tsunamis have previously been investigated by comparing the wave profile from experimental observations (e.g. Wiegel et al., 1970) to wave theory (e.g. Noda et al., 1970) and developing a classification method (Huber, 1980; Fritz et al., 2004; Zweifel et al., 2006; Heller and Hager, 2011). Fritz et al. (2004) developed an empirical formula to classify waves into four categories (non-linear oscillatory waves, non-linear transition waves, solitary-like waves and dissipative transient bores) based on the landslide properties including velocity and impact thickness. Heller and Hager (2011) examined wave profiles from experimental data and compared results to wave theories to classify the shape as stokes-like, cnoidal-like, solitary-like or bore-like waves. Limiting the classification of these waves into discrete categories causes ambiguity in transition zones between these wave types and this information; however valuable, has limited applicability in prescribing quantitative boundary conditions into numerical models for prediction of wave propagation and runup.

1.4 Far-field Wave Propagation

Previous experiments have used a small scale laboratory method to investigate impulse generated waves in flumes that are 11 m long and 0.5 m wide (Fritz et al., 2004; Heller and Hager, 2010), and 3 m long

and 0.11 m wide (Zitti et al., 2015). Although these studies have been extremely valuable to define the amplitude of the near-field wave immediately after impact, the length of these flumes have not allowed for in-depth analysis of the wave properties in the far-field to investigate evolution of the wave shape and wave amplitude attenuation. Wave shape is an important parameter, which influences the wave amplitude as it propagates and also influences the orbital velocity, sediment transport and wave impact forces (Peregrine, 2003; Hsu and Hanes, 2004).

Two and three-dimensional physical models have been used in the study of impulse waves by Kamphuis and Bowering (1970), Fritz et al. (2004), Heller and Spinneken (2013), Evers et al. (2015), Lindstrøm (2016) and Huber and Hager (1997), Mohammed and Fritz (2012) and Heller and Spinneken (2015). The advantage of a three-dimensional laboratory basin is that it accounts for dissipation through wave radiation, while a two-dimensional flume can give an accurate representation of the energy transfer between the sliding mass and the reservoir at impact. Long water bodies such as fjords and mountainous lakes could also be accurately simplified to two-dimensional problems. The maximum amplitude can dissipate over a longer distance in 2D, due to directional spreading of wave energy in 3D, and therefore the flume length is critical in order to properly analyze far-field wave characteristics.

1.5 Objectives

The objectives of the research program are to use novel physical model observations of tsunamigenic landslide impact, near-field wave characteristics, and wave propagation obtained within a large-scale landslide flume to:

- Investigate the influence of the time and length scales of forcing on the momentum transferred to the wave using dry granular landslides and a landslide material that represents an upper bound of possible mobility (water) to inform further advancements in analytical models of momentum transfer;

- Develop a framework to quantify the shape of waves generated by tsunamigenic landslides in the near-field to permit this information to be included as boundary conditions within numerical models of wave propagation;
- Test the applicability of the HM slides by comparing the impulse waves to those created by varying volumes of LM landslides with negatively buoyant particles;
- Test the hypothesis that the amplitude of waves generated from higher mobility granular flows (e.g. saturated granular flows) will exceed predictions based on the current empirical datasets, which have been derived solely from the behavior of solid blocks or dry granular flows.

1.6 Novelty of the Study

The current study has provided new insight into landslide generating waves by both applying some novel concepts and building on commonly used methods for new applications.

- The effects of water as a sliding mass creating an impulse wave have not previously been investigated and could provide an upper-bound as to the limiting near-field amplitude generated by a landslide of a certain velocity and thickness;

- A detailed investigation as to the influence of varying the landslide type in terms of the near-field maximum wave amplitude has also never been previously completed. These advances will increase the applicability of any previously developed predictive model to field cases;

- The wave shape has not previously been quantified for impulse waves. This provides a more complete description initial wave shapes as well as increasing understanding of wave shape evolution, which aids in understanding of far-field characteristics;

- The solitary wave equation has been modified to provide a time series output, which can account for the range of wave shapes measured in this study.

1.7 Scope of the Study

The focus of the current study is the near-field and far-field wave characteristics due to the impact parameters of the landslide. Therefore, the landslide properties prior to impact such as interparticle collisions have not been measured. The total range of landslide parameters measured over the duration of this study are $1.5 < F < 5.4$ and $0.02 < S < 0.58$ creating waves of dimensionless amplitude $A_m < 2.3$. The impulse wave properties were measured over a flat bottom flume with constant depth in two-dimensions due to the confining sidewalls. The amplitude of the wave run-up was not measured in this study.

1.8 Organization of Thesis

In accordance with the regulations outlined by the School of Graduate Studies at Queen's University, this thesis has been prepared in manuscript format. Chapter 1 of this dissertation gives a general introduction of the dangers of impulse generated waves and previous studies. Chapters 2, 3, 4 and 5 are original manuscripts and have not been submitted to journals at present.

Chapter 2 presents the results from 41 tests conducted at the Queen's University Landslide flume of impulse waves generated by highly mobile flows. Highly mobile flows emphasize the importance of the length of forcing in order to accurately estimate the near-field wave amplitude.

Chapter 3 analyzes the data collected from Chapter 2, looking at the far-field characteristics and wave shape. It also includes a novel method of simulating wave shape, which can be used as boundary conditions for numerical models.

Chapter 4 presents the results from impulse waves generated by three varying volumes of dry granular slides in the Queen's University Landslide flume, which demonstrate the same behaviours of waves generated by highly mobile slides. The length of forcing is hypothesized to be the reason for the discrepancy in near-field maximum wave amplitude between dry granular and highly mobile water flows.

Chapter 5 compares the mobility of fully saturated granular flows to the dry granular and highly mobile water flows completed in Chapter 2 and Chapter 4. The length of forcing is quantified for all three types of flows and provides further understanding to the parameters involved for varying landslide mobility.

Chapter 6 provides a summary of the work completed, as well as the overall impact and future recommendations.

1.9 References

Achterberg, D., Gotzmer, J. W., Spath, R., Tseng, M., Woodward, D. E., Miller, N., & Shipman, S. A. (1998). Federal guidelines for dam safety: selecting and accommodating inflow design floods for dams. *Dept. of Homeland Security, Federal Emergency Management Agency, Washington, DC*.

Bessette-Kirton, E., Allstadt, K., Pursley, J., and Godt, J. (2017). Preliminary analysis of satellite imagery and seismic observations of the Nuugaatsiaq landslide and tsunami, Greenland. *USGS, Washington, DC https://landslides. usgs. gov/research/featured/2017-nuugaatsiaq/ Google Scholar*.

Brideau, M. A., Sturzenegger, M., Stead, D., Jaboyedoff, M., Lawrence, M., Roberts, N. J., ... & Clague, J. J. (2012). Stability analysis of the 2007 Chehalis lake landslide based on long-range terrestrial photogrammetry and airborne LiDAR data. *Landslides*, *9*(1), 75-91.

Evers, F. M., & Hager, W. H. (2015). Impulse wave generation: comparison of free granular with mesh-packed slides. *Journal of Marine Science and Engineering*, *3*(1), 100-110.

Fritz, H.M., Hager, W.H. and Minor, H.E. (2004). Near field characteristics of landslide generated impulse waves. *Journal of Waterway, Port, Coastal, and Ocean Engineering*, *130*(6), 287-302.

Fritz, H. M., Giachetti, T., Anderson, S., and Gauthier, D. (2017, December). Field Survey of the 17 June 2017 Landslide and Tsunami in Karrat Fjord, Greenland. In *AGU Fall Meeting Abstracts*.

Gauthier, D., Anderson, S. A., Fritz, H. M., and Giachetti, T. (2018). Karrat Fjord (Greenland) tsunamigenic landslide of 17 June 2017: initial 3D observations. *Landslides*, *15*(2), 327-332.

Heller, V. and Hager, W.H. (2010). Impulse product parameter in landslide generated impulse waves. *Journal of Waterway, Port, Coastal, and Ocean Engineering*, *136*(3), 145-155.

Heller, V. and Hager, W.H. (2011). Wave types of landslide generated impulse waves. *Ocean Engineering*, *38*(4), 630-640.

Heller, V. and Spinneken, J. (2013). Improved landslide-tsunami prediction: effects of block model parameters and slide model. *Journal of Geophysical Research: Oceans*, *118*(3), 1489-1507.

Heller, V., and Spinneken, J. (2015). On the effect of the water body geometry on landslide-tsunamis: physical insight from laboratory tests and 2D to 3D wave parameter transformation. *Coastal Engineering*, 104(10), 113-134.

Hsu, T.J. and Hanes, D.M. (2004). Effects of wave shape on sheet flow sediment transport. *Journal of Geophysical Research: Oceans*, *109*(C5).

Huber, A. (1980). Schwallwellen in Seen als Folge von Felsstürzen (Reservoir Impulse Waves Caused by Rockfall). VAW Mitteilung 47, Versuchsanstalt für Wasserbau, Hydrologie und Glaziologie, ETH Zürich.

Huber, A., and Hager, W.H. (1997). Forecasting impulse waves in reservoirs. *Dix-neuvieme Congres des Grands Barrages C*. 31, 993-1005. Florence, Italy, Commision Internationale des Grands Barrages, Paris.

Kamphuis, J.W., and Bowering, R.J. (1970). Impulse waves generated by landslides. *Proc., 12th Coastal Engineering Conf.*, ASCE, REST, Va. 1. 575-588.

Klimeš, J., Novotný, J., Novotná, I., Jordán de Urries, B., Vilímek, V., Emmer, A., Strozzi, T., Kusák, M., Cochachin Rapre, A., Hartvich, F., and Frey, H. (2016). Landslides in moraines as triggers of glacial lake outburst floods: example from Palcacocha Lake (Cordillera Blanca, Peru). *Landslides*, *13*(6), 1461-1477.

Lindstrøm, E.K. (2016). Waves generated by subaerial slides with various porosities. *Coastal Engineering*, *116*, 170-179.

Mohammed, F. and Fritz, H.M. (2012). Physical modeling of tsunamis generated by three-dimensional deformable granular landslides. *Journal of Geophysical Research: Oceans*, *117*(C11).

Miller, G.S., Take, W.A., Mulligan, R.P, and McDougall, S. (2017). Tsunamis generated by long and thin granular landslides in a large flume. *J. Geophys. Res. Oceans*, 122,653-668, DOI: 10.1002/2016JC012177.

Noda, E. (1970). Water waves generated by landslides. *Journal of the Waterways, Harbors and Coastal Engineering Division*, *96*(4), 835-855.

Peregrine, D.H. (2003). Water-wave impact on walls. *Annual review of fluid mechanics*, *35*(1), 23-43.

Roberts, N. J., McKillop, R. J., Lawrence, M. S., Psutka, J. F., Clague, J. J., Brideau, M. A., & Ward, B. C. (2013). Impacts of the 2007 landslide-generated tsunami in Chehalis Lake, Canada. In *Landslide science and practice* (pp. 133-140). Springer, Berlin, Heidelberg.

Wang, J., Ward, S. N., & Xiao, L. (2015). Numerical simulation of the December 4, 2007 landslide-generated tsunami in Chehalis Lake, Canada. *Geophysical Journal International*, *201*(1), 372-376.

Wiegel, R.L., Noda, E.K., Kuba, E.M., Gee, D.M. and Tornberg, G.F. (1970). Water waves generated by landslides in reservoirs. *Journal of the Waterways, Harbors and Coastal Engineering Division*, *96*(2), 307-333.

Zitti, G., Ancey, C., Postacchini, M. and Brocchini, M. (2015). Impulse waves generated by snow avalanches falling into lakes. In *Proceedings of 36th IAHR World Congress, The Hague, Netherlands, 2015* (No. EPFL-CONF-215899). IAHR.

Zitti, G., Ancey, C., Postacchini, M. and Brocchini, M. (2017). Snow avalanches striking water basins: behaviour of the avalanche's centre of mass and front. *Natural Hazards*, 1-27.

Zweifel, A., Hager, W.H. and Minor, H.E. (2006). Plane impulse waves in reservoirs. *Journal of Waterway, Port, Coastal, and Ocean Engineering*, *132*(5), 358-368.

Chapter 2

Experimental analysis of tsunamis generated by the impact of landslides with high mobility

2.1 Introduction

A tsunami is a wave or series of waves caused by the bulk mass displacement of water. The source of the displacement can take different forms including submarine and subaerial landslides such as avalanches and debris flows. These waves are complex hazards, which can behave very differently depending on the way a landslide impacts a reservoir or body of water at the base of the slope. Landslide mobility is known to influence the velocity and total runout distance of the landslide, and an example of a slide with high mobility is a saturated debris flow with high pore water pressures (Legros, 2002). Mobility is a complex phenomenon of interacting processes that depend on the density, porosity, internal shear strength, basal friction, particle collisions, pore pressures and possible fluidization of the material (Legros, 2002). Highly mobile flows have the potential to be a more severe hazard due to the high slide speed and the increased area that can be affected (Iverson et al. 2015). Understanding the type of slope failure and bulk properties of the slide material, including mobility, is critical in field cases (e.g., Klimeš et al., 2016; Gauthier et al., 2017) to help manage risk of future events by correctly applying methods of predicting the landslide-generated wave.

Subaerial landslide-triggered tsunamis have been well studied using physical models with a particular focus in quantifying the maximum wave amplitude (Fritz et al., 2004; Heller and Hager, 2010). Heller and Hager (2010) investigated the effects of varying the landslide density and completed experiments over an even wider range of masses, thicknesses and velocities than tested by Fritz et al. (2004). The large dataset was used to develop semi-empirical formulae, to predict the near-field maximum wave amplitude using the landslide parameters. For positively buoyant debris flows, such as snow avalanches, Zitti et al. (2015) modified the semi-empirical formula developed by Heller and Hager (2010). In this study, the same slide

parameters were used with different exponential relationships to describe the maximum amplitude of the waves. Miller et al. (2017) released granular material in a large flume to produce long and thin trains of material that generated waves with smaller amplitudes than those that were pneumatically accelerated in a smaller-scale experimental facility (e.g., Fritz et al., 2004; Heller et al., 2010). The results indicate that this type of impact occurs over an 'effective time' where the landslide transfers momentum to the reservoir and determines the size of the waves produced. Recent tests by Heller et al. (2016) also indicate that the majority of energy transferred during slide-water interaction experiments occurs over a short time of only 0.5 s after impact. A momentum-based theoretical approach for predicting the maximum wave amplitude was developed by Mulligan and Take (2017), and the results were in agreement with the experimental observations of Heller and Hager (2010) and Miller et al. (2017) for granular landslides.

Landslides with higher mobility have higher impact velocities and longer distances. It is hypothesized that an increase in landslide mobility will also result in a longer distance over which the slide momentum is imparted to the water, resulting in larger waves compared to slides with lower mobility. A wave generated by a highly mobile slide is depicted in Figure 2.1, and the momentum transfer occurs over an effective length (L_e) and an effective time (t_e) until the wave speed (c_s) exceeds the submerged slide velocity (v). After the effective time, the wave releases from generation region, the propagation speed is a function of the water depth (h) and the maximum amplitude (a_m), and the submerged material comes to rest at distal reach (R). The objective of this paper is to investigate the characteristics of waves generated by slides with high mobility, such as mudflows or saturated debris torrents. This experimental approach also has the advantage of rapid re-setting of the test conditions, allowing a wide range of source volumes and reservoir depths to be investigated. The laboratory observations results are compared to the results of predictive equations from previous studies, allowing the applicability of the near-field maximum wave amplitudes generated by highly mobile slides to be determined. This study provides a vital set of observations necessary for a better understanding of the generation and transformation of tsunamis

created by landslides with high mobility, which is important to increase applicability of the current predictive models to a wider variety of landslide types.

2.2 Methodology

2.2.1 Landslide Flume Experiments

The Queen's University landslide flume is a large-scale experimental facility for the generation of landslides and tsunamis under the force of gravity. It is comprised of a 6.73 m long 30° slope connected to a 33.8 m long flat-bottom wave flume shown in Figure 2.2. The flume is 2.10 m wide with sidewalls that are 1.21 m in height. The sidewalls of the slope and the first 3.7 m of the flat section are tempered glass, and after this distance the walls are made of concrete. At the end of the flume is a 2.7 m long run-up ramp sloped at an angle of 27°. The landslide source volume is held in an aluminium box with a maximum capacity of 1.68 m^3. When the release box is triggered, the gate rapidly swings open about a hinge with an angular velocity of 1 ms^{-1} at the tip of the gate. In the present study, the material released from the aluminum box is water and the volume is varied from 0.1-0.4 m^3 in increments of 0.1 m^3 as indicated in Figure 2.2. With zero internal shear strength, water produces a fast-moving slide analogous to a fluidized mudflow or saturated debris flow and is representative of the upper limit of high landslide mobility. The depth of the reservoir is varied from 0.15-0.65 m in 0.05 m increments, and in total 41 tests were conducted that covered a wide range of source volumes and reservoir depths.

2.2.2 Sensors

The landslide flow thickness (s) was measured using a side-looking Proscilica GX1050 camera with a Nikon Nikkor 24 mm f/2.8D lens at the interface between the sliding water and the reservoir at 100 Hz with a spatial and temporal resolution of 1024x1024 pixels. Rotated at 30° to make the horizontal image parallel to the slope, the field of view is shown in Figure 2.2 labelled as "Cam 1". The velocity of the slide (v_s) was measured using the downward-looking "Cam 2", titled 30° upward such that the bottom of the field of view is normal to the slope and is 0.9 m up the slope from the corner. This camera is a Sony RX10M2 with a 24-200 mm f/2.8 lens, recording at 480 Hz. The landslide impact region for both of these

cameras was illuminated with a high-seed flicker free Pallite VIII light source. A Canon T5i camera labelled as “Cam 3” was placed 3.2 m from the outside of the flume where the field of view includes the slide impact zone to and the wave generation zone. This camera is used to capture images at 29 Hz with a resolution of 1929x1101 pixels and is used to observe the waves in the near-field region.

An acoustic Doppler current profiler (Nortek Vectrino) was used to measure the fluid velocity at 100 Hz in four 4 mm wide bins over the range z = 0.003-0.012 m from the bottom of the flume, located just beyond the maximum distal reach of the largest slides at x = 3.1 m from the corner of the landslide slope. The water surface elevation (η) was measured using nine 0.6 m long capacitance wave probes (Akamina AWP-24 Wave Height Gauge) that sampled at 100 Hz. These wave probes were located along the flume centreline at stations P1-P9 (x = 1.9, 3.1, 6.0, 8.8, 11.3, 16.8, 22.0, 26.6 and 32.5 m) from the origin x = 0.0 m at the base of the landslide slope. The probes are accurate to $\pm$0.001 m and are synchronized using a 16-bit/1-MHz USB data acquisition system.

2.2.3 Testing

A Pentair 3HP IntelliFlo Variable Speed Pump was used to transport water from a sealed tank at ground level through a series of 40 mm diameter PVC pipes to the elevation of the landslide source. The water level in the source volume was monitored remotely using a GoPro Hero 4 Silver camera. Upon pneumatic opening of the release box, the source material accelerates down the slope until it impacts the reservoir depth at a velocity and thickness dependent on the initial source volume. The slide impact impulsively generates a train of waves where the leading wave has the largest amplitude. This wave propagates along the length of the flume, sloshes up the run-up ramp, and reflects back along the flume. After the completion of an experiment, the fluctuations in the reservoir were measured in order to quantify the point at which the reservoir could be considered still. The standard deviation of the water surface elevation measured by the wave probes was determined and a threshold of 0.005 m or less was achieved before moving on to the next test.

2.3 Observations and Analysis

2.3.1 Slide Impact

The landslide velocity just prior to impact was measured using the downward-looking Cam 2. Particle Image Velocimetry was performed on the digital images using geoPIV (White et al., 2003) to compute the incremental displacement of the water between frames and thus v_s. The velocity time series for each source volume is shown in Figure 2.3. It is noted that in each case v_s is relatively constant over the initial 0.39-0.62 s, and decreases over the next 1 s until the landslide thickness is negligible (s < 0.0008 m). For each source volume, the average velocity $\bar{v_s}$ over the initial time was computed for all reservoir water depths. These values are listed in Table 2.1 and vary from 5.08-6.51 ms^{-1}, with higher $\bar{v_s}$ corresponding to larger source volumes.

The instantaneous thickness of the slide was computed using the images obtained from side-looking Cam 1. The surface of the sliding water was identified using a green pixel intensity threshold, and the location of exceedance of the threshold was mapped over the field of view for each frame. Time series of the slide thickness of each source volume is shown in Figure 2.3. The peak flow thickness, which occurs at a different point in time for each source volume, varies from 0.030–0.074 m. The average landslide thickness $\bar{s}$ over the initial time is listed in Table 2.1 and range from 0.022-0.056 m, with incrementally higher $\bar{s}$ corresponding to larger source volumes.

The cameras used to measure the slide speed and thickness are also used to determine the total time of the landslide (Δt_s) and the effective time (Δt_e) required to generate the waves. In this study, the time over which the landslide parameters are averaged has been quantified using the landslide momentum flux M_s (Mulligan and Take, 2017) defined as

$$M_s = \frac{\rho_s s v_s cos\alpha}{\Delta t_e} \quad \text{(Eq 2.1)}$$

The numerator in Eq 2.1 quantifies the rate of change of landslide momentum and is plotted as a function of time in Figure 2.4 for each source volume. The smaller source volumes have a smaller peak in slide momentum, which occurs at an earlier point in time compared to the larger volumes. The vertical lines indicate the time over which the parameters of v_s and s have been averaged. This parameter is quantified by the amount of time for 75% of the total landslide to impact the water, expressed as Δt_{M75}. This point in time increases for each increase in source volume, due to the increasing length of the slide. The average values of landslide times are listed in Table 2.1 and it is important to note that Δt_{M75} is approximately 50% of the value of Δt_s. This is important as only part of the landslide is involved in the generation of the wave, and is consistent with the findings of Miller et al. (2017) in describing the time over which the effective mass of the landslide generates the wave.

The average landslide velocity and thickness for each source volume are shown in Figure 2.5. Both properties increase with volume, however the thickness has a linearly increasing trend with volume and the velocity has small changes for low volumes and larger increases at higher volumes. Therefore, as revealed by these experiments, increasing the source volume has a larger effect on changing the slide thickness than the impact velocity.

Table 2.1 Summary of landslide parameters for each source volume

Source Volume, V (m^3)	Average landslide velocity, $\bar{v_s}$ (m/s)	Average landslide thickness, $\bar{s}$ (m)	Average time of wave generation, Δt_{M75} (s)	Total time of landslide (s < 0.0008 m), Δt_s (s)
0.1	5.08	0.022	0.39	0.77
0.2	5.09	0.032	0.50	0.89
0.3	5.38	0.043	0.57	1.05
0.4	6.51	0.056	0.62	1.12

2.3.2 Wave Generation

The near-field generation of the waves occurs at the base of the landslide slope over $0 < x < 4$ m and is recorded using Cam 3, where the time of impact is referenced to time $t = 0$ s indicated in Figure 2.6a.

Immediately after the impact initiates, the wave amplitude is high due to the rapid vertical movement of water combined with the entrainment of air in the splash shown in Figure 2.6b. As the wave forms, the maximum water surface displacement is located very close to the horizontal position of the submerged turbulent landslide plume (Figure 2.6b-d). The landslide decelerates and at a certain point the wave releases from the slide and the slide no longer influences the properties of the wave (Figure 2.6d-e). This occurs at the effective time Δt_e, defined as the length of time until the wave speed c_s exceeds the submarine landslide velocity v. The submerged plume continues to decelerate and elongate after the effective time has passed but the wave propagates out of the near-field region (Figure 2.6e). The runout distance R of the submarine slide is measured when the submerged velocity $v = 0$ ms^{-1}.

The difference in landslide waves for each source volume is shown as a series of images in Figure 2.7. These images have been selected when the crest of the wave is at $x \approx 1.3$ m, and are all for tests with the same water depth of $h = 0.30$ m. The larger source volumes result in larger and more turbulent (more bubbles) submerged landslide plumes, which in turn produces waves with larger amplitudes. For consistency between all tests, the near-field maximum wave amplitude is from here on defined as the value of a_m at wave probe P1 ($x = 1.9$ m).

The water surface elevation time series measured by each wave probe are shown together in Figure 2.8 for each source volume and $h = 0.3$ m. At the near-field probe (P1, $x = 1.9$ m) the wave amplitudes are significantly higher for the larger source volumes, the same result as observed with the images from Cam 3. As the waves propagate along the flume, the larger wave amplitudes decrease rapidly until $x = 11.3$ m and beyond this distance all the waves continue to propagate with a similar amplitude close to 0.18 m. This suggests that the larger waves break at higher rates and attenuate in amplitude until they reach a stable depth-limited size. Differences in wave speed are also evident in Figure 2.8. The waves arrive at the first wave probe (P1) at a similar time and the arrival time at the furthest probe from the impact site (P9, $x = 26.6$ m) differs by approximately 3 s with the smaller source volumes (non-breaking waves) arriving before the larger source volumes (breaking waves). The separation distance between the leading

wave and the next wave in the wave train also changes with the difference in wave speed. The smallest source volume produces the largest amplitude second and third waves in the train, and has the shortest wave train length. The fastest moving leading wave will continue to increase the separation time as it propagates and could result in an increase in hazard due to people removing themselves from an area of safety prematurely.

Near-bottom fluid velocity measurements in the same water depth (h = 0.3 m) and the same location (x = 3.1 m) are shown in Figure 2.9 for each source volume. The time series have been adjusted for comparison and thus are not relative to the impact time of each landslide. These data indicate that the larger source volumes produce larger maximum fluid velocities (u_m), where a Butterworth lowpass filter with a cutoff frequency of 0.3 Hz was applied for smoothing of the raw signal. As the waves sweep past the sensor location, orbital motion is evident with significantly higher maxima that occurs before each minima. The highest positive velocity for V = 0.4 m^3 is 1.1 ms^{-1}, followed by the negative velocity of -0.50 ms^{-1} and the time period between this points in the wave phase is longer than for the smaller source volumes.

The properties observed by a combination of Cam 3, the Vectrino Profiler and the P2 wave probe are shown in Figure 2.10 and provide an overview of the near-field wave behaviour over the wide range of test conditions with varying h and V. As indicated in Figure 2.10a, the maximum wave amplitude for each source volume increases for a given h but a_m for a constant volume had a limited range of variation for 0.15 m < h < 0.65 m. The maximum fluid velocity varies significantly with the reservoir depth. The value of u_m at this location is inversely proportional to water depth, with the highest recorded fluid velocity occurring in the shallowest h (Figure 2.10b). This is mostly due to the fact that the measurements are made at the same z, and in deeper water this means the sampling location is further from the free surface. In addition, increasing h provides a longer horizontal distance between the surface impact site and the stationary Vectrino sensor at P2, possibly influencing the velocity signal. The total runout distance of the submerged turbulent plume R and the effective length of forcing L_e are shown in Figure

2.10c-d. The length of the plume varies with both source volume and with reservoir depth. Shallow reservoirs have less water to displace, allowing the highly mobile slide to propagate further horizontally. As h increases, the difference between the runout length R and the effective length L_e decreases until they are almost the same (e.g., for $h > 0.55$ in these experiments). Therefore, for some cases where the reservoir is deep relative to the slide thickness, the effective length over which the wave is generated can be approximated using the total runout length of the slide.

2.3.3 Wave Breaking Limit

The maximum amplitude measured at each wave probe is shown in Figure 2.11, indicating the changes in wave size with propagation away from the impact site for the reservoir depths and source volumes in all 41 experiments. The effect of changing the landslide source volume is clearly evident, with larger V generating larger near-field waves. At P1 the wave amplitude is relatively independent of depth and is only a function of the source volume, indicating the importance of landslide size on wave generation. As the wave continues to propagate from P2-P5, two very distinct types of behaviour occur. These include breaking waves, with rapid attenuation of the amplitude, and non-breaking waves, with only small changes to a_m. Grilli et al. (1997) describes the maximum stable solitary wave in constant depth to be defined by the wave breaking limit

$$\frac{\eta}{h} \cong 0.80 \qquad \text{(Eq 2.2)}$$

where η is the water surface elevation. This expression indicates that any wave exceeding this limit will break, resulting in an immediate reduction in amplitude. The observations in the present study indicate that the relationship is more accurately expressed by

$$\frac{a_m}{h} = 0.60 \qquad \text{(Eq 2.3)}$$

This ratio is indicated by the dashed lines in Figure 2.11, and it is clear that all points that lie above this limit are reduced as they propagate. In the far-field (e.g., P5-P9) the waves have all broken and each

source volume has a peak value of a_m that occurs in a different water depth. This reservoir depth, defined as the critical depth h_{cr}, lies on the line expressed by Eq. 2.3 and changes as a function of source volume due to the combination of landslide momentum transfer and wave breaking processes. These findings are in agreement with the experimental results of Miller et al. (2017) for dry granular landslide slides, but the present results delineate the trend over a wide range of source volumes for highly mobile slides.

2.4 Comparison with Predictive Equations

2.4.1 Previous Studies

The maximum amplitude of landslide-generated waves have been investigated in several previous studies, and used to develop predictive frameworks. These studies (e.g., Fritz et al., 2004; Heller and Hager, 2010) mainly focussed on the effects of the landslide parameters (landslide thickness s, velocity v_s) on the maximum wave amplitude a_m in and depth h. The experiments completed by Fritz et al. (2004), Zweifel et al. (2006) and Heller and Hager (2010) used pneumatically accelerated granular material, which impacted the reservoir almost instantaneously into an 11 m long, 0.5 m wide and 1 m high flume. Heller and Hager (2010), referred to hereafter as HH10, completed of 211 experiments and developed a semi-empirical equation to describe wave properties as a function of the 'impulse product parameter', P. This is given by

$$P = FS^{1/2}M^{1/4}\left\{\cos\left[\left(\frac{6}{7}\right)\alpha\right]\right\}^{1/2} \quad \text{(Eq 2.4)}$$

where the slide Froude number is $F = \frac{v_s}{\sqrt{gh}}$, the relative slide thickness is $S = \frac{s}{h}$, the relative slide mass is $M = \frac{m_s}{\rho_w b h^2}$ (a function of the slide mass m_s, the density of water ρ_w, the channel width b and water depth h), and the impact angle is α. The relative maximum amplitude A_m is expressed solely as a function of P, and is given by

$$A_m = \frac{a_m}{h} = \left(\frac{4}{9}\right)P^{4/5} \quad \text{(Eq 2.5)}$$

In a different experimental study, Zitti et al. (2015) used positively buoyant particles to generate waves by avalanches that impact water. In this study, referred to hereafter as Z15, 42 experiments were conducted and two empirical methods were developed based on the impulse product parameter expression developed by Heller and Hager (2010) in Eq. 2.4. The first expression is dependent on slide thickness and is given by

$$P_s = F^{0.4}M^{0.9}S^{0.3}cos\alpha^{0.7} \quad \text{(Eq. 2.6)}$$

$$A_m = 0.2P_s^{0.5} \quad \text{(Eq. 2.7)}$$

The second formula is dependent on the total time of landslide impact Δt_s, given by

$$P_{\Delta t} = F^{0.2}M^{0.8}\Delta t_s^{-0.2}cos\alpha^{0.7} \quad \text{(Eq. 2.8)}$$

$$A_m=0.5P_{\Delta t} \quad \text{(Eq. 2.9)}$$

Mulligan and Take (2017) explored the maximum amplitude of landslide-generated tsunamis using a theoretical expression that describes the momentum balance between a landslide and water. The hydrostatic momentum equation (Eq. 2.10) describes the along-channel pressure gradient created by the vertical increase in water level upon slide impact.

$$a_q = \sqrt{h^2 + \frac{2\rho_s s v_s cos\alpha L_e}{\rho g \Delta t_e}} - h \quad \text{(Eq 2.10)}$$

This approach introduces length and time parameters, which were not considered by Heller and Hager (2010). The length and time scales are difficult to measure outside a laboratory setting and therefore a simplification can be made in which the average velocity is used to estimate constant deceleration of the landslide over the period of wave detachment and therefore:

$$L_e = \frac{1}{2}v_s cos\alpha \Delta t_e \quad \text{(Eq 2.11)}$$

This simplification has been validated for the relevant dataset collected by Heller and Hager (2010). Substitution of Eq. 2.11 into Eq. 2.10, yields

$$a_q = \sqrt{h^2 + \frac{\rho_s s (v_s cos\alpha)^2}{\rho g}} - h \qquad \text{(Eq 2.12)}$$

where a_q denotes the maximum wave amplitude derived from a quadratic momentum balance equation. This equation, referred to hereafter as MT17, results predictions that are in very good agreement with the experimental observations of Miller et al. (2017) for dry granular landslides. This study considered a range of water depths (h = 0.05-0.5 m), but only one type of landslide (s = 0.035 m, v_s = 4.5 ms^{-1}, ρ_s = 1500 kgm^{-3}, α = 30°). It is therefore important to quantify the applicability of this predictive approach for other types of landslides with different size and mobility.

2.4.2 Applicability to Highly Mobile Flows

The relative maximum amplitude ($A_m = a_m/h$) for all data measured at P1 is shown in Figure 2.12 as scatter plots in comparison with the results of the three predictive equations developed by HH10 (Eq. 2.5), Z15 (Eq. 2.9) and MT17 (Eq. 2.12). These equations were developed each for different landslides than the highly mobile flows in the present study and it is not surprising that they all underestimate the near-field relative maximum amplitude. The root-mean-square error (RMSE) values indicate the closeness of fit between the data and each equation in dimensionless units corresponding to A_m. These errors indicate that HH10 has the best agreement with observations, however none of these equations capture the bulk trend in the relative maximum amplitude.

The same data shown in Figure 2.12 is provided in Figure 2.13 in comparison with two predictive equations that include time. The first is the 'impulse product parameter' type of equation developed by Z15 for positively buoyant particles. This formula includes the total landslide time, and the results provide accurate estimates of the near-field relative maximum amplitude for non-breaking waves with low values of A_m in the near-field (Figure 2.13a). However, images of the wave generation process (e.g.,

Figure 2.6) suggest that the entire length of the landslide does not influence the wave. The inclusion of a time scale by Z15 improves the overall match with data (RMSE = 0.25), however the predictions are poor for $A_m > 1$.

The hydrostatic momentum balance equation is compared with the same observations in Figure 2.13b. This predictive equation includes the wave generation timescale by considering the upper-limit of velocity of the submarine landslide plume over the effective length. Given the very high mobility of these slides, the maximum velocity relationship is given by

$$L_e = v_s cos\alpha \Delta t_e \quad \text{(Eq 2.13)}$$

In contrast to the factor of ½ used to indicate deceleration of the horizontal velocity ($v_s cos\alpha$) suggested in Mulligan and Take (2017) and shown in Eq. 2.11, this relationship implies that the full landslide impact velocity generates the wave. Substituting this relationship into the momentum balance equation (Eq. 2.10) simplifies to

$$a_{q,max} = \sqrt{h^2 + \frac{2\rho_s s(v_s cos\alpha)^2}{\rho g}} - h \quad \text{(Eq 2.14)}$$

This expression provides the most accurate estimates of the relative maximum amplitude (RMSE = 0.09) for the highly mobile flows measured in this study (Figure 2.13b). This simple approach is best for predicting the near-field wave amplitude, and indicates the importance of the high landslide velocity over the time scale of transfer of momentum to the fluid.

2.5 Summary and Conclusions

In this study a series of 41 experiments were conducted by releasing material into the reservoir of a large landslide flume. The slide material was water, representative of a debris flow with high mobility and impact velocity, and the source volume was varied to test the influence of varying the landslide thickness. The reservoir depth was also varied and the waves generated were measured using a system of digital

cameras, wave probes and fluid velocity sensors. The landslide source volume is a primary control on the near-field wave amplitude. In fact, the near-field maximum wave amplitude is relatively independent of depth and is only a function of the source volume, indicating the importance of landslide size on wave generation. After the landslide tsunamis are generated, wave breaking controls the maximum amplitude as they propagate along the flume. The observations in the present study indicate that the wave breaking limit is accurately expressed by $a_m/h = 0.6$ and in the far-field each source volume has a peak value of a_m that occurs in a different water depth. Therefore, for a given reservoir depth, the maximum wave amplitude changes as a function of source volume due to the combination of landslide momentum transfer and wave breaking processes.

The experimental observations of maximum wave amplitude were compared to the results of predictive equations developed in previous studies by Heller and Hager (2010), Zitti et al (2015) and Mulligan and Take (2017) for other types of landslides. With knowledge of the effective length and time scales of wave generation gained in the present study, a maximum velocity relationship for highly mobile landslides was developed. This was applied to the hydrostatic momentum equation in Mulligan and Take (2017). The new expression provided the most accurate estimates of the relative maximum amplitude for the highly mobile slides and indicates the importance of the high landslide velocity over the time scale of transfer of momentum to the fluid. This simple predictive method is unable to account for more complex physical processes such as air entrainment and turbulence, and further investigation into wave generation by highly mobile landslides using numerical models is recommended to describe this behaviour. The detailed data collected in this study would be ideal for validation of such models, which could then be used to simulate tsunamis in reservoirs or fjords with varying bathymetry. Overall, the results of the present study indicate the dependence of wave amplitude on source volume and the correct methods of predicting severely hazardous tsunamis generated by landslides with high mobility.

2.6 References

Fritz, H.M., Hager, W.H. and Minor, H.E. (2004). Near field characteristics of landslide generated impulse waves. *Journal of Waterway, Port, Coastal, and Ocean Engineering*, *130*(6), 287-302.

Gauthier, D., Anderson, S.A., Fritz, H.M., and Giachetti, T. (2018). Karrat Fjord (Greenland) tsunamigenic landslide of 17 June 2017: initial 3D observations. *Landslides*, *15*(2), 327-332.

Grilli, S.T., Svendsen, I.A., and Subramanya, R. (1997). Breaking criterion and characteristics for solitary waves on slopes. *Journal of Waterway, Port, Coastal, and Ocean Engineering*, *123*(3), 102-112.

Heller, V., Bruggemann, M., Spinneken, J., and Rogers, B.D. (2016). Composite modelling of subaerial landslide–tsunamis in different water body geometries and novel insight into slide and wave kinematics. *Coastal Engineering*, *109*, 20-41.

Heller, V., Hager, W.H. and Minor, H.E. (2008). Scale effects in subaerial landslide generated impulse waves. *Experiments in Fluids*, *44*(5), 691-703.

Heller, V., and Hager, W.H. (2010). Impulse product parameter in landslide generated impulse waves. *Journal of Waterway, Port, Coastal, and Ocean Engineering*, *136*(3), 145-155.

Iverson, R.M., George, D.L., Allstadt, K., Reid, M.E., Collins, B.D., Vallance, J.W., Schilling, S.P., Godt, J.W., Cannon, C.M., Magirl, C.S., Baum, R.L., Coe, J.A., Schultz, W.H. and Bower J.B. (2015). Landslide mobility and hazards: implications of the 2014 Oso disaster. *Earth and Planetary Science Letters*, *412*, 197-208.

Klimeš, J., Novotný, J., Novotná, I., Jordán de Urries, B., Vilímek, V., Emmer, A., Strozzi, T., Kusák, M., Cochachin Rapre, A., Hartvich, F., and Frey, H. (2016). Landslides in moraines as triggers of glacial lake outburst floods: example from Palcacocha Lake (Cordillera Blanca, Peru). *Landslides*, *13*(6), 1461-1477.

Legros, F. (2002). The mobility of long-runout landslides. *Engineering Geology*, *63*(3-4), 301-331.

Miller, G.S., Take, W.A., Mulligan, R.P., and McDougall, S. (2017). Tsunamis generated by long and thin granular landslides in a large flume. *Journal of Geophysical Research: Oceans*, *122*(1), 653-668.

Mulligan, R.P., and Take, W.A. (2017). On the transfer of momentum from a granular landslide to a water wave. *Coastal Engineering*, *125*, 16-22.

White, D.J., Take, W.A., and Bolton, M.D. (2003). Soil deformation measurement using particle image velocimetry (PIV) and photogrammetry. *Geotechnique*, *53*(7), 619-631.

Zitti, G., Ancey, C., Postacchini, M. and Brocchini, M. (2015). Impulse waves generated by snow avalanches falling into lakes. In *Proceedings of 36th IAHR World Congress, The Hague, Netherlands, 2015* (No. EPFL-CONF-215899). IAHR.

Zweifel, A., Hager, W.H. and Minor, H.E. (2006). Plane impulse waves in reservoirs. *Journal of Waterway, Port, Coastal, and Ocean Engineering*, *132*(5), 358-368.

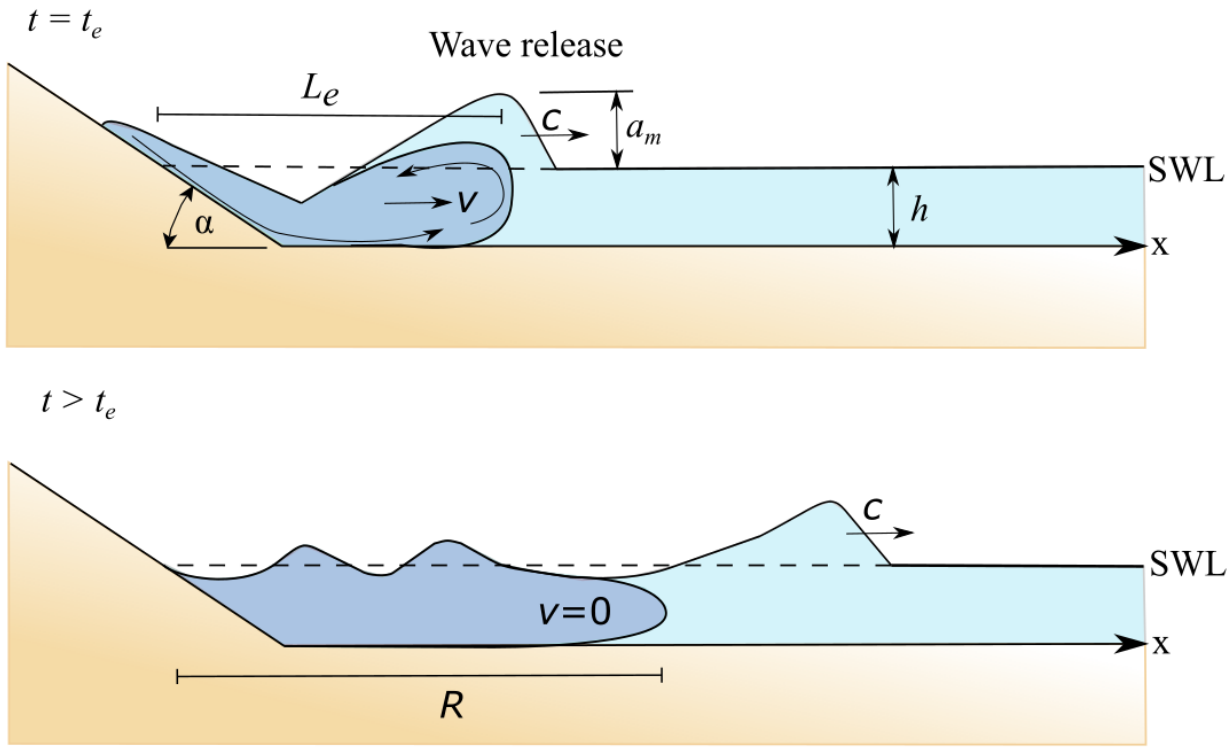

Figure 2.1: Conceptual sketch of wave generation by a landslide with high mobility indicating the effective length of the momentum transfer zone L_e, defined by the point at which the wave speed c_s is greater than the speed of the submerged plume v. After the point of wave release from the momentum transfer zone, the plume extends until $v = 0$ to the maximum runout distance R.

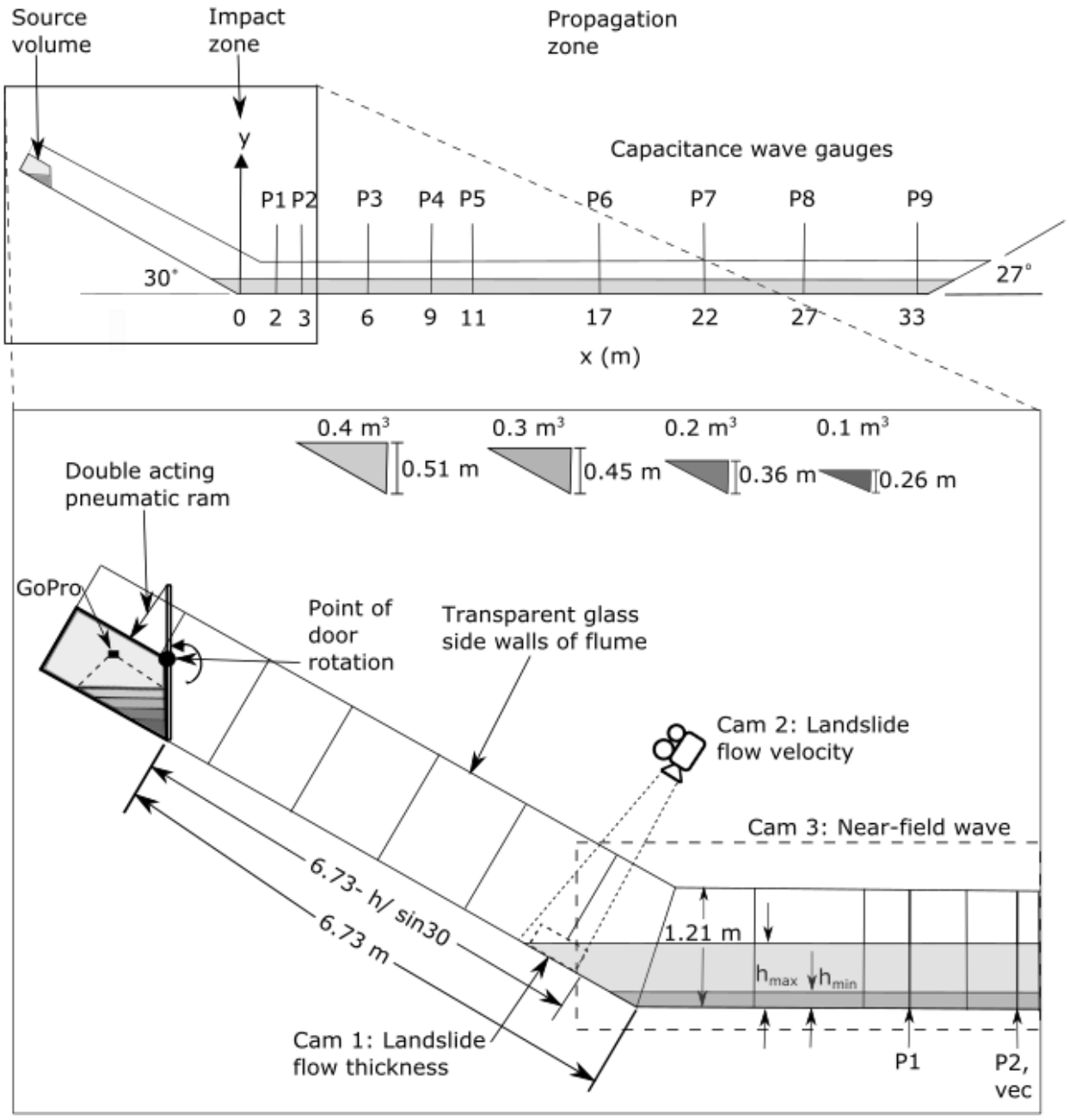

Figure 2.2: Experimental apparatus for measuring landslide generated tsunamis. The flume has nine probe locations from x = 2m to x = 33 m labelled P1 to P9. The detailed view of the landslide slope shows the field of view for each of the three cameras indicated by dashed lines and the location of the fluid velocity sensor (vec) and wave probes P1 and P2. Dimensions of each source volume and the range of water depths from h_{min} = 0.15 m to h_{max} = 0.65 m are indicated.

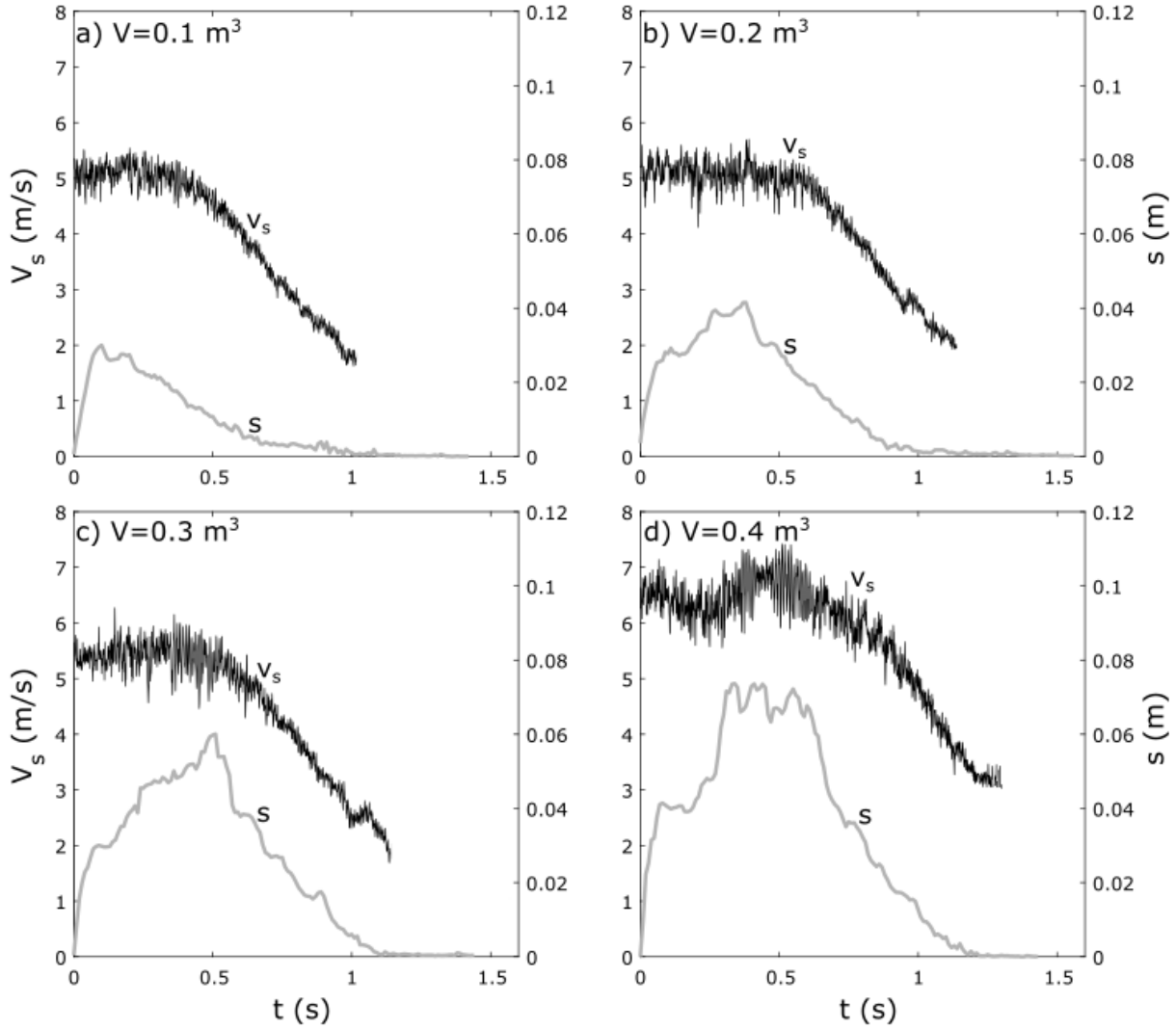

Figure 2.3: Landslide properties at impact for each for source volume. The velocity (v_s) is measured using PIV analysis of downward-looking images (Cam 2) and the thickness (s) is measured using side-looking images (Cam 1).

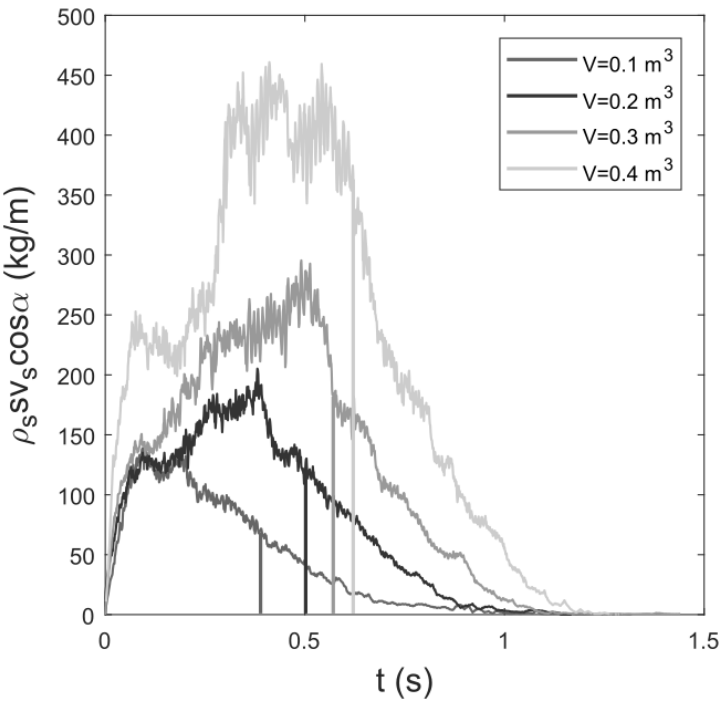

Figure 2.4: Time series indicating the rate of change of landslide momentum determined by the product of slide density, thickness and velocity. The vertical lines represent Δt_{M75} for each source volume.

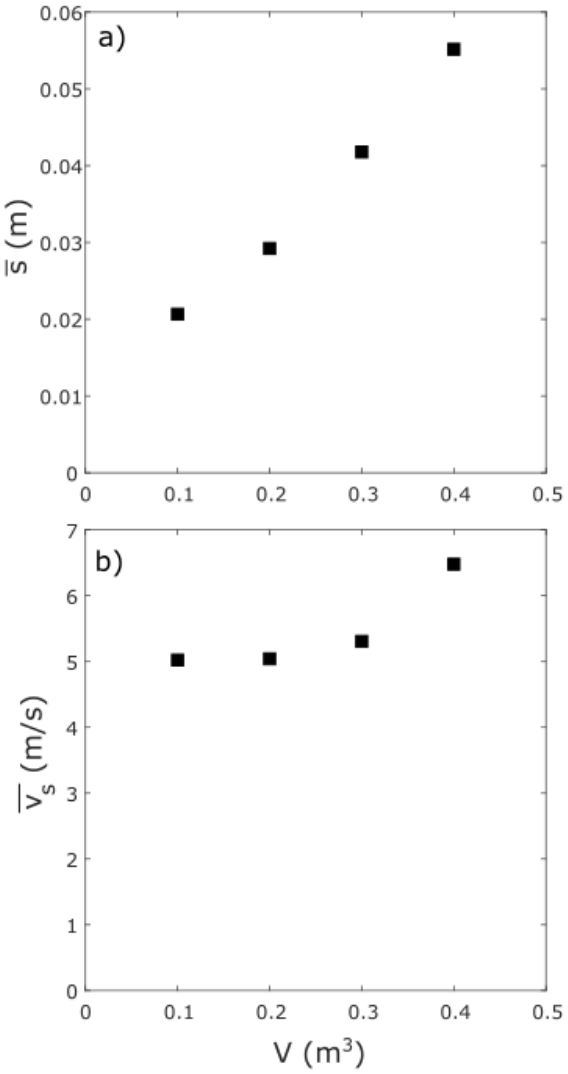

Figure 2.5: Mean values of the landslide parameters at impact, averaged over the time for 75% of the total momentum to impact the water Δt_{M75}.

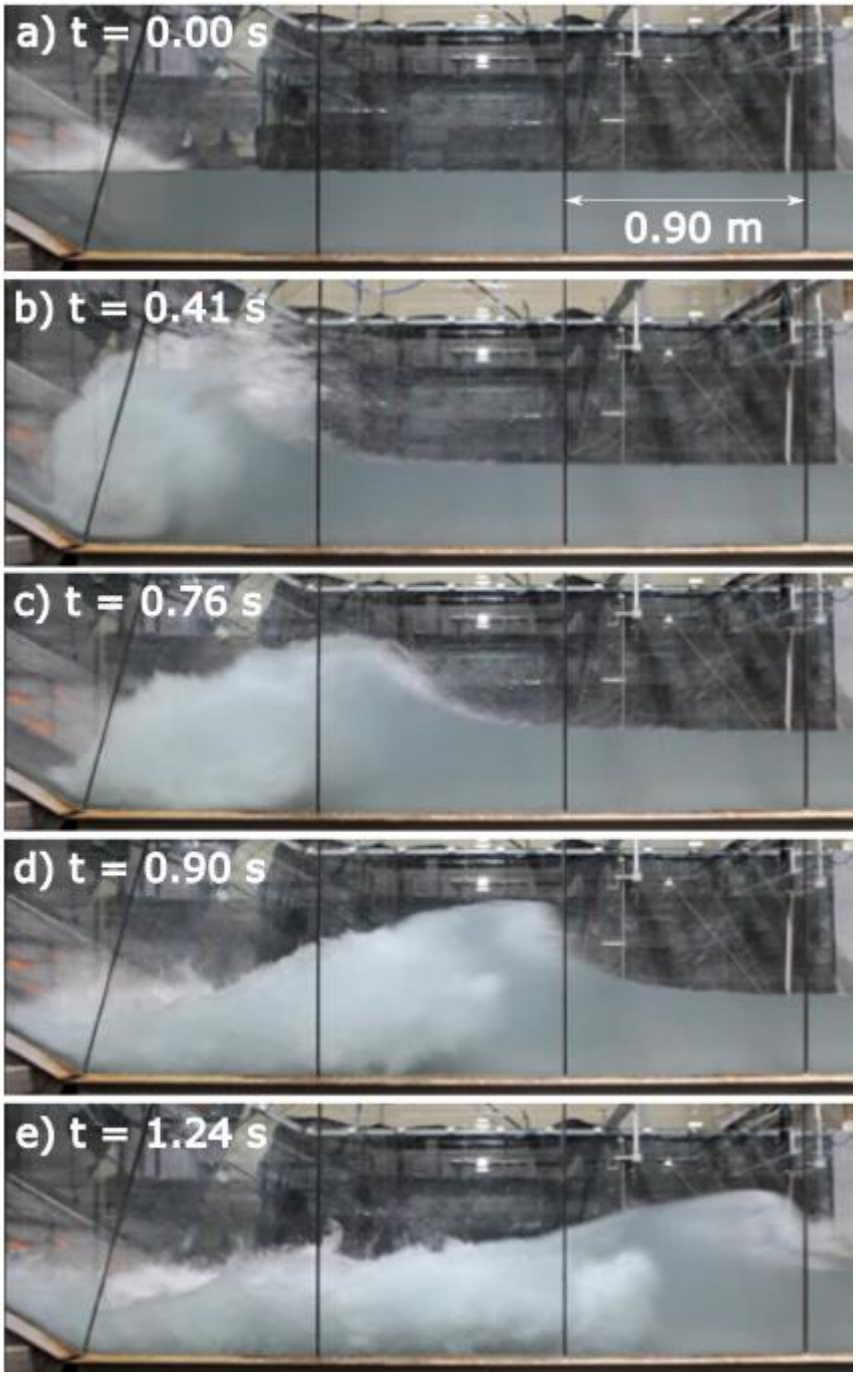

Figure 2.6: Time series of images from Cam 3 from the point of initial impact for the experiment with h = 0.30 m and V = 0.3 m^3, indicating generation of the surface wave and motion of the submerged turbulent landslide plume.

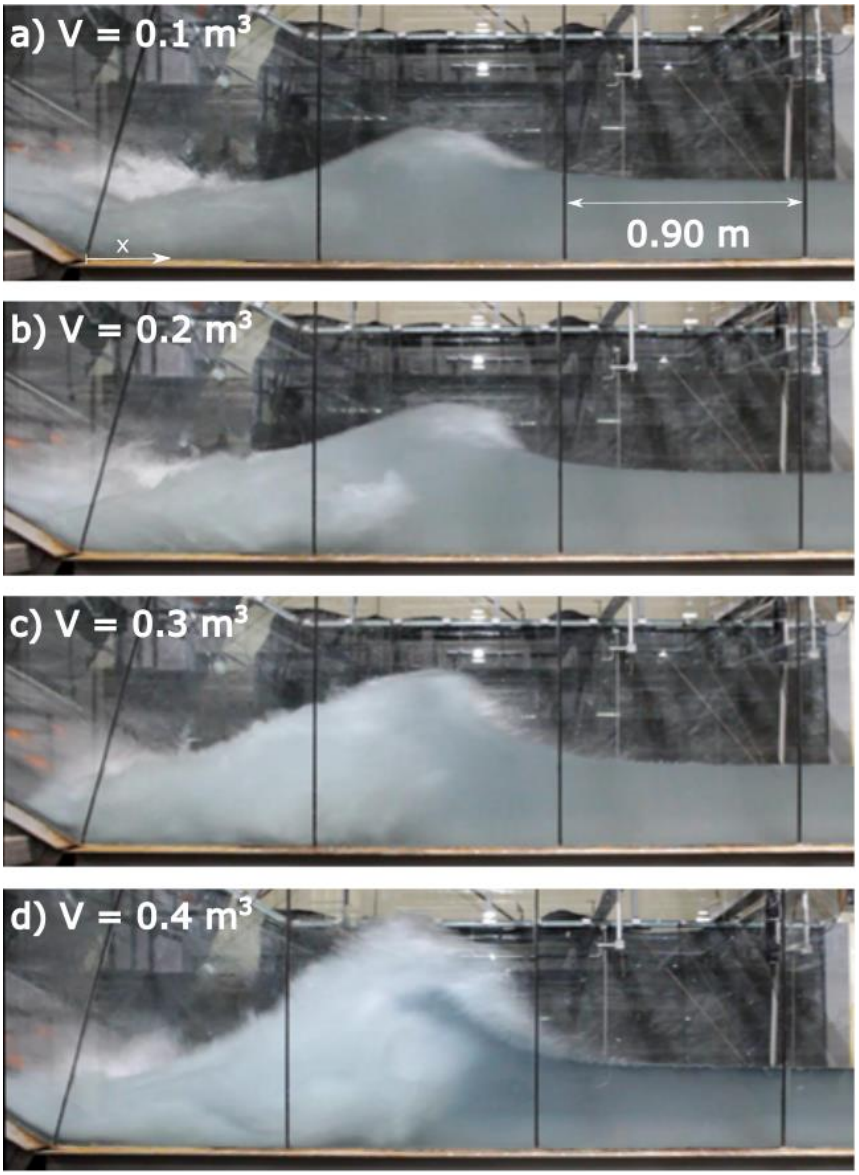

Figure 2.7: Selected images with h = 0.30 m for each source volume showing the maximum wave amplitudes at x = 1.2 m and the submerged turbulent landslide plumes.

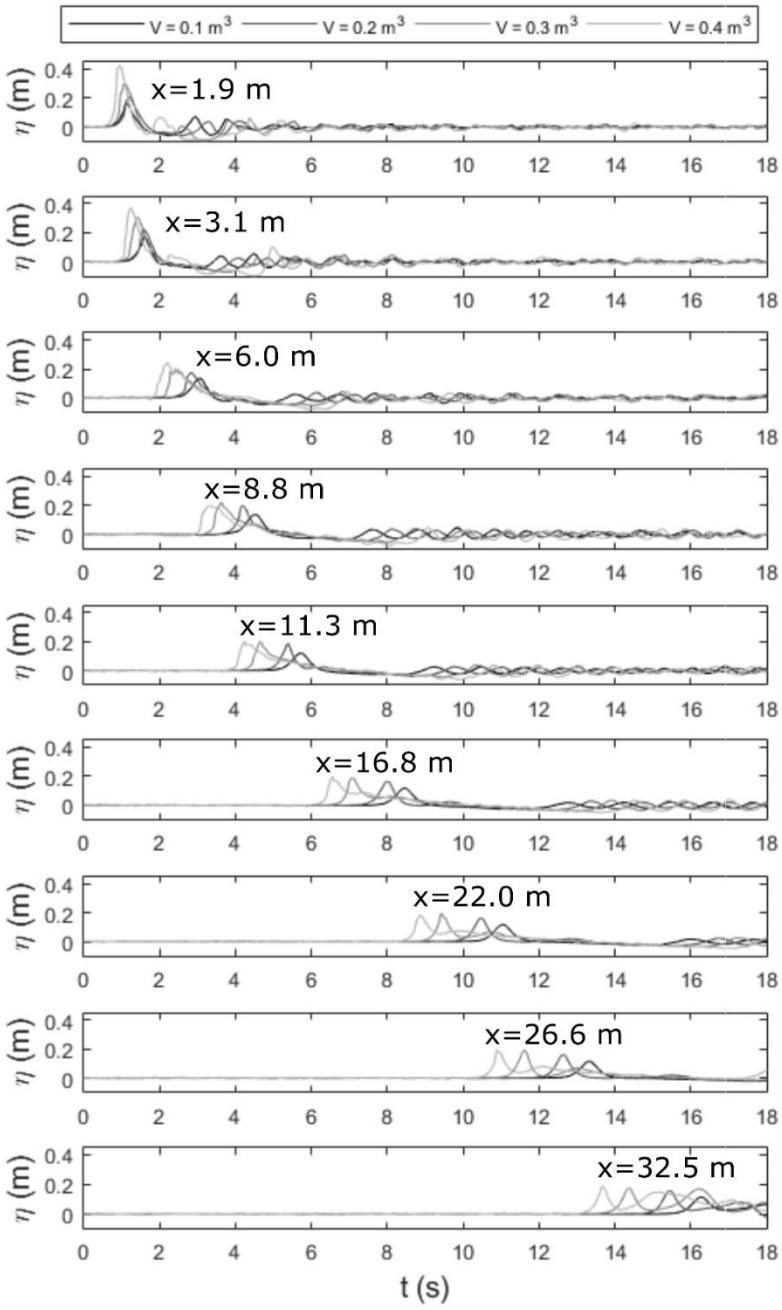

Figure 2.8: Water surface elevation profiles at wave probes (P1 at top to P9 at bottom) for *h* = 0.30 m and for each source volume, indicating the differences in wave amplitude and wave speed along the flume.

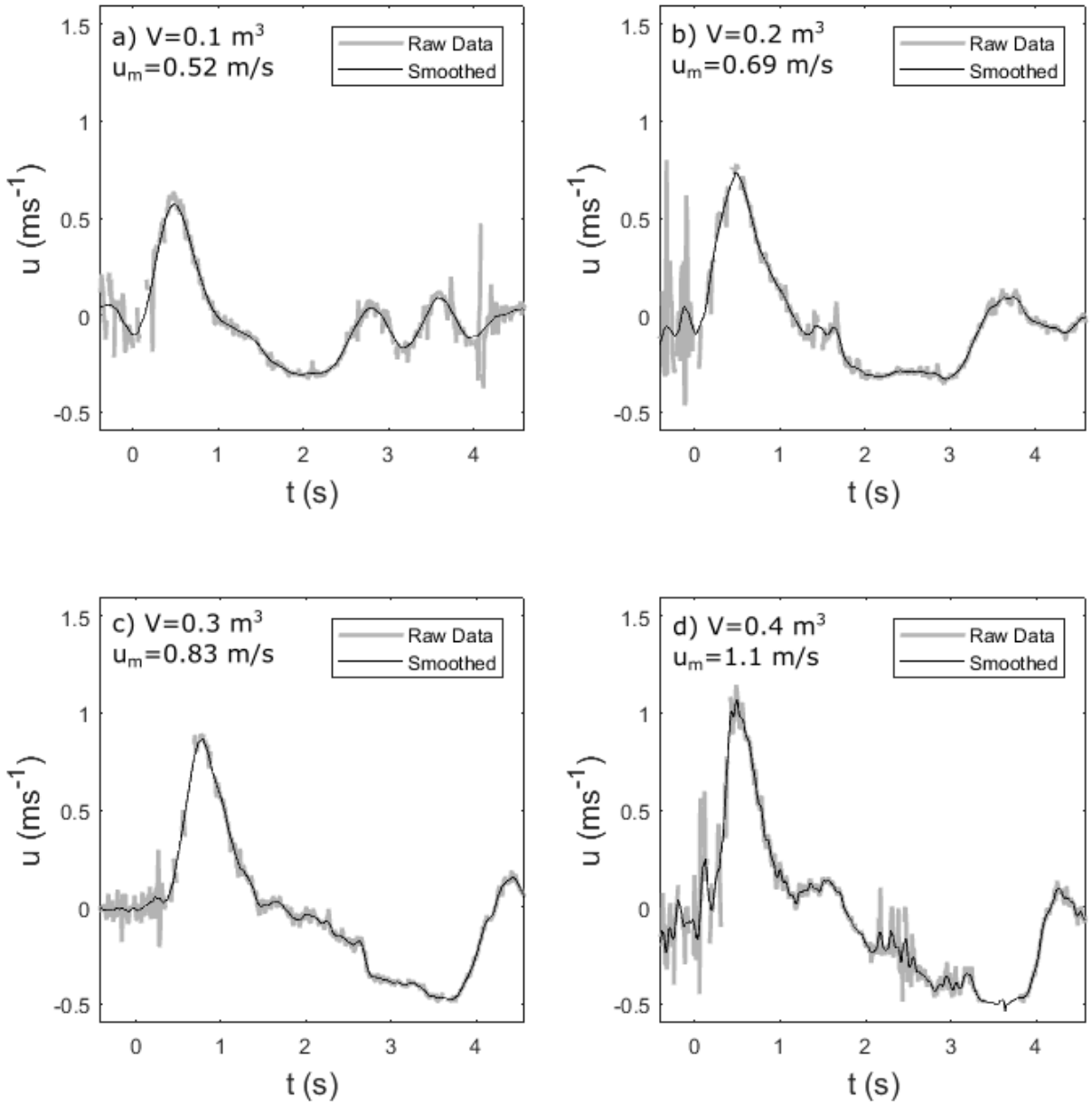

Figure 2.9: Near-bottom fluid velocity observations for each source volume in reservoir depths of *h* = 0.3 m, measured at *x* = 3.1 m. The raw data are measured at 100 Hz and the smoothed data have a lowpass filter applied to identify the maximum fluid velocity u_m.

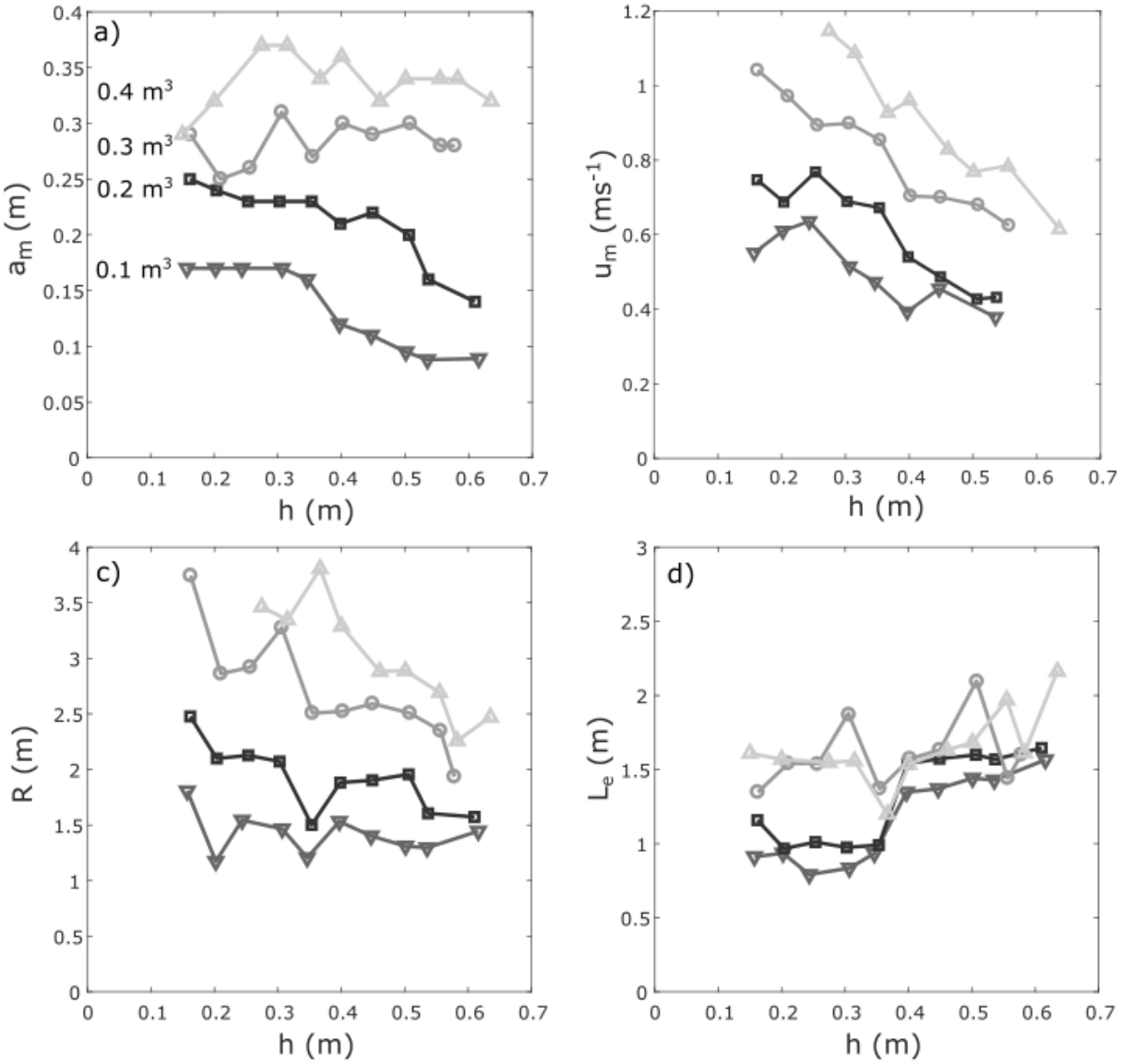

Figure 2.10: Observed wave properties in the near-field: a) maximum wave amplitude determined from the peak value of wave probe P2 at x = 3.1 m; b) maximum fluid velocity at h = 0.012 m above bottom measured using the acoustic sensor at x = 3.1 m; c) total runout R of the submerged landslide plume as measured using Cam 3; d) effective length of the slide at the point of wave release measured using Cam 3.

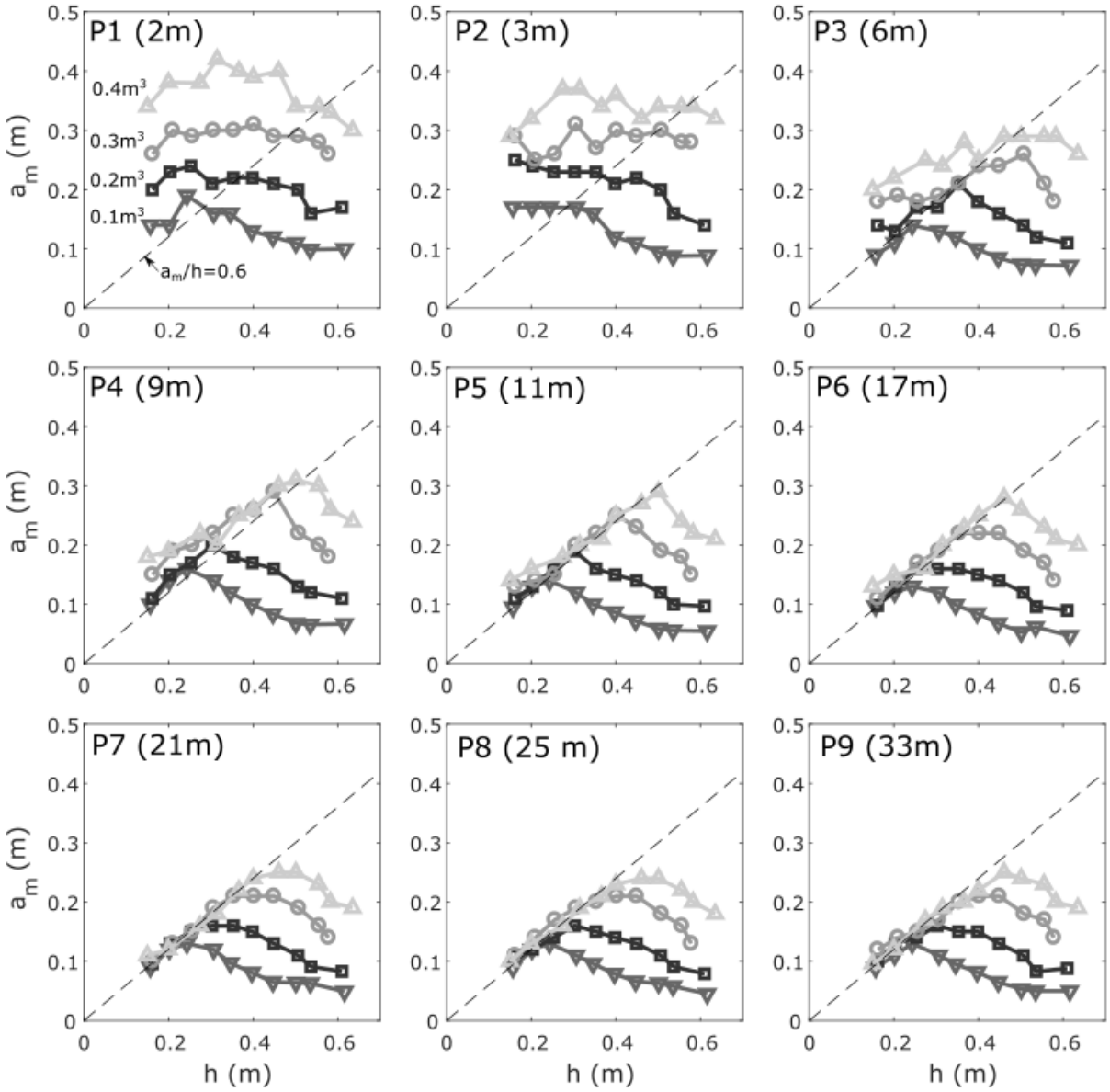

Figure 2.11: Maximum wave amplitude for each source volume measured at each wave probe, with dashed lines indicating a_m/h = 0.6.

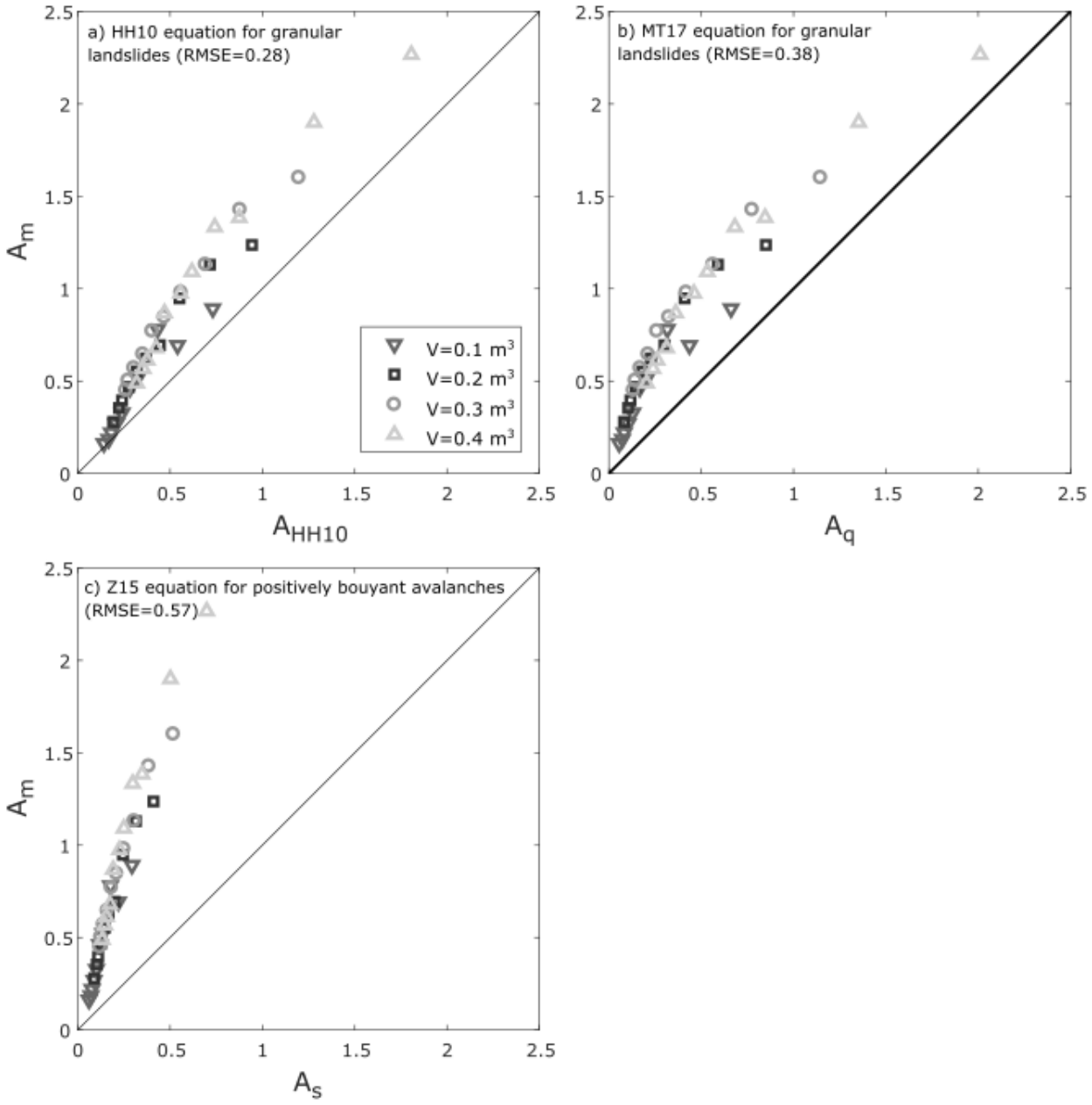

Figure 2.12: Comparison of the relative maximum amplitude ($A_m = a_m/h$) measured at P1 (x = 1.9 m) to previously developed equations, where the 1:1 line indicates perfect agreement: a) impulse product parameter applied to granular landslides, Eq. 2.5 (Heller and Hager, 2010); b) hydrostatic momentum equation for granular landslides, Eq. 2.12 (Mulligan and Take, 2017); c) impulse product parameter for positively buoyant avalanches, Eq. 2.7 (Zitti et al., 2015).

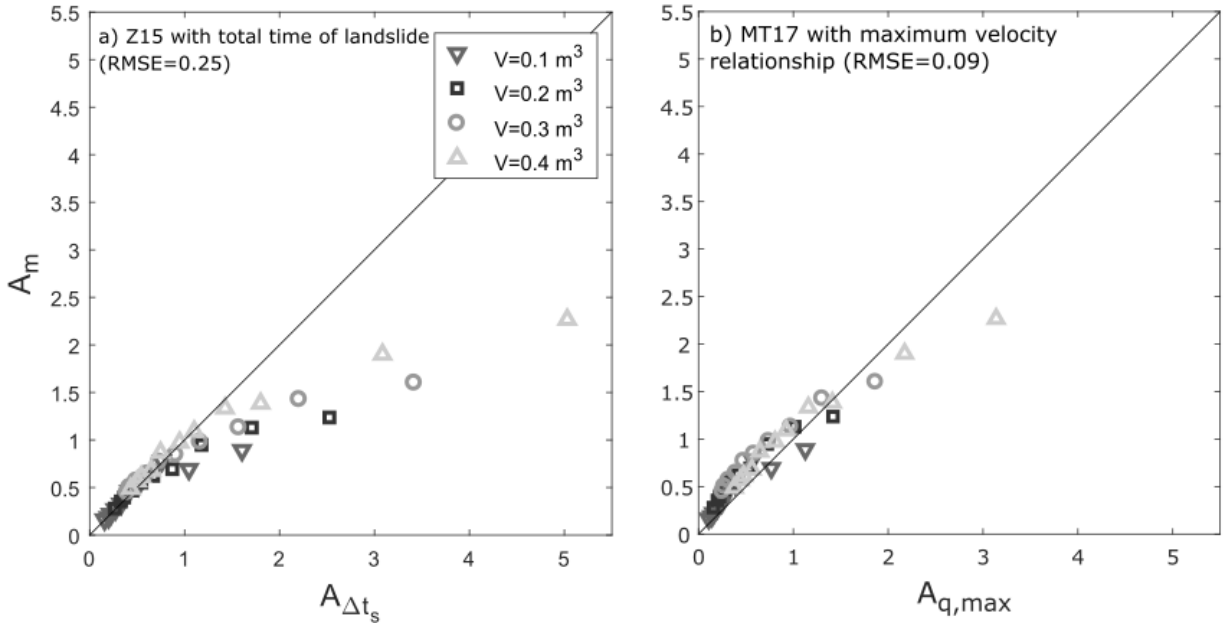

Figure 2.13: Comparison of the relative maximum amplitude ($A_m = a_m/h$) measured at P1 (x = 2 m) to previously developed equations that include consideration of the landslide time, where the 1:1 line indicates perfect agreement: a) impulse product parameter for positively buoyant avalanches that includes the total time of landslide Δt_s, Eq. 2.9 (Zitti et al., 2015); b) hydrostatic momentum equation for granular landslides (Mulligan and Take, 2017), using the maximum velocity relationship for highly mobile slides, Eq. 2.13, that yields Eq. 2.14.

Chapter 3

A novel framework to quantify the shape of landslide-generated tsunamis using wave asymmetry

3.1 Introduction

A landslide that falls or runs out into a body of water creates an impulse wave due to the rapid displacement of mass. A considerable amount of research has been invested into understanding this phenomenon by using physical models with solid blocks (e.g. Kamphuis and Bowering, 1970), granular material (e.g. Fritz et al., 2004; Heller and Hager, 2010; Miller et al., 2017) and highly mobile material including positively buoyant granular clay (Zitti et al., 2015) and water (Chapter 2). These studies focussed on using experimental data to develop predictive empirical equations for the maximum wave amplitude, with less attention on other wave characteristics such as the wave shape.

The shape of landslide-generated tsunamis have been investigated by comparing the wave profile from experimental observations (e.g., Wiegel et al., 1970) to wave theory (e.g., Noda et al., 1970) and developing classification methods (Huber, 1980; Fritz et al., 2004; Zweifel et al., 2006; Heller and Hager, 2011). Fritz et al. (2004) developed an empirical formula to classify waves into four categories based on the landslide properties of velocity and impact thickness including nonlinear oscillatory waves, nonlinear transition waves, solitary-like waves and dissipative transient bores. Heller and Hager (2011) examined wave profiles from experimental data and compared results to wave theories to classify the shape as stokes-like, cnoidal-like, solitary-like or bore-like waves. Limiting the classification of these waves into discrete categories causes ambiguity in transition zones between these wave types and this information, however valuable, has limited applicability in developing boundary conditions for numerical models.

Laboratory experiments of earthquake-generated tsunamis are commonly conducted in wave basins, where a paddle is using to generate the initial wave. These studies typically use a simple wave signal at the offshore boundary, such as a solitary positive wave (Baldock et al, 2009) or an error function to increase the inundation time compared to a regular solitary wave (Reuben et al, 2011). These tsunamis rapidly become asymmetric in shape as they propagate away from the paddle, and the wave shape has been shown to be very important in controlling the overland flow (Reuben et al, 2015). The shape of wind-generated waves is known to play a major role in sediment transport on beaches and is typically quantified by the asymmetry (*As*) of the water surface time series (Elgar and Guza, 1985; Doering and Bowen, 1995). Asymmetry is used to quantify the degree of wave symmetry about the vertical axis. A perfectly symmetric wave has $As = 0$, while a pitched-forward wave with a steep front face has $As < 0$ and a wave with a flatter front has $As > 0$. Wave shape not only influences the wave amplitude as it propagates but also influences the orbital velocity, sediment transport and wave impact forces (Peregrine, 2003; Hsu and Hanes, 2004). For landslide-generated tsunamis, understanding the near-field wave shape and how it evolves with distance is crucial in order to accurately assess the far-field wave characteristics, which can be used to assess the hazard some distance away.

In this study, a new method for calculating and classifying near-field landslide-generated wave shape is presented. Using experimental data, the asymmetry of the wave profile is used to quantify the wave shape. The problem is defined in Figure 3.1, where breaking waves that are asymmetrical in the near-field can experience a significant reduction in the maximum amplitude (a_m) as they evolve with distance into more symmetrical waves with $As \approx 0$, whereas non-breaking waves experience very little change in a_m as they propagate away from the source over constant depth. The experimental results are used to develop new predictive equations to express the water surface elevation time series as a continuous function of a_m and *As* for the source conditions as a landslide impacts water. These equations describe the wave shape and can be used along with predictive methods for maximum wave amplitude to develop the near-field boundary conditions needed for numerical simulations of landslide tsunami propagation in the far-field.

These models can be applied to different areas of concern and can properly account for varying bathymetry and three-dimensional wave dissipation.

3.2 Materials and Methods

3.2.1 Laboratory Experiments

Experimental observations were collected of impulse-generated waves using the Queen's University landslide flume. The flume is comprised of a 6.73 m long 30° slope connected to a 33.8 m long base, shown in Figure 3.2. The flume is 2.10 m wide and has sidewalls that are 1.21 m in height. The sidewalls of the inclined portion of the flume are transparent glass, which continues for 3.7 m along the base before transitioning to smooth concrete. At the end of the flume there is a 2.7 m long run-up ramp sloped at 27°. The source volume for the landslide is held in an aluminium box with a maximum capacity of 1.68 m^3. When the release box is triggered, the gate swings open about a hinge at the top at a tip angular velocity of 1 ms^{-1}. Water is used as the sliding material. With zero internal shear strength, this material is hypothesised to present an upper bound of landslide mobility, representative of highly mobile landslides such as a mudflow, water-saturated debris flow, or liquefied soil that behaves as a fluid. The use of water makes the experimental process very efficient, with rapid set-up and clean-up for each test, allowing many tests to be conducted and a wide parameter space to be investigated.

To measure the water surface elevation, a Canon T5i camera (Cam 1) was placed 3.2 m from the side of the flume where the field of view includes the impact at the sliding water to the edge of the tempered glass. The camera is used to record images at 29 Hz, with a resolution of 1929x1101 pixels and is used to observe the waves in the near-field region (Figure 3.3). The waves were also measured along the flume centreline using nine 0.6 m long wave probes (Akamina AWP-24 Wave Height Gauges) located at stations P1-P9 that sampled the water surface elevation (η) at 100 Hz located at x = 1.9, 3.1, 6.0, 8.8, 11.3, 16.8, 22.0, 26.6 and 32.5 m from the origin at the base of the landslide slope. The probes are accurate to $\pm$0.001 m and simultaneously collect the observations with a 16-bit/1-MHz USB data acquisition system.

A total of 41 tests were completed using four source volumes that increased incrementally from 0.1-0.4 m^3 in water depths ranging from 0.15-0.65 m in increments of 0.05 m, generating a wide range of wave types.

3.2.2 Quantifying the Wave Shape

The wave shape is quantified by calculating the asymmetry, defined as the skewness of the Hilbert transform of the time series (Elgar and Guza, 1985), and an example of a perfectly symmetrical wave about the vertical axis is the sine function. The Hilbert transform is described by Elgar et al. (1990) for a pitched forward triangular saw-tooth time series, which is highly skewed and thus has high *As*. In the present study, the asymmetry of landslide-generated waves are calculated for the leading wave in each water surface elevation time series measured at P1-P9. The "zero-crossing points", shown as red circles in Figure 3.3, define the time in which the Hilbert transform is applied to each time series. This method is used to distinguish three distinct types of waves observed with different values of *As.* Negatively asymmetric waves are pitched forward in space and therefore the steeper side occurs first in time as shown in Fig. 3.3a. The most extreme example of an asymmetric wave with a vertical front would produce a wave with *As* = -2.2. Symmetric waves (Fig. 3.3b) have the same steepness on the front and back of the wave. Positively asymmetric have a flatter front face which occurs first in time, before the steeper back side (Fig 3.3c). The largest value of asymmetry which is possible using this method is *As* = 2.2, which would occur with a shallow front slope and a vertical back side. These waves, along with the near-symmetric waves, can also have a shallow trough trailing the leading wave.

3.3 Results and Analysis

3.3.1 Wave Characteristics

For each landslide experiment, water surface elevation measurements at the nine wave probes are used to investigate the characteristics of the near-field waves in terms of maximum amplitude (quantified by a_m)

and wave shape (quantified by *As*), and the evolution of these characteristics along the length of the flume. Examples of time series data collected at P1, with video imagery of the corresponding shape, are provided for three cases with different *As* in Figure 3.3. Scatter plots of these wave characteristics are shown in Figure 3.4 at selected probe locations including the most near-field site (P1), an intermediate distance (P5) and the most far-field (P9) as functions of the water depth (*h*). At P1, the wave has been fully generated by the slide but has not had space over which to break or significantly evolve in shape. This is indicated by the near-horizontal lines in Figure 3.4a, signifying that the initial wave amplitudes are nearly independent of *h*, and the waves have a wide range of initial asymmetry values from -1.2 to 0.7.

At the intermediate distance (P5), the maximum amplitude is strongly influenced by the water depth, and each landslide source volume results in a higher depth at which the peak maximum amplitude occurs (Figure 3.4c). This indicates there are some tests affected by wave breaking. The tests in which $As < 0$ in the near-field (P1) are the tests which experience a drastic reduction in a_m and *As* at P5 (Figure 3.4 c, d).

The amplitudes of the far-field waves (P9) are similar to those measured at the intermediate distance (Figure 3.4 e). This indicates that each wave has reached a stable state and the near-zero asymmetry of each far-field wave (Figure 3.4 f) shows that the wave shapes are all symmetrical at this distance.

3.3.2 Wave Shape Variability with a_m and h

The Solitary Wave Theory criterion (Grilli et a., 1997) defines the limiting wave height in a given water depth, which can be expressed as

$$\frac{a_m}{h} \approx 0.80 \qquad \text{(Eq 3.1)}$$

where a_m is the maximum wave amplitude in a given water depth *h*. This expression indicates that any wave which exceeds the maximum stable depth-limited amplitude will break, resulting in an immediate decrease in amplitude. In comparison to the observations, the relationship described in Eq 3.1

overestimates the wave amplitude in the far-field and a better representation of the limiting wave amplitude is described by Eq 3.2.

$$\frac{a_m}{h} = 0.60 \qquad \text{(Eq 3.2)}$$

This indicates a new breaking wave limitation for impulse generated waves where the stable maximum wave amplitude for a given depth is lower than anticipated using the Solitary Wave Theory criterion. Eq 3.2 is used to distinguish between positive and negatively asymmetrical waves in the near-field as shown in Figure 3.4b. Asymmetry in the near-field for positively asymmetrical waves is inversely proportional to a_m/h whereas negatively asymmetrical breaking waves are not a function of a_m/h in the near-field. As the waves propagate to the far-field, the + *As* waves decrease slightly to become more symmetrical while the - *As* waves become more asymmetrical before evolving into near-solitary waves (Figure 3.4d, f). Therefore, major changes in *As* as the waves propagates are coincident with a major decrease in a_m/h for – *As* waves, while the +*As* waves experience very little change in both *As* and a_m/h with *x*.

The continuous evolution of wave shape for each source volume is shown in Figure 3.5, which compares the evolving wave asymmetry for each test performed for each landslide volume. This clearly demonstrates that two distinct types of behaviour are separated by the relationship given by Eq 3.2. Each wave reaches $As \approx 0$ at a different *x*, and tests that have $As \approx 0$ near $x \approx 2$ m remain stable along the length of the flume. Waves with positive asymmetry, where $a_m/h < 0.6$ at P1, demonstrate gradual decrease in *As* as the wave shape becomes more symmetrical. In general, more asymmetrical waves in the near-field require a longer distance to reach a stable state where the shape becomes nearly independent of distance.

Eq 3.2 can also be applied to distinguish between rapidly decreasing and slowly decaying wave amplitudes as indicated in Figure 3.6, where all wave amplitudes that exceed this relationship attenuate until this limit is reached. The distance at which the waves become stable is indicated by the point at

which $As \approx 0$ and is directly related to the initial maximum amplitude measured at P1, where a higher a_m at this location requires a longer distance until a stable wave shape is achieved.

The shape of rapidly evolving breaking waves in the near-field cannot be evaluated solely as a function of a_m/h. Therefore, a length scale x_b has been introduced to quantify the distance each wave propagates before it attenuates to below the limit $a_m/h = 0.6$. This zone represents a near-field distance of higher hazard, where higher fluid velocities and impact forces must be considered. This relationship has been evaluated for 23 tests with breaking waves, defined when $a_m/h > 0.6$ at P1 and shown in Figure 3.4a. The relationship describing the length scale at which both Eq 3.2 and $As \approx 0$ is reached are quantified by Equation 3.3 and 3.4.

$$\frac{x_b}{h} = 82.8 \frac{a_m}{h}_{@P1} - 46.7 \quad \text{(Eq 3.3)}$$

$$As = -156 \frac{x_b}{h} + 24.3 \quad \text{(Eq 3.4)}$$

These relationships are given by best fit equations to the tests where breaking waves were observed at P1, are shown in Figure 3.7, and are valid where $x_b/h > 10$.

3.3.3 A Modified Equation for Wave Shape

The solitary wave solution, developed by Boussinesq (1872) and Rayleigh (1876), is commonly used to analyze the runup of tsunamis (Goring, 1978; Liu et al., 1991; Yeh et al., 1994; Synolakis and Berknard, 2006) and is given by Eq. 3.5.

$$\eta(x,t) = a \operatorname{sech}^2 \left[\sqrt{\frac{3}{4}\frac{a}{h^3}} (x - c_s t) \right] \quad \text{(Eq. 3.5)}$$

where

$$c_s = \sqrt{g(a+h)} \quad \text{(Eq.3.6)}$$

This equation expresses the water level elevation η in terms of the wave amplitude a, water depth h, and wave celerity c_s with respect to distance x, time t and gravitational acceleration g. The solitary wave solution describes a perfectly symmetrical wave. Observations from the present study indicate that landslides can produce a wide variety of wave shapes with different skewness about the vertical axis. To predict the near-field wave shape, the solitary wave equation has been modified to account for the asymmetry. Following the approach by Madsen et al. (2008) in developing a horizontal scale coefficient for a symmetrical solitary wave, two separate horizontal scale coefficients A and B are developed and are used in solitary wave equations (Eq. 3.7 and 3.8) for the front side and the back side of the wave, providing a mathematical description of a wave that can be pitched forward or backward.

$$\eta_1(x,t) = a\,\mathrm{sech}^2\left[A\sqrt{\frac{3}{4}\frac{a}{h^3}}(-c_s t)\right] \qquad \text{for } t < 0 \qquad \text{(Eq 3.7)}$$

$$\eta_2(x,t) = a\,\mathrm{sech}^2\left[B\sqrt{\frac{3}{4}\frac{a}{h^3}}(-c_s t)\right] \qquad \text{for } t \geq 0 \qquad \text{(Eq 3.8)}$$

$$\eta(x,t) = [\eta_1\ \eta_2] \qquad \text{for all } t \qquad \text{(Eq 3.9)}$$

where

$$A = 0.86 \qquad \text{(Eq 3.10)}$$

$$B = 0.86e^{\frac{5\pi}{9}As} \qquad \text{(Eq 3.11)}$$

Here, $x = 0$ is applied to represent a stationary location and describe the water surface variation only over time. The two sides of the wave are combined in Eq. 3.9, which can be used to continuously describe the different types of near-field wave shape based on the asymmetry (positive, near-zero, negative) that are observed in the experiments.

To express the wave time series as a function of wave shape, the water surface asymmetry needs to be computed within a defined length of time. However, the solitary wave equation approaches but does not cross zero, and therefore the "zero-crossing" points cannot be used. Therefore, the time over which to evaluate *As* has been defined by the time when η is greater than 0.7% of the maximum amplitude a_m as suggested by Kobayashi and Karjadi (1994) for solitary waves. The *A* and *B* values were then iterated until the asymmetry matched the value determined from observations at P1 for each test.

The value of *A* has low variability with values ranging from 0.65 to 1.1 for $-1.2 < As < 0.6$ over the 41 tests. The mean value of $A = 0.86$ produced the best fit to the wave shape at P1, and therefore *A* is taken to be a constant. Since the horizontal scale factor describing the front side of the wave is constant for all tests across a range of depths, this suggests that the solitary wave equation has a consistently steeper front face than what has been observed during this study. The values of *B* change significantly with *As*, and the relationship is summarized in Fig 3.8. For positively asymmetrical waves, which occur for small a_m and large *h*, the *B* coefficient has a high value. This results in a steeper slope of the trailing edge, creating waves with $As > 0$. The negative asymmetry waves are simulated by reducing the steepness of the trailing edge and therefore results in a steeper slope on the leading edge. A perfectly symmetrical wave with $As = 0$ occurs when $B = 0.86$.

This method allows for a continuous solution for the near-field water surface profile given the water depth *h*, maximum wave amplitude a_m and wave asymmetry *As*. Three cases are numerically generated and presented in Fig. 3.9, indicating the dependence of *B* on *As*, where positive asymmetry results for $B > 0.86$, symmetrical waves occur for $B = 0.86$, and negative asymmetry occurs when $B < 0.86$. The wave asymmetry just after a landslide generates the wave strongly depends on the characteristics of the slide and receiving water body.

3.4 Application and Discussion

Asymmetry in the generation zone is an important descriptor of the initial wave shape. A colour contour map describing how *As* varies with water depth and wave amplitude is shown in Figure 3.10. In this plot *As* = 0 is shown in white and negative/positive *As* is shown in red/blue. Eq 3.2 corresponds to $As \approx 0$ for all tests, and it is remarkable how well the wave breaking limit coincides with the symmetrical waves. This map can be used to predict the shape of a near-field tsunami in the parameter range of the present study. For given input conditions (a_m, h), this plot can be used to determine the near-field *As* that can in turn be used in Eq. 3.9 to generate a time series that matches the observations for the near-field wave probe at P1. This is shown in Figure 3.11 for four cases, each using a depth of h = 0.4 m due to the large variation in *As* with slide volume. The amplitudes and depths of each test are known and the resulting predicted wave shapes compared to the raw data. There is very good agreement between the observations and predictions, evidenced by the high root mean squared error (RMSE < 0.017) in each case.

3.4.1 Wave Shape Prediction

In order to map the new method of quantifying wave type based on asymmetry to a previous qualitative description of wave shape by Fritz et al. (2004), the new data are shown on a dimensionless plot of the landslide parameters of the relative landslide thickness ($S = s/h$) and Froude number ($F = v_s/(gh)^{1/2}$). The four wave types classified by Fritz et al. (2004) are non-linear oscillatory waves, non-linear transition waves, solitary waves and transient bores indicated by I-IV respectively in Figure 3.12. Combining these classifications with the measured asymmetry for the experiments conducted in this study can give approximations of asymmetry for each wave classification as defined by Fritz et al. (2004): I ($As > -0.2$); II ($-1 < As < -0.2$); III ($As < -1$) and IV was not observed. The lower limit of the non-linear transition waves corresponds well to the change in behaviour from negative breaking waves to positive non-breaking waves. This threshold is described by the relationship $F = 4\text{-}7.5S$, and can be used to distinguish breaking and non-breaking waves in the near-field.

Recasting the solitary wave equation to include asymmetry and describe the landslide-generated waves allows wave evolution over time and space to be predicted, by generating the necessary boundary conditions for phase-resolving wave models. The maximum wave amplitude for these boundary conditions can be predicted using methods developed in previous studies such as Mulligan and Take (2017) or Heller and Hager (2010). With numerical models, wave properties including the wave celerity, fluid velocity, water surface amplitude and wave runup can be evaluated for any bathymetric conditions. This method can be applied to calculate the near-field wave time series given the wave amplitude, wave asymmetry and water depth.

3.4.2 Limitations

The results for wave evolution with distance from the source are applicable for the parameter range tested in this study in a two-dimensional flume with a constant depth. In field cases, an impulse wave would dissipate much faster in three-dimensions due to radial spreading of the wave energy (Fritz et al., 2004). Wave transformation processes, such as diffraction and refraction, would also change the far-field amplitude. The understanding between how wave asymmetry influences wave amplitude would in theory remain the same in three-dimensions, however, this has yet to be investigated. The new condition describing the breaking wave limit (Eq 3.2) should be further investigated in order to determine the limitations in terms of scalability with field-cases and applicability with three-dimensional physical models.

A limitation in using the solitary wave equation is that it can only be used to generate the shape of the first crest and trailing edge until $\eta = 0$, and therefore can only be used for the positive deflections of the water surface. It does not include the wave trough that could occur, which are observed in the present study in cases with $h > 0.3$ m that have $As \geq 0$. Examples of this are shown in Figure 3.3. The effects of how this can influence the wave properties during wave propagation is currently unknown, however

simulations using testing using phase-resolving numerical models could be used to examine the accuracy of this approach.

This method has been proven to quantifiably match the shapes of all waves produced in this study in the near-field. However, Madsen et al. (2008) describes the difficulties in applying the solitary wave equation to long period waves on a sloping bottom, and therefore the effects of bathymetric variations should also be investigated. Madsen et al. (2008) also describes the limitations of applying the solitary wave equation to geophysical scale tsunamis, as the effects of scaling coefficients are unknown and should be applied to and compared with field observations when available.

3.5 Summary and Conclusions

The impulse waves produced in this experimental study vary greatly in shape from steep fronted waves breaking waves to deep water waves with a flatter front face. These shapes have been quantified using the asymmetry about the vertical axis between the zero-crossing points of the wave. The wave shape in the near-field can be evaluated by using the parameters of a_m and h that were observed in this study and can also be estimated using the relative slide thickness and Froude number of the landslide.

The results can be used to differentiate between waves with negative and positive asymmetry, which behave very differently in the far-field. Negatively asymmetric breaking waves can rapidly decrease in amplitude until $a_m/h \approx 0.6$ and then remain relatively constant, whereas waves with positive or near-zero asymmetry attenuate less in space. In terms of wave shape, breaking waves become more asymmetric as they propagate before evolving into a solitary wave. The point at which the wave evolves into a solitary wave depends on the initial value of a_m/h. The distance it takes for each wave to become a stable solitary wave with respect to a_m can be quantified. This provides a distance in which there is an additional risk of high impact forces due to wave shape.

The solitary wave equation has been used as the basis for defining the range of wave shapes based on asymmetry about the vertical axis. In order to simulate the wave shape as a continuous function of time, two shape coefficients (*A*, *B*) have been developed to control the water surface slope at the leading and trailing edge of the wave. It has been found that $A = 0.86$ for all tests and therefore the solitary wave equation overestimates the steepness of the leading edge by the same amount for every test at each depth. The *B* coefficient describing the trailing edge of the wave varies significantly with *As*, which can be described as a function of *As*. The inclusion of these coefficients in the solitary wave equation is shown to accurately predict all the wave shapes observed at the closest wave gauge to the impact site in the experiments conducted herein.

Future work could employ a phase-resolving numerical wave model to determine the validity of this method in the far-field, for cases with realistically varying bathymetry. Additional work could also be completed to investigate the importance of simulating the shallow wave troughs that follow the higher initial wave amplitudes and occur in this study for the cases with high or near-zero values of *As*. This new and novel method of quantifying the wave shape by modifying the solitary wave equation to include asymmetry can be used to generate more accurate boundary conditions for numerical models, which could be applied to improve tsunami hazard evaluation and reduce risk to human life and property in mountainous coastal regions.

3.6 References

Baldock, T.E., Cox, D., Maddux, T., Killian, J. and Fayler, L. (2009). Kinematics of breaking tsunami wavefronts: A data set from large scale laboratory experiments. *Coastal Engineering*, *56*(5), 506-516.

Boussinesq, J. (1872). Theorie des ondes et des remous qui se propagent le long d'un canal rectangulaire horizontal, en communiquant an liquide contenu dans ce canal de vitesses sensiblement pareilles de la surface anfond, Liouvilles. *J. Math.*, *17*, 55-108.

Doering, J.C. and Bowen, A.J. (1995). Parametrization of orbital velocity asymmetries of shoaling and breaking waves using bispectral analysis. *Coastal Engineering*, *26*(1-2), 15-33.

Elgar, S. and Guza, R.T. (1985). Observations of bispectra of shoaling surface gravity waves. *Journal of Fluid Mechanics*, *161*, 425-448.

Elgar, S., Freilich, M.H. and Guza, R.T. (1990). Model-data comparisons of moments of nonbreaking shoaling surface gravity waves. *Journal of Geophysical Research: Oceans*, *95*(C9), 16055-16063.

Fritz, H.M., Hager, W.H. and Minor, H.E. (2004). Near field characteristics of landslide generated impulse waves. *Journal of Waterway, Port, Coastal, and Ocean Engineering*, *130*(6), 287-302.

Goring, D.G. (1978). Tsunamis--the propagation of long waves onto a shelf.

Grilli, S. T., Svendsen, I. A., & Subramanya, R. (1997). Breaking criterion and characteristics for solitary waves on slopes. *Journal of Waterway, Port, Coastal, and Ocean Engineering*, *123*(3), 102-112.

Heller, V. and Hager, W.H. (2010). Impulse product parameter in landslide generated impulse waves. *Journal of Waterway, Port, Coastal, and Ocean Engineering*, *136*(3), 145-155.

Heller, V. and Hager, W.H. (2011). Wave types of landslide generated impulse waves. *Ocean Engineering*, *38*(4), 630-640.

Hsu, T.J. and Hanes, D.M. (2004). Effects of wave shape on sheet flow sediment transport. *Journal of Geophysical Research: Oceans*, *109*(C5).

Huber, A. (1980). Schwallwellen in Seen als Folge von Felsstürzen (Reservoir Impulse Waves Caused by Rockfall). VAW Mitteilung 47, Versuchsanstalt für Wasserbau, Hydrologie und Glaziologie, ETH Zürich.

Kamphuis, J.W., and Bowering, R.J. (1970). Impulse waves generated by landslides. *Proc., 12th Coastal Engineering Conf.*, ASCE, REST, Va. 1. 575-588.

Kobayashi, N. and Karjadi, E.A. (1994). Surf-similarity parameter for breaking solitary-wave runup. *Journal of Waterway, Port, Coastal, and Ocean Engineering*, *120*(6), 645-650.

Liu, P.L.F., Cho, Y.S., Briggs, M.J., Kanoglu, U. and Synolakis, C.E. (1995). Runup of solitary waves on a circular island. *Journal of Fluid Mechanics*, *302*, 259-285.

Madsen, P.A., Fuhrman, D.R. and Schäffer, H.A. (2008). On the solitary wave paradigm for tsunamis. *Journal of Geophysical Research: Oceans*, *113*(C12).

McDougall, S. (2016). 2014 Canadian Geotechnical Colloquium: Landslide runout analysis—current practice and challenges. *Canadian Geotechnical Journal*, *54*(5), 605-620.

Miller, G.S., Take, W.A., Mulligan, R.P, and McDougall, S. (2017). Tsunamis generated by long and thin granular landslides in a large flume. *Journal of Geophysical Research: Oceans,* 122,653-668, DOI: 10.1002/2016JC012177.

Mulligan, R. P., & Take, W. A. (2017). On the transfer of momentum from a granular landslide to a water wave. *Coastal Engineering*, *125*, 16-22.

Noda, E. (1970). Water waves generated by landslides. *Journal of the Waterways, Harbors and Coastal Engineering Division*, *96*(4), 835-855.

Peregrine, D.H. (2003). Water-wave impact on walls. *Annual Review of Fluid Mechanics*, *35*(1), 23-43.

Rayleigh, L. (1876). On waves. *Phil. Mag.*, *1*, 257-259.

Rueben, M., Holman, R., Cox, D., Shin, S., Killian, J. and Stanley, J. (2011). Optical measurements of tsunami inundation through an urban waterfront modeled in a large-scale laboratory basin. *Coastal Engineering*, *58*(3), 229-238.

Rueben, M., Cox, D., Holman, R., Shin, S. and Stanley, J. (2014). Optical measurements of tsunami inundation and debris movement in a large-scale wave basin. *Journal of Waterway, Port, Coastal, and Ocean Engineering*, *141*(1), 04014029.

Synolakis, C.E. and Bernard, E.N. (2006). Tsunami science before and beyond Boxing Day 2004. *Philosophical Transactions of the Royal Society of London A: Mathematical, Physical and Engineering Sciences*, *364*(1845), 2231-2265.

Wiegel, R.L., Noda, E.K., Kuba, E.M., Gee, D.M. and Tornberg, G.F. (1970). Water waves generated by landslides in reservoirs. *Journal of the Waterways, Harbors and Coastal Engineering Division*, *96*(2), 307-333.

Yeh, H., Liu, P., Briggs, M. and Synolakis, C. (1994). Propagation and amplification of tsunamis at coastal boundaries. *Nature*, *372*(6504), 353-355.

Zitti, G., Ancey, C., Postacchini, M. and Brocchini, M. (2015). Impulse waves generated by snow avalanches falling into lakes. In *Proceedings of 36th IAHR World Congress, The Hague, Netherlands, 2015* (No. EPFL-CONF-215899). IAHR.

Zweifel, A., Hager, W.H. and Minor, H.E. (2006). Plane impulse waves in reservoirs. *Journal of Journal of Geophysical Research: Oceans*, *132*(5), 358-368.

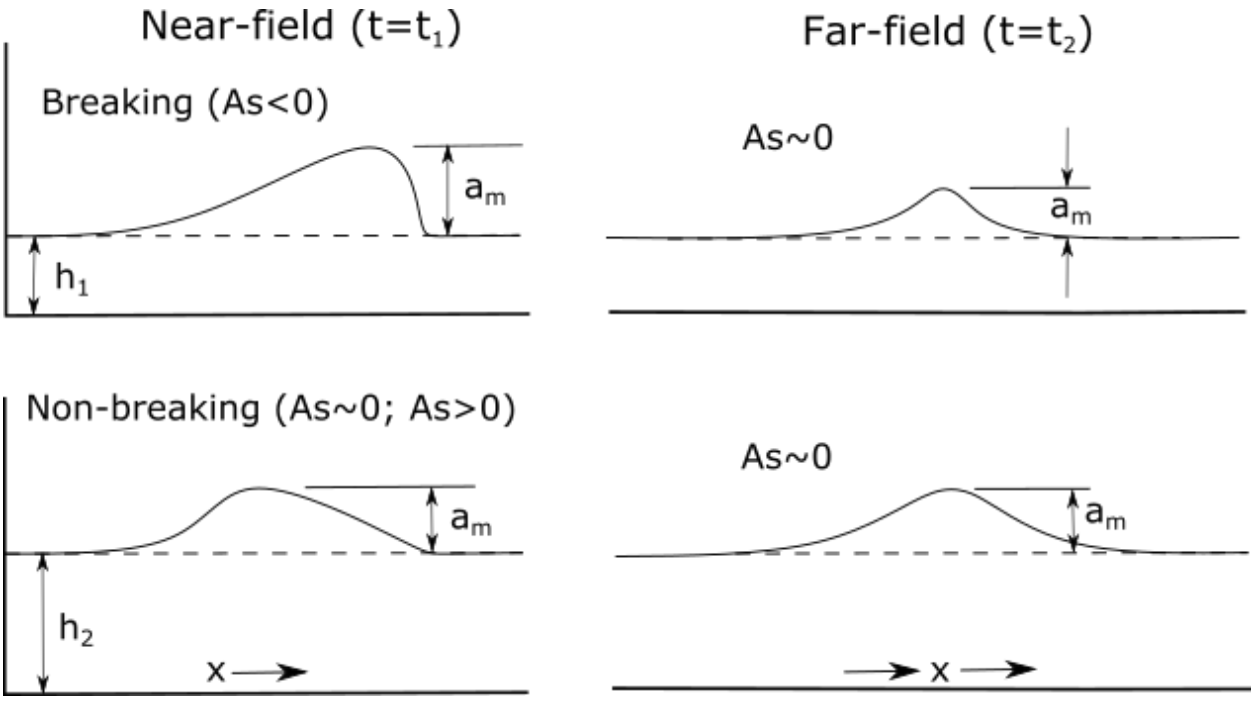

Figure 3.1: Comparison between breaking and non-breaking waves as they propagate from the near-field to the far-field. Breaking waves with *As* < 0 can experience a drastic decrease in amplitude (a_m) and non-breaking waves with As ≈ 0 or *As* > 0 experience very little amplitude change in water of constant depth (*h*).

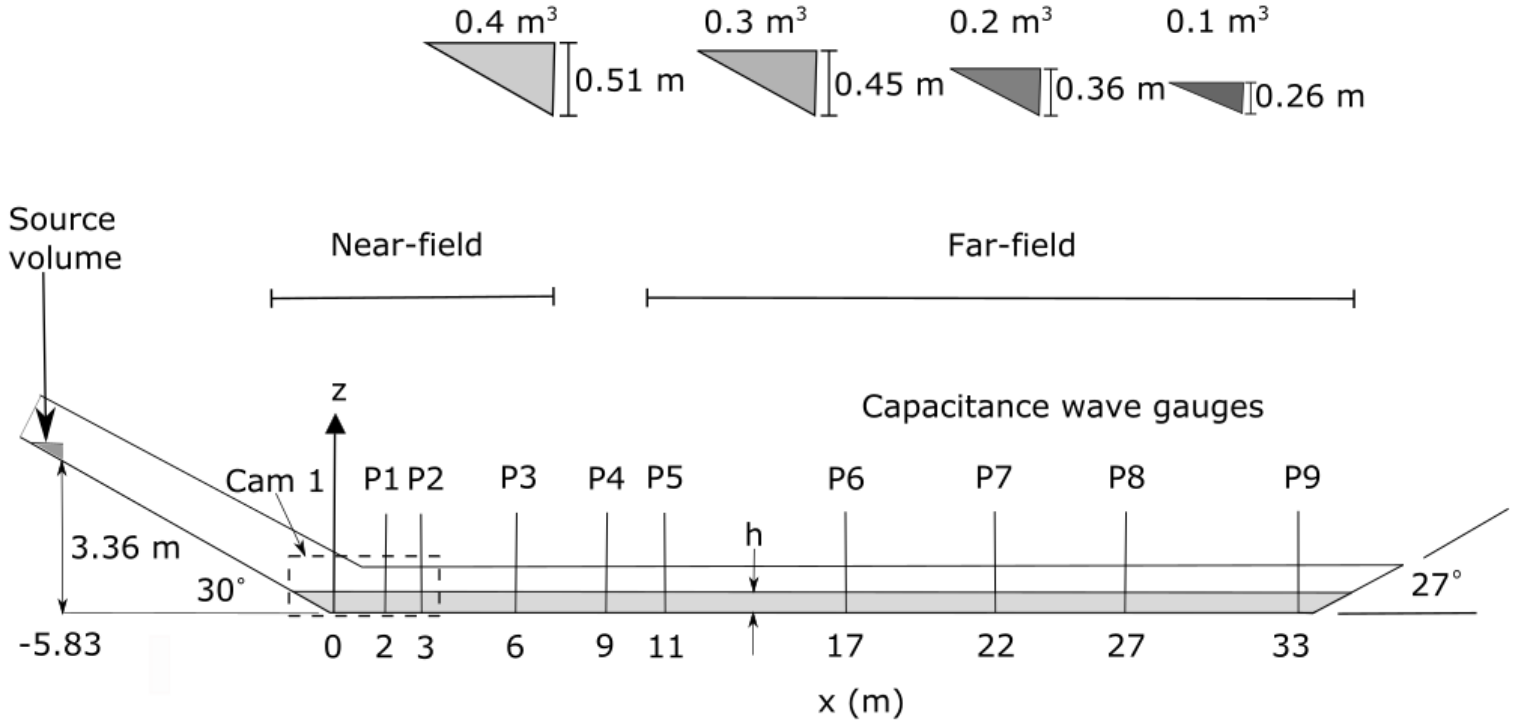

Figure 3.2: Experimental apparatus for measuring landslide generated waves. The shape of each source volume is indicated above the flume, and the 9 capacitance wave gauges along the flume from x = 2 m to x = 33 m are labelled P1-P9. The dashed box indicates the camera field of view.

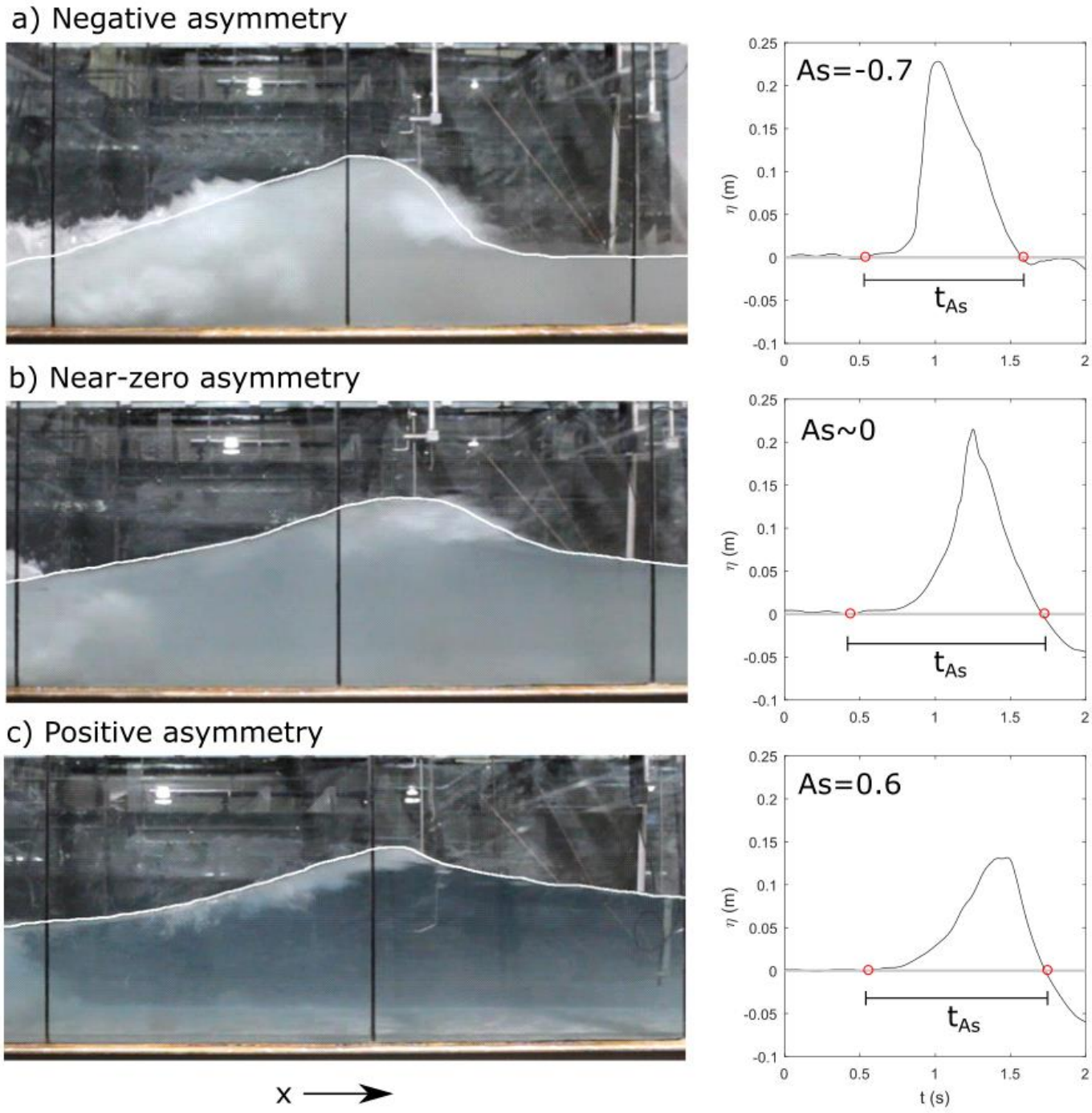

Figure 3.3: Examples of water surface elevation time series at x = 2 m (P1) accompanied by corresponding near-field camera images. The depth h and the source volume V for each case is: a) h = 0.2 m, V = 0.2 m^3; b) h = 0.35 m V = 0.2 m^3; c) h = 0.4 m, V = 0.1 m^3. The asymmetry is calculated over t_{As}, the time defined between zero-crossing points of the leading wave. For comparison, the time has been adjusted such that t = 0 at impact.

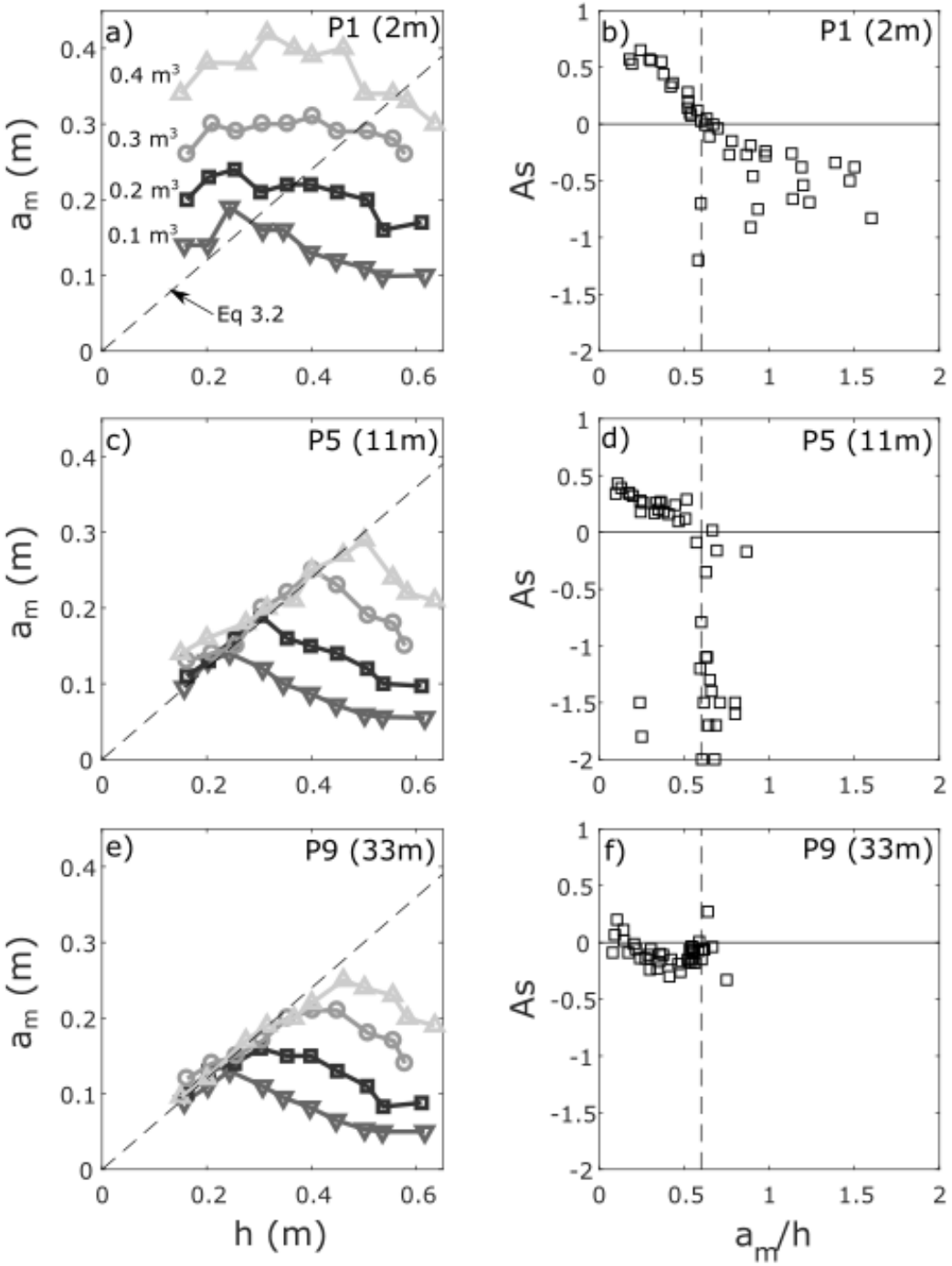

Figure 3.4: Evolution of wave properties from near-field to far-field: a) Maximum amplitude measured at P1 (*x* = 2m) for each source volume and depth; b) Asymmetry quantified from the wave shape at P1; c) Maximum amplitude measured at P5 (*x* = 11 m) for each source volume and depth; d) Asymmetry quantified at P5 from the measured wave shape; e) Maximum amplitude measured at P9 (*x* = 33m) for each source volume and depth; f) Asymmetry quantified from the wave shape at P9. Solid line indicates a perfect symmetrical wave and the dashed line is Eq 3.2.

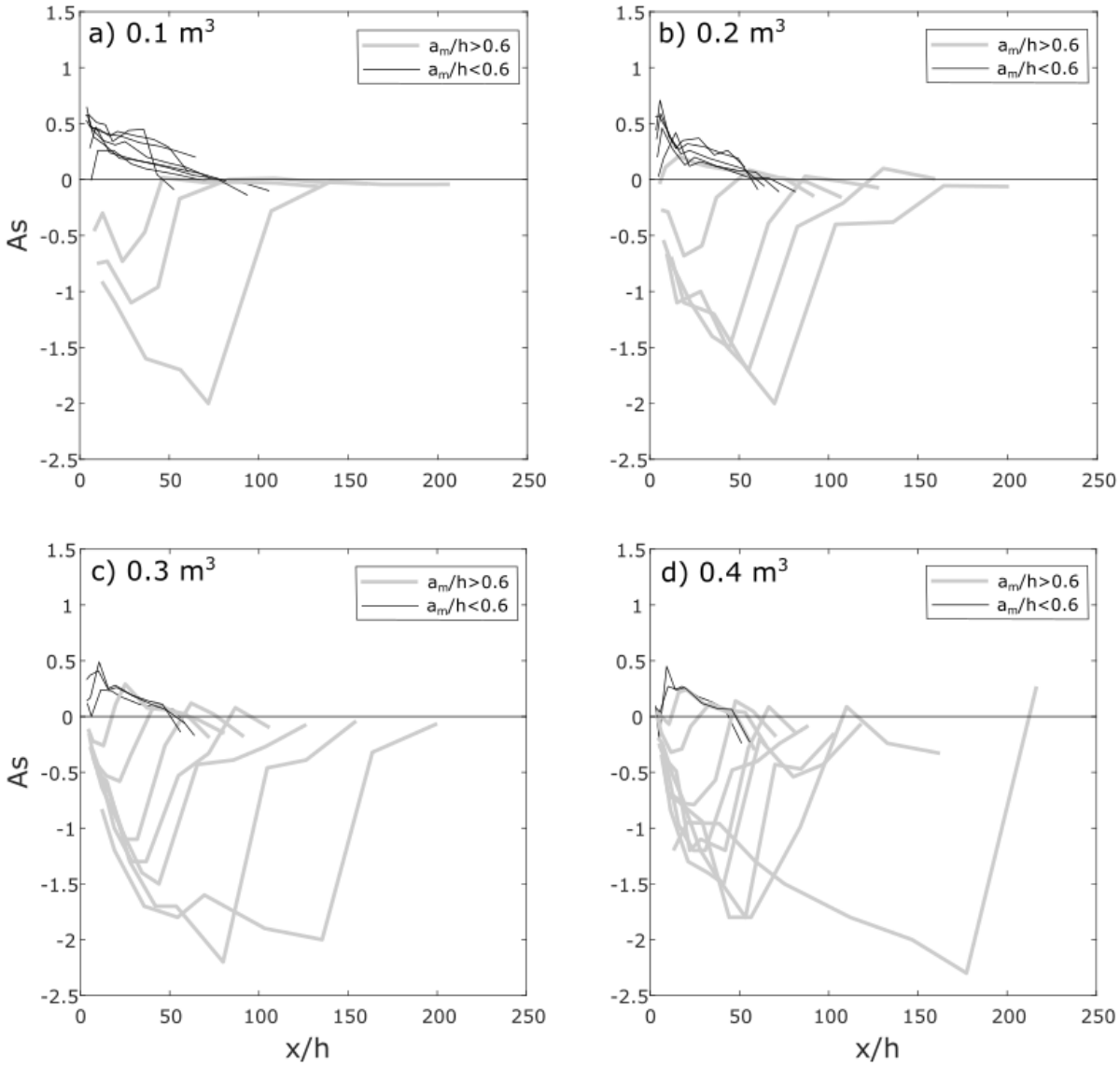

Figure 3.5: Measured wave asymmetry with relative distance for each source volume. Eq 3.2 is used to differentiate between waves that evolve differently in shape.

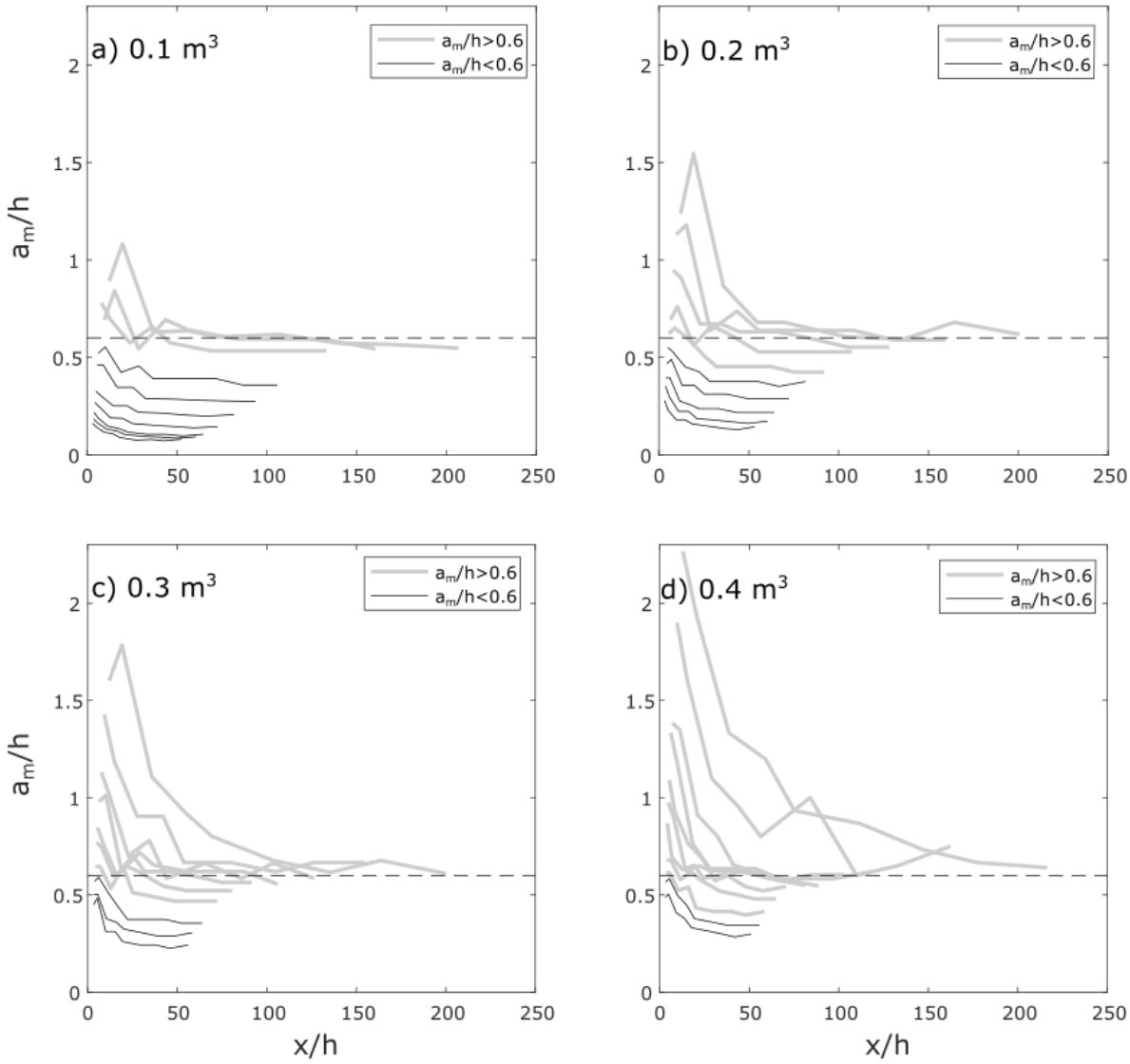

Figure 3.6: Evolution of the relative maximum wave amplitudes with relative distance for each source volume. Eq 3.2 is used to differentiate between waves that evolve differently in size.

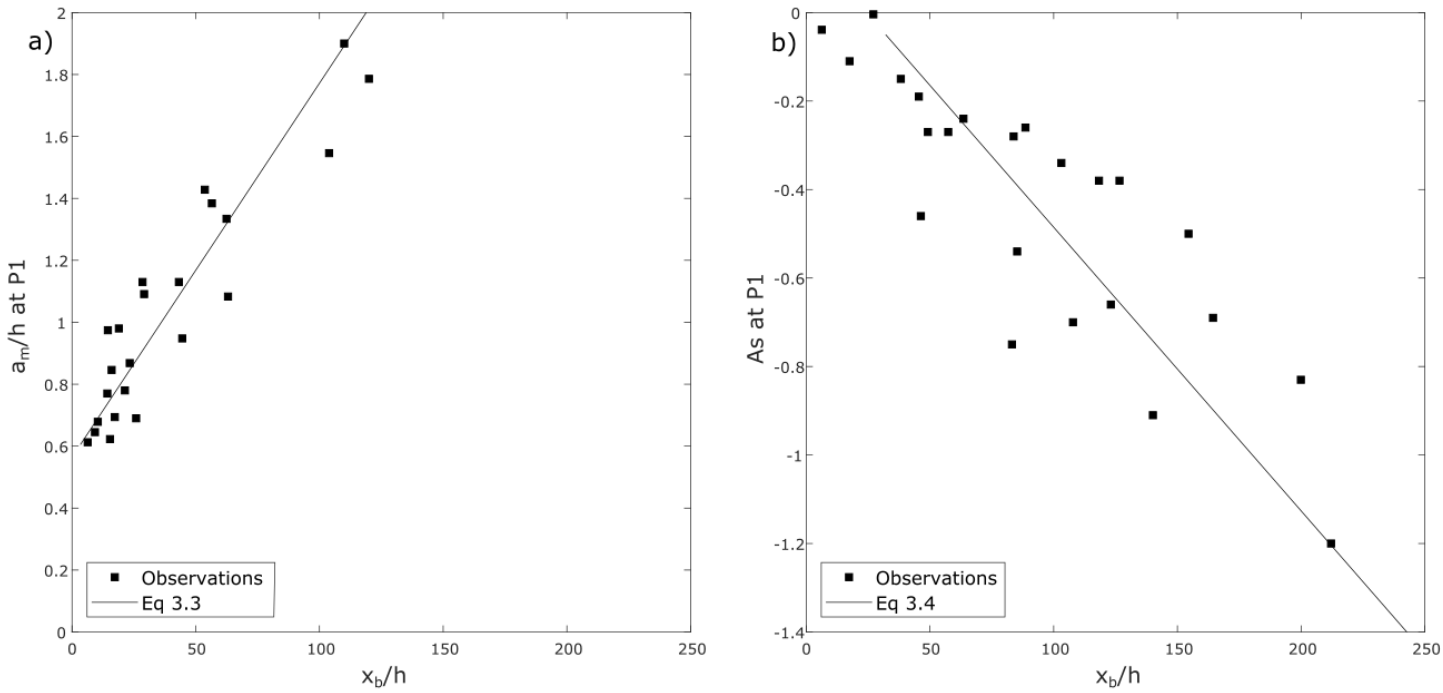

Figure 3.7: Dimensionless length scale of wave evolution x_b/h quantified for a) dimensionless wave amplitude $a_m/h = 0.6 \pm 0.05$ and b) wave shape asymmetry $As = 0 \pm 0.1$ for all source volumes.

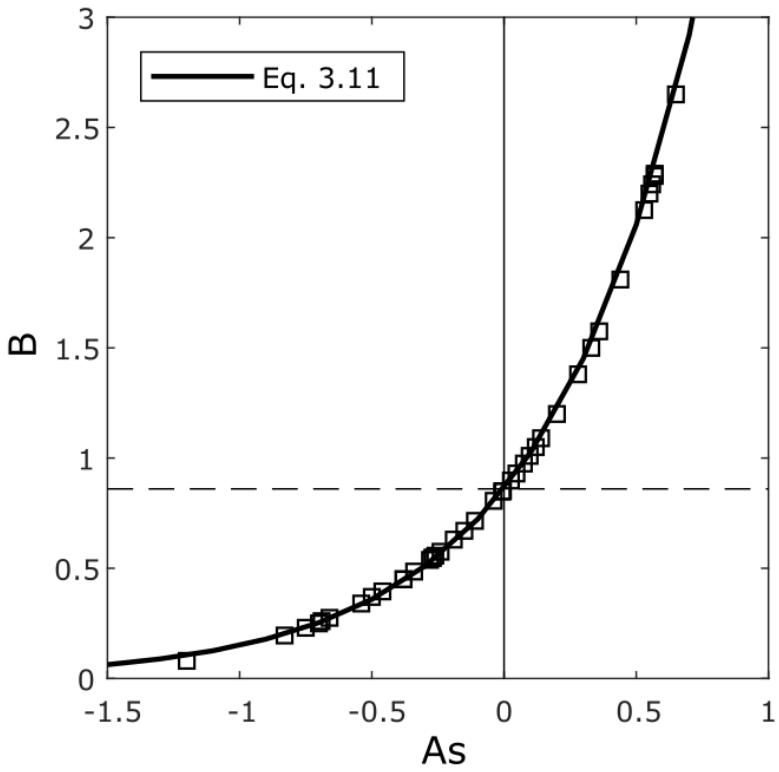

Figure 3.8: Relationship between the asymmetry and the horizontal scale coefficient *B*. Data points indicate the asymmetry calculated from wave probe observations at P1 (*x* = 2 m). The thick black line is given by Eq 3.10 and the dashed horizontal line at *B* = 0.86indicates a perfectly symmetrical wave.

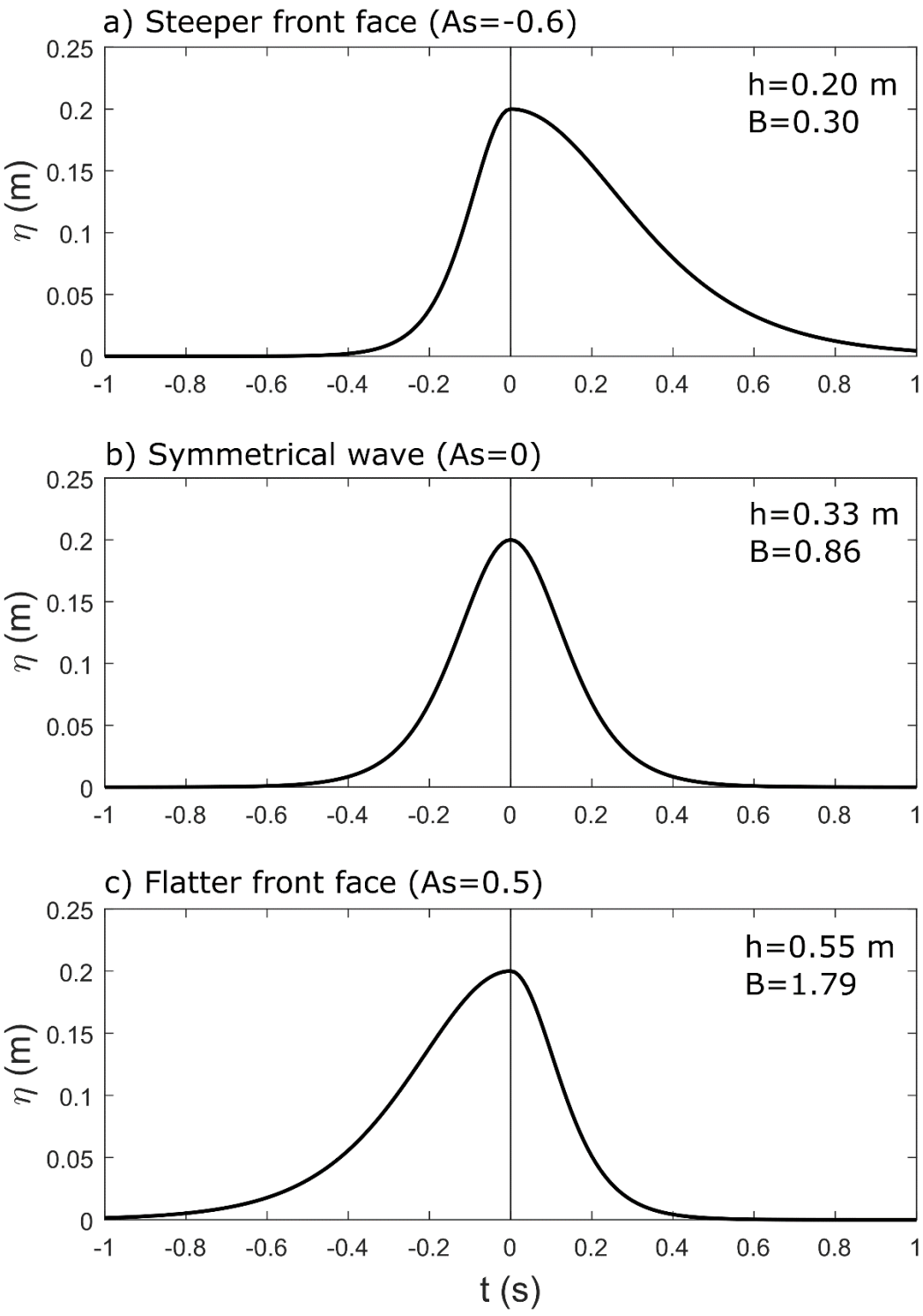

Figure 3.9: Water surface time series generated using Eq. 3.9 for 3 cases with the same amplitude (a_m = 0.20 m), to illustrate the differences in asymmetry (wave shape) for different *B* coefficients in different water depths. The time series has been adjusted such that *t* = 0 at the peak water surface elevation.

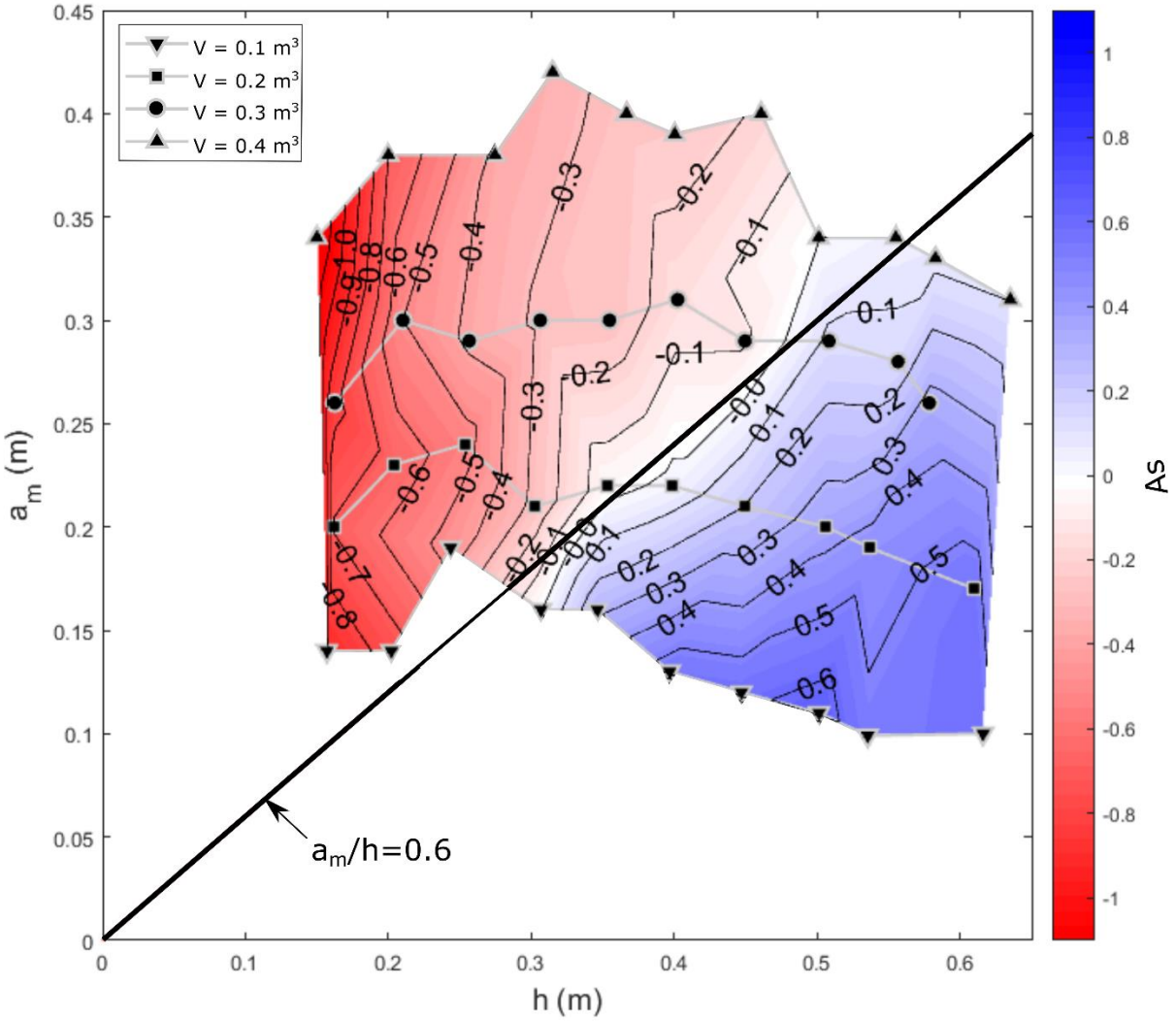

Figure 3.10: Maximum amplitude for each tests at P1 (*x* = 2 m) in black scatter points with colour contours indicating the asymmetry of the water surface elevation profile. Eq 3.2 is shown in black.

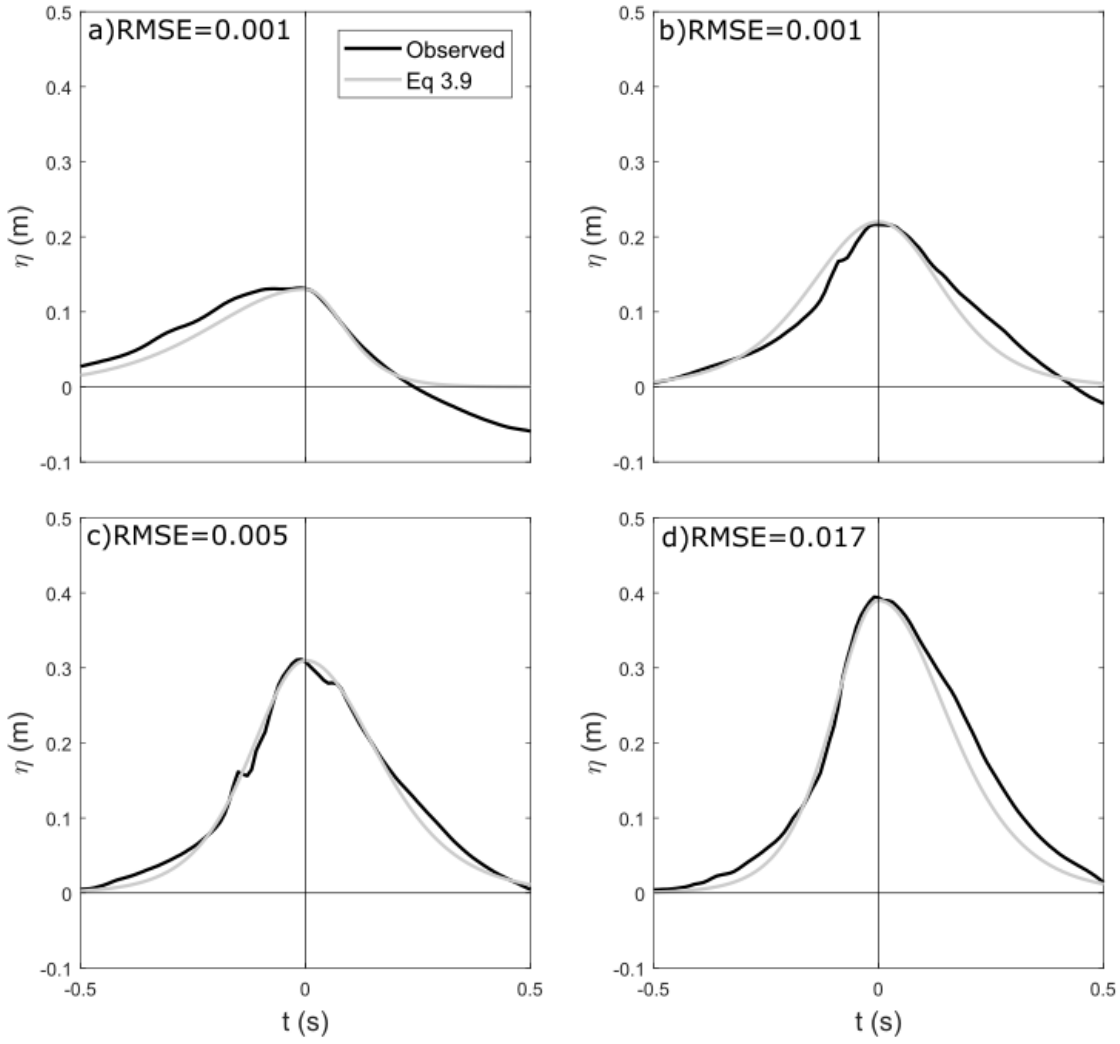

Figure 3.11: Mathematically generated cases (light grey) calculated using Eq 3.9 using the input parameters of a_m, h and As. Observations at P1 (x = 2 m) are shown in black with the correlation coefficient (R) given over the time -0.5 < t < 0.5. All plots shown tests with different landslide volume for the same water depth (h = 0.4 m) and the As values are a) 0.51; b) 0.05; c) -0.15; and d) -0.23 for volumes from 0.1-0.4 m^3 respectively. The time series has been adjusted such that t = 0 at the peak of both the simulated and observed data.

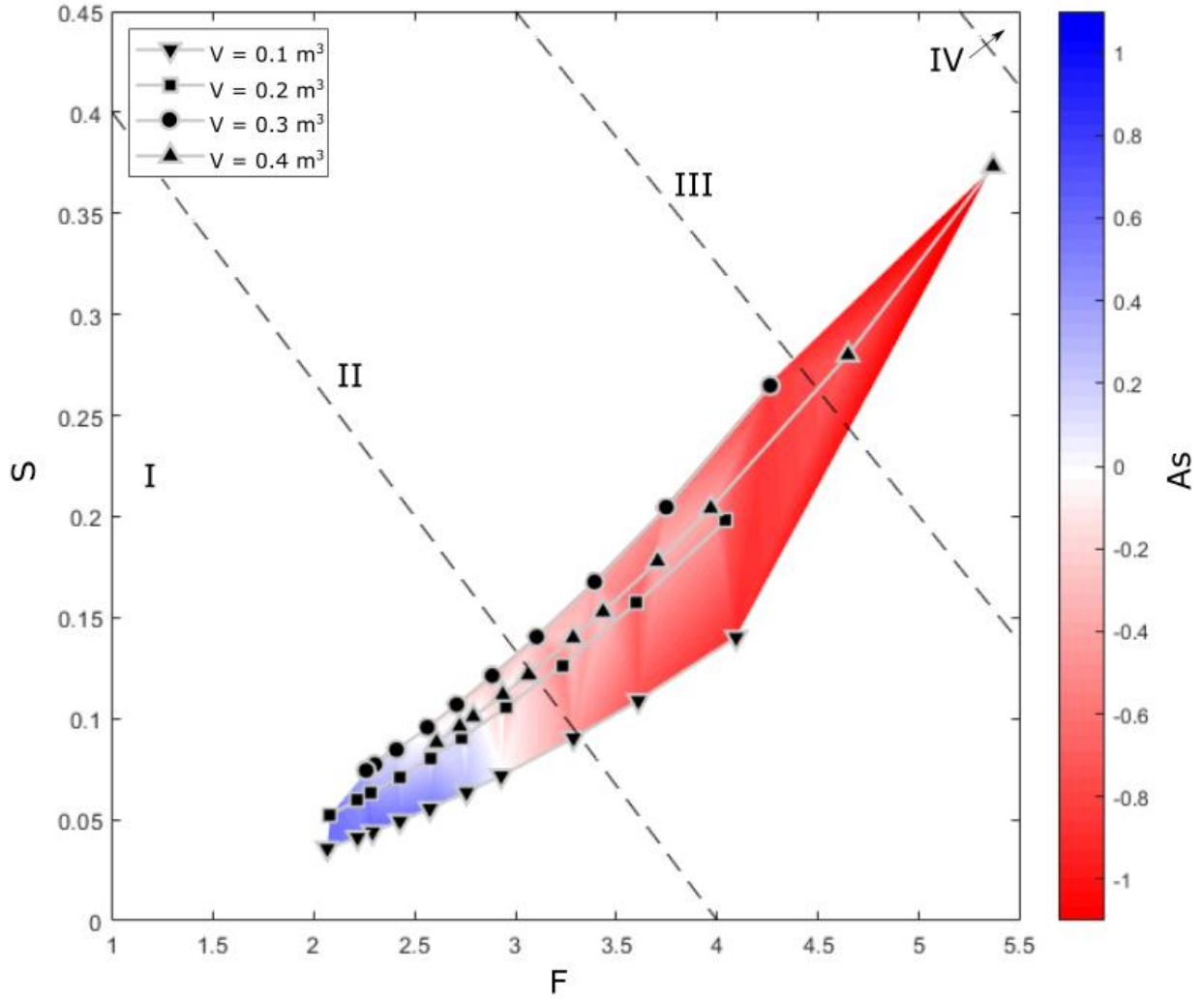

Figure 3.12: Map of wave shape quantified by asymmetry at P1 (colour contours) for dimensionless landslide parameters of relative slide thickness *S* and Froude number *F* for each source volume. The dashed lines indicate the wave type classification described by Fritz et al. (2004), for I: non-linear oscillatory waves; II: non-linear transition waves; III: solitary waves; and IV: transient bores.

Chapter 4

Influences of time and length scales on waves generated by dry granular landslides

4.1 Introduction

Management of landslide tsunami risk requires an accurate prediction of the near-field amplitude of a wave generated by a given landslide source volume/mobility scenario. The amplitude is needed as the initial boundary condition input into wave propagation models for calculation of the magnitude and distribution of run-up along the shoreline. Recent analytical work considering the transfer of momentum from the slide to the first wave has highlighted the significant role the time and length scales of forcing play in determining the initial amplitude of the first and largest wave (e.g. Mulligan and Take, 2017; Zitti et al. 2015). In particular, Mulligan and Take (2017) hypothesize that the consideration of momentum transfer can be simplified through the assumption that the time and length scale of forcing can be related to each other as a function of the initial horizontal component of the slide velocity. However, the time and length scale of forcing have not been typically reported for past studies on the generation of impulse waves from dry granular flows, leaving additional experimental data required to validate this simplifying assumption.

In the first of such required studies, the influence of these parameters has been examined experimentally in Chapter 2, which used a novel strategy of using water as the impacting flow material to achieve an upper bound of possible flow mobility. These experiments indicated that the time and length scale of forcing were related as assumed by Mulligan and Take (2017); however, at a higher average velocity through the momentum transfer zone than assumed by the authors for dry granular flows.

This parametric study of experimental results has also yielded interesting new conclusions arising from the ability to track the longevity of the high amplitude, a_m, of the first wave along the 33.5 m length of the

flume. Recent research on impulse waves generated by highly mobile flows completed in Chapter 2 has discovered that if the near-field amplitude, a_m, normalized by the still water depth h, (a_m/h) > 0.6, the wave amplitude drops rapidly with distance x during the process of wave breaking (Figure 4.1a). In contrast, a wave with an a_m/h < 0.6 in the near-field, as shown in Figure 4.1b, retains a much higher fraction of its amplitude in the far field. This is of note, as H_b/h = 0.78 has been considered the solitary breaking criterion, where H_b is the breaking wave height (Grilli et al., 1997). Furthermore, the experimental database of tsunamis generated by highly mobile flows has led Chapter 3 to investigate relationships between amplitude and wave shape, which was quantified using asymmetry. Asymmetry is defined as the skewness of the water surface about the vertical axis, computed using the Hilbert transform of the time series (Elgar and Guza, 1985), and three examples are shown in Figure 4.1c. The time series of pitched forward waves correspond to a pitched backward saw-tooth shape in space. This results in a wave that is highly skewed and therefore has a high value of *As*. Negatively asymmetrical waves are pitched forward in space due to breaking and symmetrical waves have the same steepness front and back. The results from the 41 impulse waves generated by highly mobile slides conducted in Chapter 3 determined that the value of *As* = 0 also accurately distinguishes the change in behaviour from a breaking to a non-breaking wave. Therefore, as the breaking waves approach a_m/h = 0.6 in the far-field, the wave shape also becomes closer to a perfectly solitary wave with *As* = 0. These findings provide a framework in which not only the wave amplitude but the wave shape can be used as input into wave propagation models to more accurately predict the far-field characteristics of impulse generated waves; however, verification of the applicability of these results to tsunamis generated by more conventional dry granular flows is required.

The objectives of this paper are two-fold. The first objective is to revisit the momentum transfer of dry granular flows to validate whether the assumption that the time and length scales of forcing can be related in the simple assumption of Mulligan and Take (2017). The second objective is to determine whether or not the revised wave breaking criterion of a_m/h = 0.6 and the quantification of asymmetry observed in

highly mobile flows applies equally to waves generated from dry granular flows. These objectives will be achieved by conducting an experimental parametric study in which different masses (476, 980, 1960 kg) of 3 mm diameter pseudo-spherical particles will be released down a 30° incline. These landslides of varying thickness, s, and velocity, v_s, transfer momentum as the slide impacts reservoirs of varying still water depth (0.1 m < h < 0.85m) and generate tsunamis that are observed using a system of digital cameras and wave probes.

4.2 Methodology

4.2.1 Physical Model and Material

The Queen's University landslide flume was designed to release material under gravitational acceleration to create long and thin landslides. The landslide flume has a 33.8 m long base, which connects to a 6.73 m long 30° slope at one end and a 2.7 m long 27° run-up ramp at the other. The height of the sidewalls are width are consistently 1.21 m and 2.1 m respectively, further details of the flume specifications are described in Chapter 2. An aluminum box at the top of the slope is where the three source volumes of 0.34, 0.7 and 1.4 m^3 of ceramic beads is held prior to release. The beads have a dry bulk density of 1400 kgm^{-3} and a nominal diameter of 3 mm, other parameters of the beads are described in detail by Coombs et al. (2018). The maximum capacity of this box is 1.68 m^3 and the varying sizes of the source volumes are shown in Figure 4.2. The maximum clearance of the door is 0.78 m and therefore the largest volume has a slight back slope to include the material. In order to reduce the variability in the source volume, the material from the deposit was excavated and loaded directly into the box for the next tests without adding or removing any material. When the release box is triggered from ground level, the gate swings open about a hinge at the top at a tip angular velocity of 1 ms^{-1}.

4.2.2 Sensors

The thickness was measured from a side view, rotated at 30° to make the horizontal images plane with the slope and is labelled as "Cam 1" in Figure 4.2. The velocity is measured using a static mesh in geoPIV

with images from an overhead view labelled at “Cam 2” on Figure 4.2, which is tilted upwards at 30° such that the line of sight of the camera is perpendicular to the slope. The landslide parameters of velocity and thickness of the two smaller source volumes were measured using a Proscilica GX1050 camera with a Nikon Nikkor 24 mm f/2.8D lens at 100 Hz with a spatial and temporal resolution of 1024x1024 pixels. The largest source volume uses a Sony DSC-RX10M2 equipped with a SONY Vario-Sonnar T* Carl Zeiss 2.8/8.8-73.3 lens at 480 Hz. Both Cam 1 and Cam 2 are illuminated using a high-seed flicker free Pallite VIII light source. The immediate wave generation zone was captured with the use of a Canon Rebel T5i, labelled as “Cam 3”, recording at 29 Hz with a resolution of 1929x1101 pixels, which was placed 3.2 m from the outside of the flume. After the test was completed and the reservoir was drained, the same camera was used to capture the deposit shape using images taken approximately 2 m above the base and normal to the flume for photogrammetry analysis. The water surface elevation (η) with time was measured using nine 0.6 m long wave probes along the entire length of the flume in the centreline. The stations for the wave probes (P1-P9) are located at x = 1.9, 3.1, 6.0, 8.8, 11.3, 16.8, 22.0, 26.6 and 32.5 m from the origin at the base of the landslide slope measuring at a frequency of 100 Hz. The observations from the nine wave probes have been used to quantify both near-field and far-field wave shape and amplitude.

4.3 Results

4.3.1 Landslide

The objective of these tests is to generate a wide range of initial a_m/h to investigate the range of propagation characteristics. The effects of how the thickness and velocity change with time for each source volume can be seen in Figure 4.3. As expected, the velocity is relatively constant with changes in volume due to the marginal increases in the initial position of the centroid for this fixed point apparatus. The initial velocity corresponds to the peak velocity and as the flow continues, the velocity decreases. The peak velocities at initial stages in time vary from 5.0-5.8 ms^{-1}, increasing slightly with each increase in source volume. The thickness changes more dramatically with both time and volume. The smallest

volume experiences the smallest change in thickness over the entire period of the flow and the opposite is true for the largest volume. The peak thickness occurs around 1 s into the flow for all three source volumes. The size of the front of the landslide is very comparable for each source volume, ranging from 0.037 m-0.041 m. The entire length of the landslides were not recorded due to the limited recording time of the cameras; however the initial changes in landslide characteristics are the most critical and the properties of the landslide at the end of the flow are insignificant to the wave properties, which are the focus of this study.

A summary of the landslide parameters averaged over the first 1 s of flow are shown in Figure 4.4. This highlights the minimal change in the landslide velocity and the constantly increasing flow thickness with each increase in source volume. Therefore, the primary effect of changing the volume is changing the thickness, as it changes considerably with volume. A time of 1 s was used to average the landslide parameters for each source volume in order to include the dramatic changes in s.

4.3.2 Momentum Transfer

The typical process of momentum transfer generating waves in the near-field is shown in Figure 4.5. In this example, 1.4 m^3 of material enters the 0.45 m deep reservoir at the left hand side of the images. The time displayed is based on t = 0 s upon first impact into the water and the dashed white line represents the still water level and the surface of the impulse wave is highlighted in solid white. The first two wave probes are located at x = 2 m and x = 3 m from the intersection of the slope and the horizontal base of the flume and can be used as scale. In Figure 4.5a the initial stages of wave generation is shown indicating a very bulbous front forming in the submerged landslide. In Figure 4.5b, the speed of the wave exceeds the speed of the submerged portion of the landslide, which is defined as the time of wave release Δt_e. At this point in time, the horizontal length of the submerged landslide is defined as the effective length L_e and can be measured from the intersection of the still water level and the entry slope (shown in red). Figure 4.5c&d show that the distance between the wave and the submerged landslide continues to elongate until the submerged landslide finally reaches a velocity of zero and its maximum length L_m.

4.3.3 Near-field Wave Characteristics

The near-field maximum wave amplitude of each source volume is compared with varying *h* in Figure 4.6a. As expected from theory, larger source volumes with larger *s*, create bigger waves. Each source volume reaches a peak at a critical depth and begins to decrease as *h* increases. This is a similar trend seen for the singular volume of a similar gravitationally accelerated granular material used by Miller et al. (2017). It is interesting to note that the peak maximum near-field amplitude increases with each source volume as does the depth at which this maximum occurs.

The effective time and length scales at the point of wave detachment are shown in Figure 4.6 b&c. In general, landslides into shallower water tend to experience a smaller forcing length and release the wave sooner than deeper depths; however both of these relationships are non-linear with changes in *h*. The effective length L_e is a fraction of the total runout length of the slide L_m since the wave is released sooner than the submerged landslide comes to a halt (Figure 4.6c&d). Both L_e and L_m increase with increased volume and L_m also increases linearly with *h*.

The profile of the deposit for each source volume into a reservoir depth of 0.3 m, shown as the thin black line, can be seen in Figure 4.7 with the side view of the flume angle shown as the thick black line. This also demonstrates the increase in L_m with each increase in source volume. The centre of mass of each deposit volume, labelled as '+', remain relatively constant with changes in source volume due to the increase in material remaining on the slope. The position of the deposit centre of mass was used to calculate the travel angle α_g, which represents the angle of the line drawn through the centre of mass of source volume and debris. Due to the limited variability in location of the centre of mass in both the debris and source volume, the travel angle varies slightly from 29.0°-29.8°. Therefore, it can be assumed that each source volume experiences the same amount of friction as they travel down the slope of the flume and the increase in L_m is related to an increase in volume as well as water depth.

4.3.4 Wave Shape

In this paper, wave shape is quantified using time varying η at one point (P1-P9) and can be checked visually with spatial data captured at a moment in time (Cam 3). Typical data for three types of wave shapes is shown in Figure 4.8 with the wave traces recorded from Cam 3. The first two probe locations are indicated in black with the calculated asymmetry from the respective time series indicated as As_{P1} and As_{P2}. The wave traces with a peak amplitude at the location of the probes (x = 1.9 and x = 3.1 m) are in bold to visually compare the spatial and temporal wave shape. When h = 0.2 m, the leading wave has a long tail at both P1 and P2, which results in a highly negative asymmetry. When h = 0.45 m, the waves looks symmetrical at P1 and this has a good correlation with a very low As calculated from the time series. The deeper water case with h = 0.85 m indicates a long front with a steeper tail, which is characteristic of a positively asymmetrical wave.

The wave shape can be estimated two separate ways in the near-field: The first is to use the relative landslide parameters of thickness S and Froude number F (Figure 4.9). The wave shape of impulse waves generated by high and low mobility landslides at x = 1.9 m can be compared for the relative landslide parameters. The colour bar indicates As = 0 as white with extremely negative and positive values of As as red and blue respectively. In general, the same trends are seen with both data sets. Small relative thicknesses and low relative velocities produce positively asymmetrical non-breaking waves and the opposite is true for negatively asymmetric breaking waves. The dashed line indicates when As = 0 for various S and F for both datasets comprised of 19 dry granular and 41 highly mobile slides.

The second method to estimate wave shape in the near-field is the color map comparing the near-field amplitude with changes in depth (Figure 4.10). Unlike the previous method, it is only valid for the current dataset and cannot be scaled. The contours of As demonstrate how As = 0 moves in terms of a_m/h as the wave propagates from P1-P3 (shown as Figure 4.10a-c). The previous study conducted in Chapter 3 demonstrated that As = 0 and a_m/h = 0.6 could both be used to define breaking and non-breaking impulse waves generated by highly mobile flows. Figure 4.10 indicates that the asymmetry is rapidly changing in

the near-field and does not always coincide with $a_m/h = 0.6$. The discrepancies in the near-field at P1 with wave shape are due to the influence of the reflected wave, which is able to reach $x = 1.9$ m close enough behind the leading wave to appear as a long tail in the time series. The reflected wave travels slower than the leading wave and therefore it is almost completely separated out by P2, where $x = 3.1$ m. This results in a good correlation between $a_m/h = 0.6$ and $As = 0$ for $x \geq 3.1$ m (Figure 4.10b&c). Therefore, the relationship shown for $As = 0$ cannot distinguish between breaking and non-breaking waves in the extreme near-field; however after breaking waves have reached a stable wave amplitude they are perfectly symmetrical waves with $As = 0$ (Figure 2.10c).

The far-field wave characteristics were obtained using the nine wave probes (P1-P9) located from 1.9 m < x < 32.5 m from the intersection of the slope and the base of the flume. The maximum amplitude of the time series at each of these probe locations can be used to analyze how the wave amplitude changes over time and space for each test (Figure 4.11). The dashed line of $a_m/h = 0.6$ indicated on each of the subplots correctly distinguishes the breaking from the non-breaking waves in the near-field. There are some data points missing for the smaller two volumes at P4 and P5 due to technical error with the wave probe calibration; however it can be seen that by $x = 16.8$ m, all of the waves with an initial $a_m/h > 0.6$ reduce to meet this wave breaking limit.

The two distinct behaviours of breaking and non-breaking waves can be seen more clearly comparing the relative maximum wave amplitude with a relative distance (Figure 4.12). The breaking waves, shown in grey, have $a_m/h > 0.6$ measured at P1 and they experience a rapid decrease in amplitude as x/h increases until $a_m/h = 0.6$. The non-breaking waves, shown in black, show very little decrease in amplitude as they propagate. The wave shape can be shown in a similar manner using the same threshold of $a_m/h = 0.6$ to divide the breaking and non-breaking waves (Figure 4.13). The breaking waves, shown in grey, evolve to be more asymmetric as they propagate before becoming a completely symmetrical wave. Non breaking waves, shown in black, change very little in shape but do gradually become closer to perfectly

symmetrical. In general, breaking waves require a longer relative distance to reach *As* = 0 than non-breaking waves. There are two examples of negatively asymmetrical waves that have an initial $a_m/h < 0.6$ that have not been identified as breaking waves (Figure 4.13a&c). These two waves are the examples described in Figure 4.10a, measured as having *As* < 0 due to the influence of the reflected wave. Based on the trends shown in Figure 4.13 wave shape evolves to gradually become closer to *As* = 0, both outliers follow the trend of a non-breaking wave. This data from the far-field indicates that the conclusions drawn from the highly mobile landslide generated impulse waves by Chapter 2 and 3 are valid for granular landslide with a higher density such as the experiments conducted herein.

4.4 Comparison of Observed Near-filed Amplitudes with Published Relationships

The maximum near-field amplitude obtained from the wave traces, normalized by *h*, is plotted in Figure 4.14a against predictions using the semi-empirical impulse product parameter framework proposed by Heller and Hager (2010), referred to hereafter as HH10. This framework provides an accurate estimate of the relative maximum amplitude in the near-field if $a_m/h < 1$, for the shallower water cases with breaking waves it does not apply. The hydrostatic momentum equation derived by Mulligan and Take (2017), referred to as MT17, which uses the assumption that

$$L = \frac{1}{2} v_s cos\alpha \Delta t_e \qquad \text{(Eq. 4.1)}$$

also provides a reasonable estimation of the normalized maximum wave amplitude for $a_m/h < 1$ (Figure 4.14b). This assumption is only valid for gravitationally accelerated granular flows. Mulligan and Take (2017) also include a fluid continuity limit which provides an upper limit for the maximum wave amplitudes in shallow water indicated by the dashed line, which holds true for all tests with one exception.

$$\frac{\eta}{h} = \frac{s v_s cos\alpha \Delta t_e}{hL} + 1 \qquad \text{(Eq. 4.2)}$$

Both HH10 and MT17 prove to be equally valid for gravitationally accelerated granular material of varying impact thicknesses for small a_m/h and the application of the fluid continuity limit with the wave-breaking limit gives a range of relative maximum near-field amplitudes occurring in shallow water. Any wave initially estimated in this range will rapidly decrease in maximum amplitude to the wave-breaking limit as it propagates.

The assumption in Eq 4.1 has shown to be valid for the experiments completed in this study; however the parameters of L_e and Δt_e have not previously been measured for granular flows. In this study, both of these parameters were measured using the images captured from Cam 3 in the near-field and are compared with the highly mobile flows from Chapter 2 in Figure 4.15. The trend-lines for each dataset indicates that L_e and Δt_e are directly proportional to one another and therefore can be described using a constant deceleration factor, as in Equation 4.1.

Although the simplifications do not perfectly match, the gradient of each of the trend-lines demonstrate that different materials decelerate at different rates after impact and therefore they produce different near-field maximum wave amplitudes. A larger length of forcing over the same amount of time displaces more volume of the reservoir to create a larger wave (Figure 4.15b). Therefore the length of forcing and effective time are two important parameters, which must be quantified in order to provide a more robust method of predicting a near-field maximum wave amplitude that can be applied to a variety of landslide types. Further research should be completed using different materials with a range in landslide mobility in order to fully quantify the effects of the time and length scales on the near-field maximum wave amplitudes. This research has provided enough evidence to prove that the quantities L_e and Δt_e must be quantified in order to accurately assess the near-field characteristics.

4.5 Conclusions

The near-field characteristics of 19 impulse waves created by three varying volumes of granular landslides were studied using a large scale experimental setup. Long and thin gravitationally accelerated

flows impact the reservoir at maximum velocity, which then constantly decreases with time. The thickness of each source volume varies significantly with time. This introduces some uncertainty with regards to the appropriate value of thickness to use in semi-empirical and momentum based predictions of near-field amplitude. The effective time until wave release is a function of the water depth and is independent of volume. Therefore, it was determined that averaging the landslide parameters over the first 1 s provides a reasonable value describing the changing thickness and velocity, which is consistent for all volumes. The profiles have been quantified by aligning overhead photos taken of the deposit after the reservoir has been drained using Photogrammetry. A profiles of each deposit shape can be compared to determine the centre of mass has very little variation with each increase in source volume. This also coincides with a minimal change in the travel angle, which varies from 29.0°-29.8°.

The wave shape of each impulse wave produced in the current study was quantified using asymmetry. This data can be combined with the tests completed in Chapter 2 to provide validation of the trends observed for highly mobile flows. In general, the same trends are seen with smaller S and F producing slightly positively asymmetrical waves and high *S* and *F* producing very asymmetric breaking waves; however the correlation between $As = 0$ and $a_m/h = 0.6$ is not valid for the near-field. The breaking wave limit of $a_m/h = 0.6$ does distinguish between breaking and non-breaking waves in the near-field and it also provides an upper limitation of the far-field maximum wave amplitudes. The breaking wave limit also distinguishes between the two distinct behaviours of wave shape: negatively asymmetrical waves become more asymmetrical before become symmetrical waves and the positive asymmetrical waves change very little in shape as they move slowly towards becoming solitary waves. These findings are consistent with the behaviours observed by the highly mobile flows creating impulse waves.

The near-field maximum wave amplitude has been compared to the predicted values from HH10 and MT17. Both provide a reasonable estimation of the impulse generated waves for granular flows; however the MT17 equation uses a simplification to describe the relationship between L_e and Δt_e, shown as

Equation 4.1. The length of forcing and effective time have been measured for the first time for granular flows and compared to highly mobile flows. As expected, the highly mobile flows travel farther in a similar amount of time, which displaces more water vertically to create a larger wave. The slope of trend-line relating L_e and Δt_e are reasonably close to the previously applied simplifications; however further research into the influence of landslide mobility on the effects of the relationship between L_e and Δt_e must be completed to fully understand how the L_e and Δt_e are influenced by mobility and the effects this has on the near-field maximum wave amplitude.

4.6 References

Coombs, S.P., Apostolov, A., Take, W.A., and Benoît, J. (2018). Observed increase in mobility of dry granular landslides, corresponding to increased collisional activity, quantified by a smart rock sensor. *Canadian Geotechnical Journal (Under review)*.

Elgar, S. and Guza, R.T. (1985). Observations of bispectra of shoaling surface gravity waves. *Journal of Fluid Mechanics*, *161*, 425-448.

Fritz, H.M., Hager, W.H. and Minor, H.E. (2004). Near field characteristics of landslide generated impulse waves. *Journal of Waterway, Port, Coastal, and Ocean Engineering*, *130*(6), 287-302.

Grilli, S. T., Svendsen, I. A., and Subramanya, R. (1997). Breaking criterion and characteristics for solitary waves on slopes. *Journal of Waterway, Port, Coastal, and Ocean Engineering*, *123*(3), 102-112.

Heller, V. and Hager, W.H. (2010). Impulse product parameter in landslide generated impulse waves. *Journal of Waterway, Port, Coastal, and Ocean Engineering*, *136*(3), 145-155.

Miller, G. S., Andy Take, W., Mulligan, R. P., and McDougall, S. (2017). Tsunamis generated by long and thin granular landslides in a large flume. *Journal of Geophysical Research: Oceans*, *122*(1), 653-668.

Mulligan, R. P., and Take, W. A. (2017). On the transfer of momentum from a granular landslide to a water wave. *Coastal Engineering*, *125*, 16-22.

Zitti, G., Ancey, C., Postacchini, M. and Brocchini, M. (2015). Impulse waves generated by snow avalanches falling into lakes. In *Proceedings of 36th IAHR World Congress, The Hague, Netherlands, 2015* (No. EPFL-CONF-215899). IAHR.

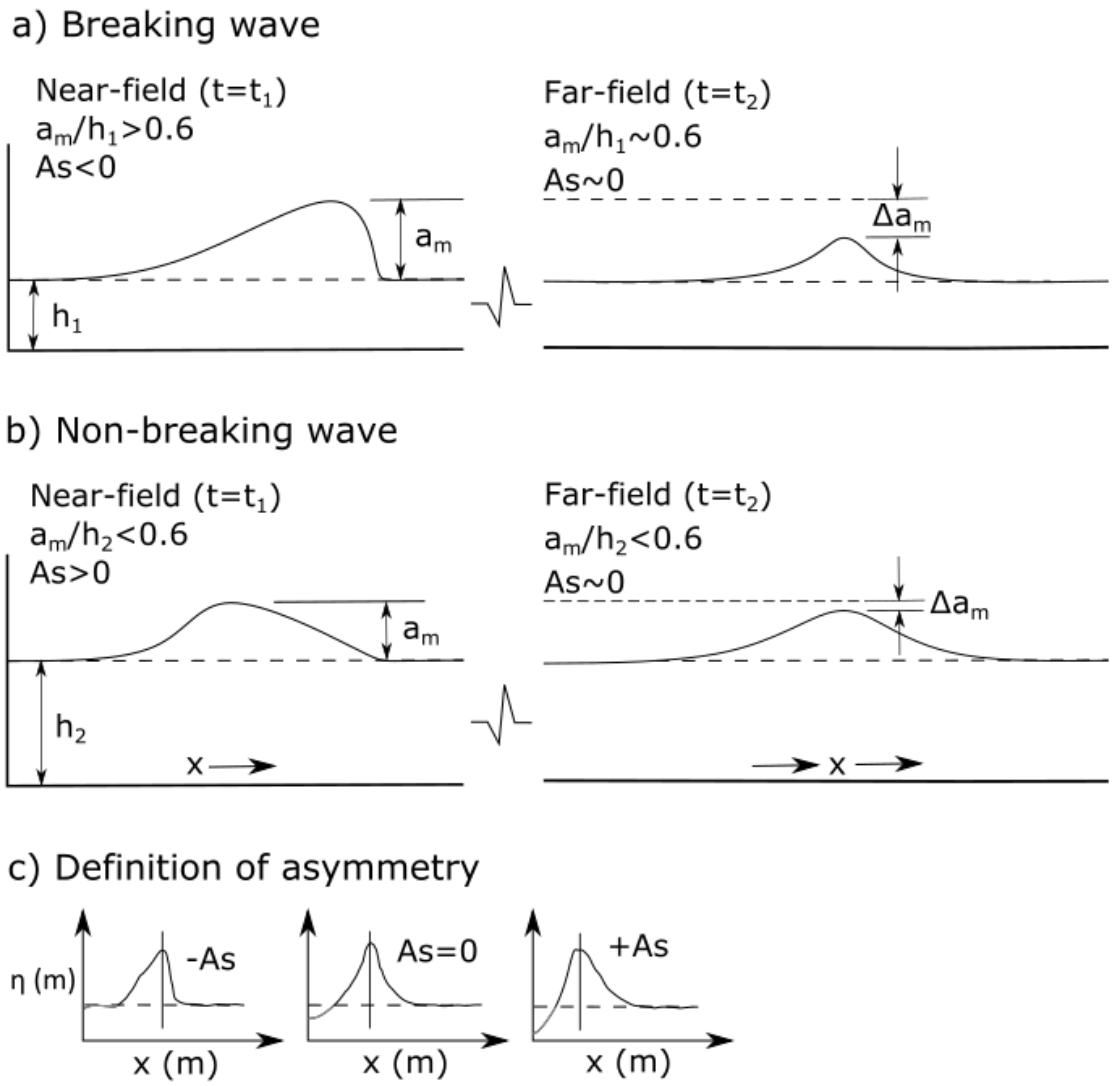

Figure 4.1: Illustration demonstrating the difference in far-field behaviour for a) breaking waves with a negative asymmetry and b) non-breaking waves with a positive asymmetry with c) the definition of asymmetry as it pertains to wave shape. The decrease in maximum amplitude a_m for a negatively asymmetrical breaking wave in shallow water is much larger than for positively asymmetrical waves in deeper water from the near-field to the far-field. The far-field behaviour for two distinctly different waves in the near-field is similar such that $As \sim 0$ and $a_m/h \sim 0.6$.

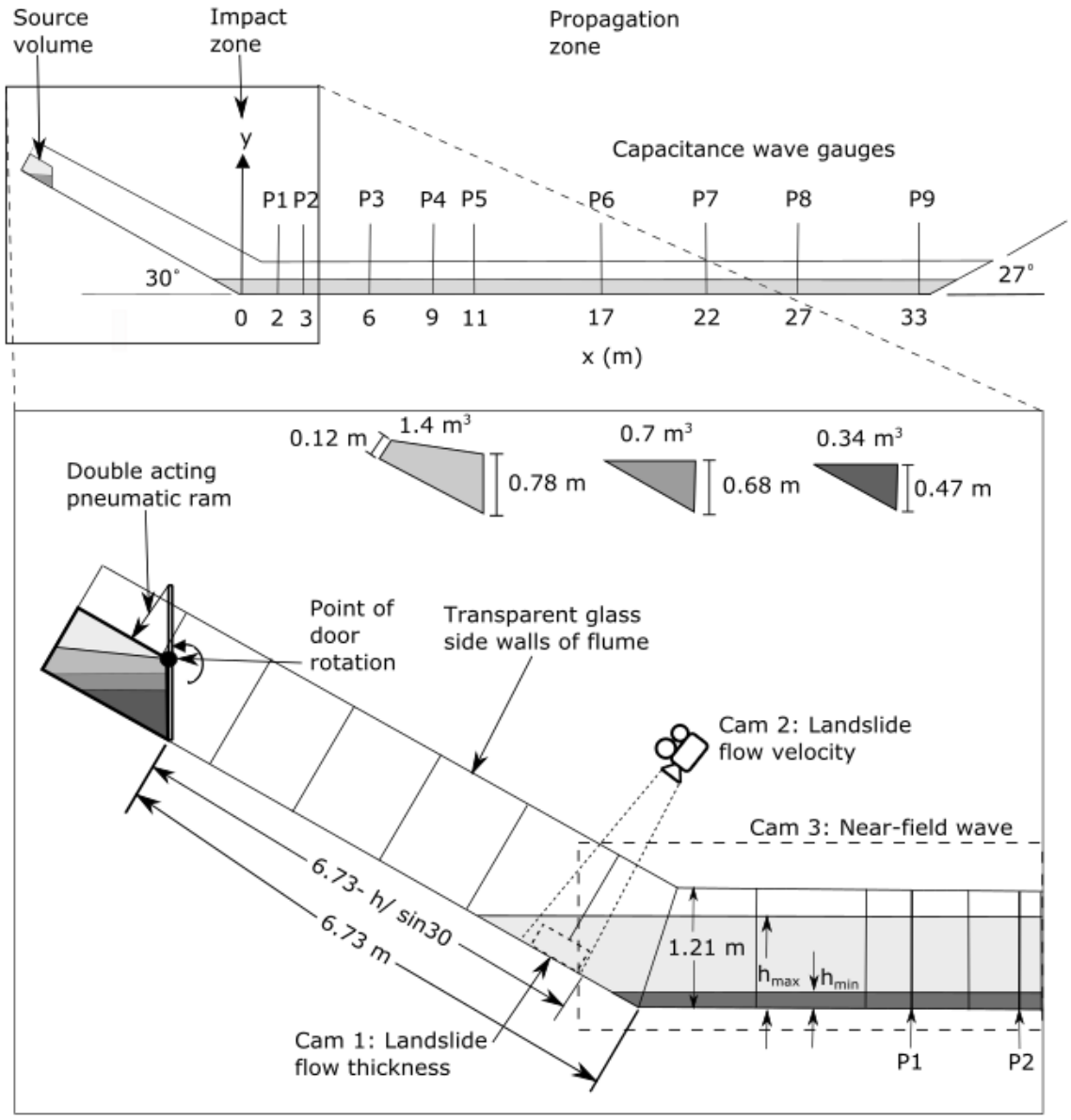

Figure 4.2: Experimental apparatus for measuring landslide generated tsunamis a) Complete length of flume showing the nine probe locations from x = 1.9 m to x = 32.5 m are labelled as P1 to P9; b) More detailed view containing the field of view of all three cameras in the near-field indicated as dashed lines and Probe 1 and Probe 2 (P1 and P2 respectively). Dimensions of all four source volumes indicated as well as the range of h, dark grey indicating h = 0.09 m and the light grey 0.85 m.

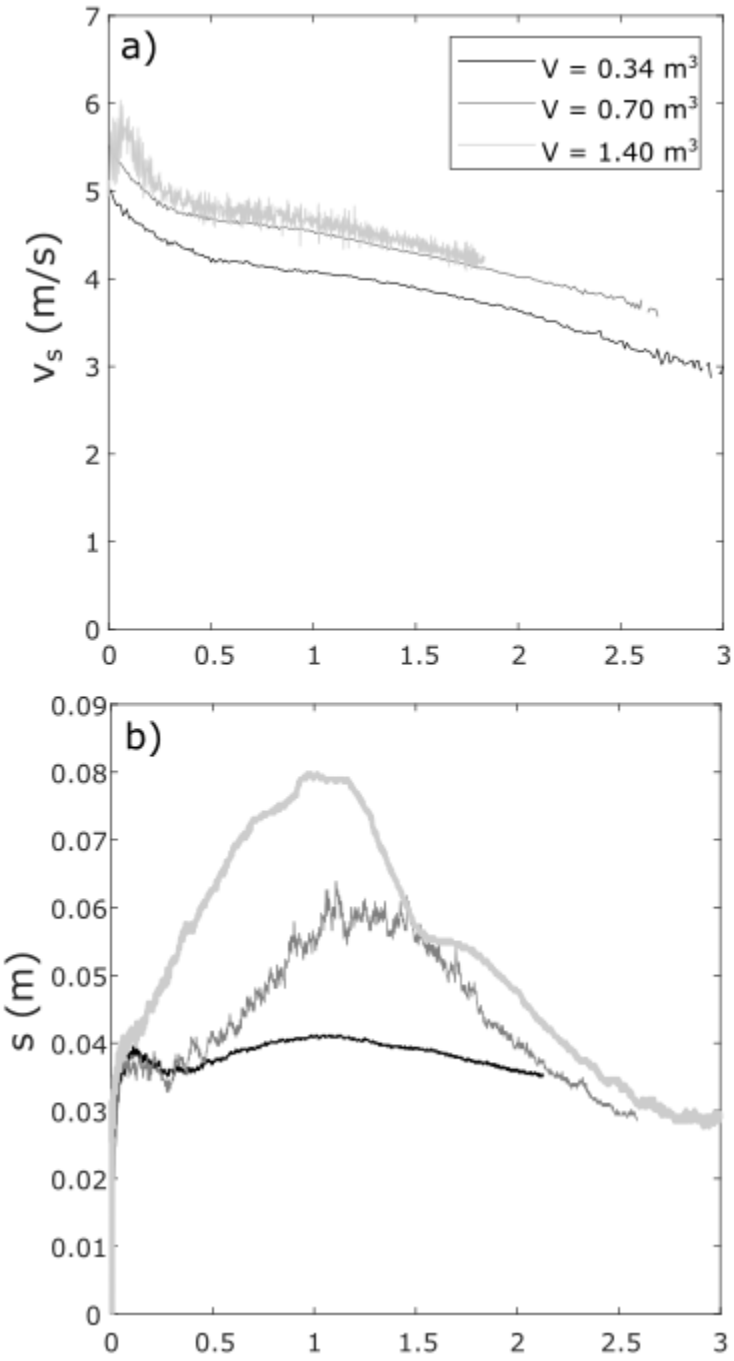

Figure 4.3: Landslide properties at impact for all three source volumes indicating a gradually decreasing velocity v_s and a highly variable thickness s for all volumes. Velocity is measured using geoPIV analysis of the images from Cam 2 and the thickness measured using the images from Cam 1.

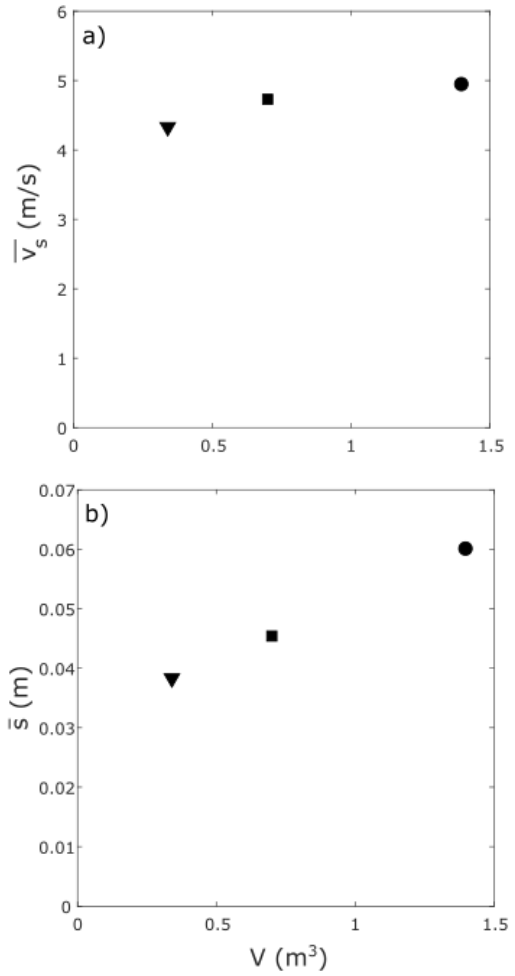

Figure 4.4: Summary of the landslide parameters averaged over the first 1.0 s of the landslide impacting the reservoir as they increase with each increase in source volume.

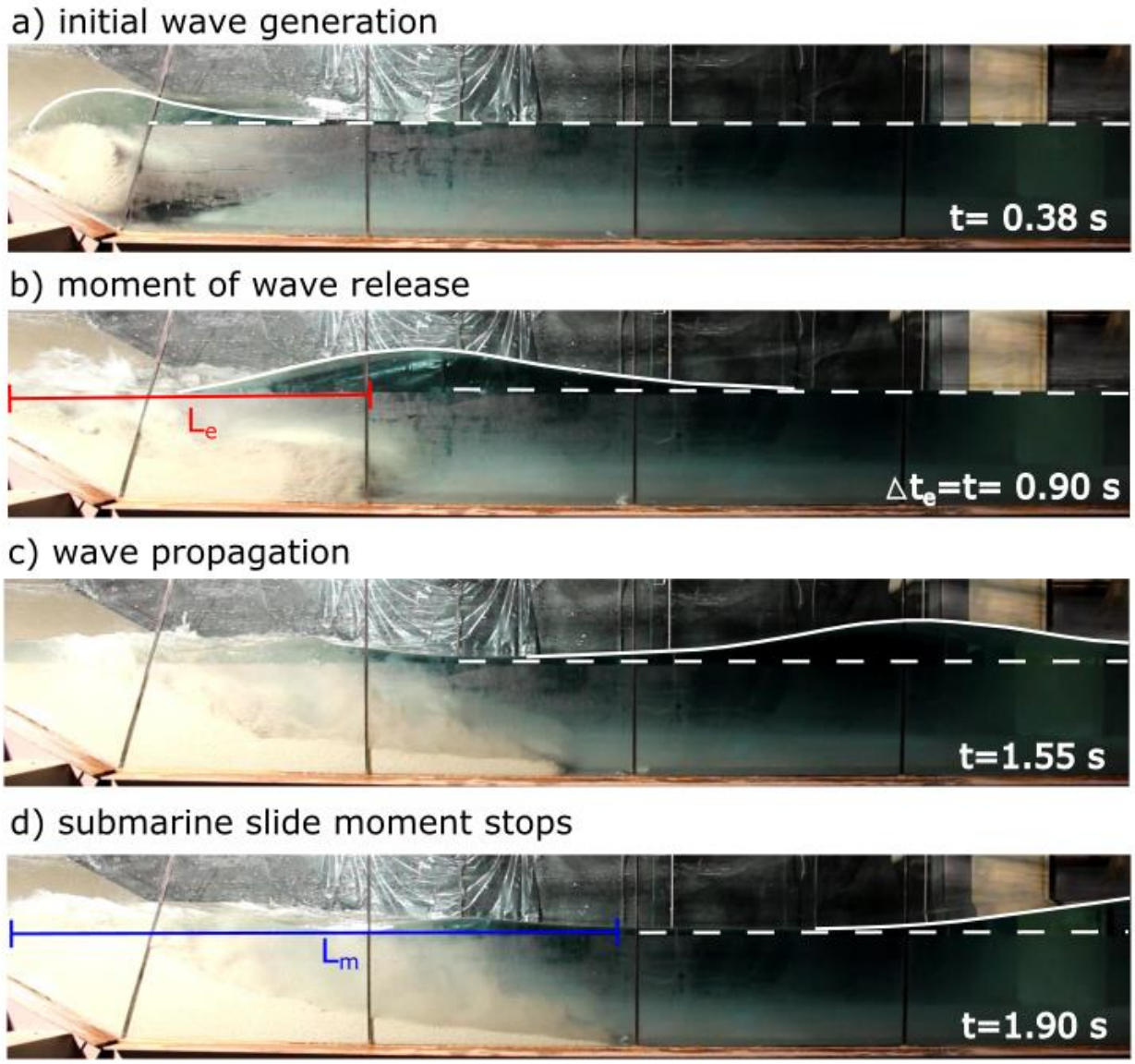

Figure 4.5: Typical test showing the wave generation process from Cam 3 for h = 0.45, V = 1.4 m^3 at different times. The initial wave is formed and continues to be pushed by the submerged mass for a distance L_e until the velocity of the wave exceeds that of the submerged plume. The submarine slide continues to move as the wave propagates further from the near-field zone until the material comes to a rest at a distance L_m.

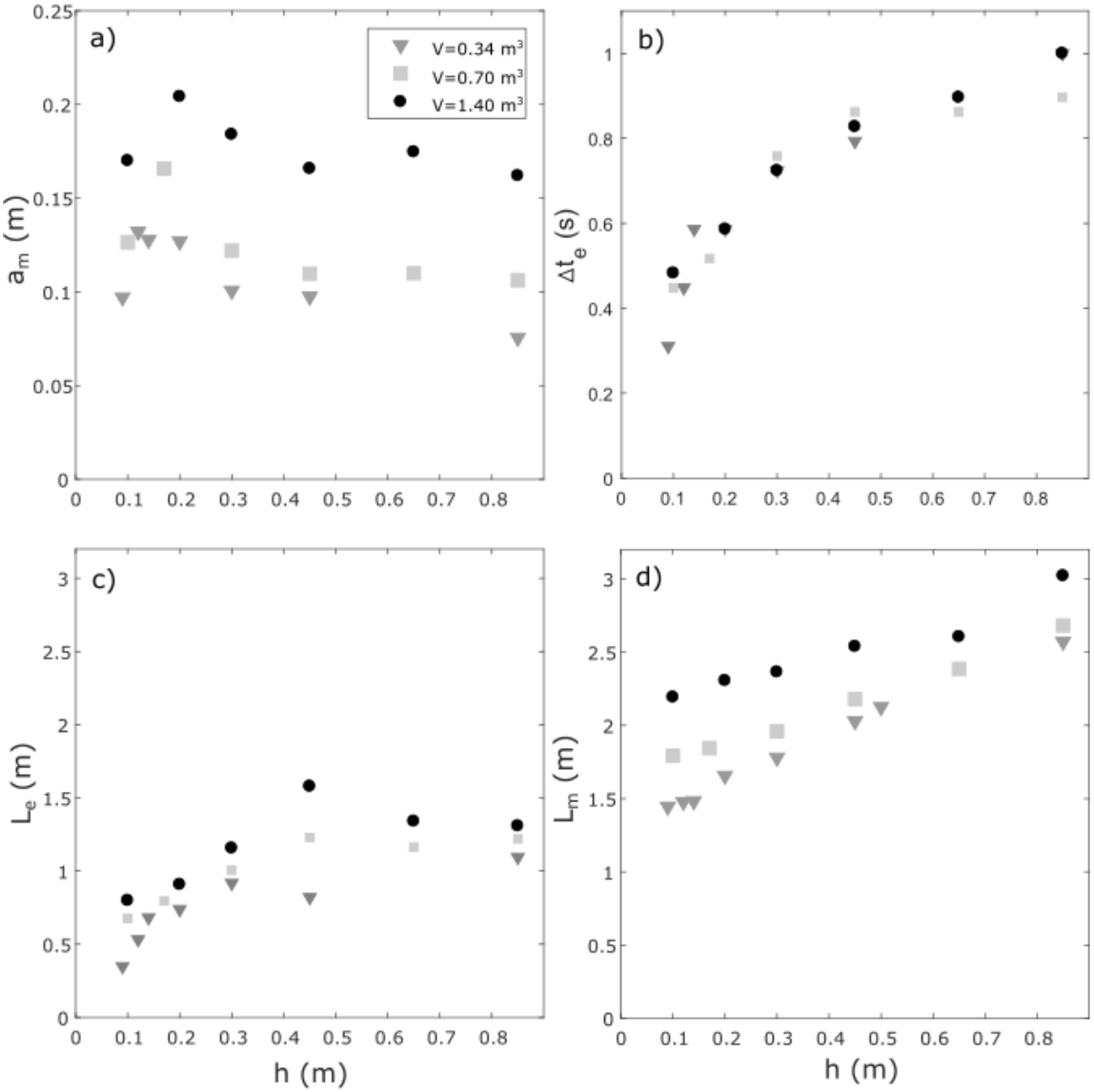

Figure 4.6: Near-field summary of characteristics for all source volumes: a) maximum amplitude obtained from the wave traces for all depths indicates a critical depth where the largest amplitude occurs and each increase in source volume increases the maximum amplitude; b) the effective time obtained from the images of Cam 3 indicating very little fluctuations with varying volumes but as the depth *h* increases, the effective time increases until it plateaus at t= 1 s; c) The length of forcing does increase with each increasing volume and it also increases with depth; d) Total runout distance increases slightly for each source volume and it also increases with depth.

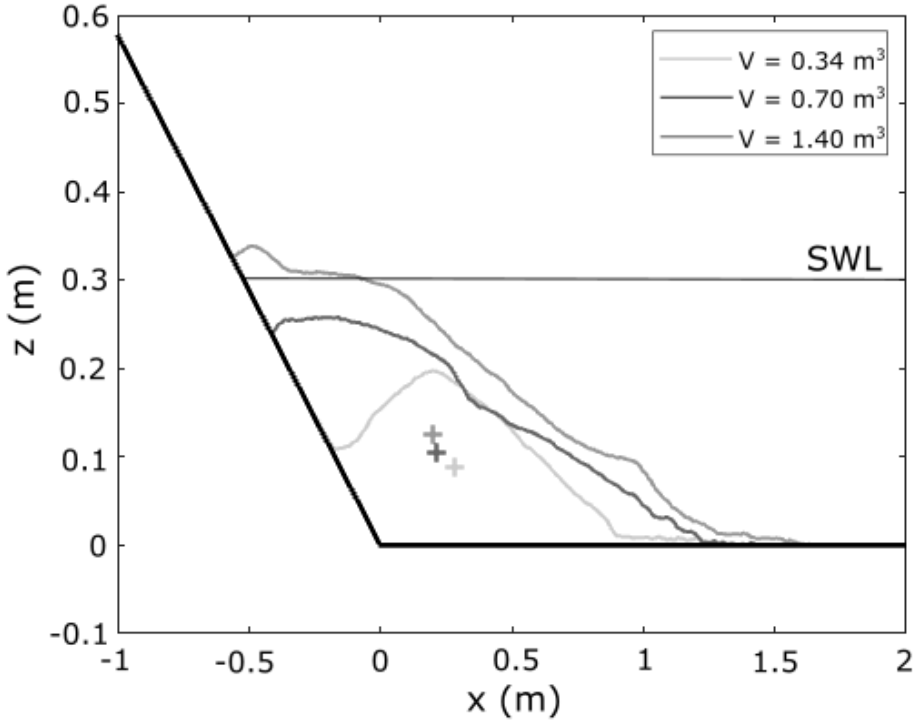

Figure 4.7: Deposit shapes for all three source volumes with *h* = 0.30 m with the centre of mass indicated by the "+" sign for each volume. The returning reflected wave may have influenced the original shape after impact.

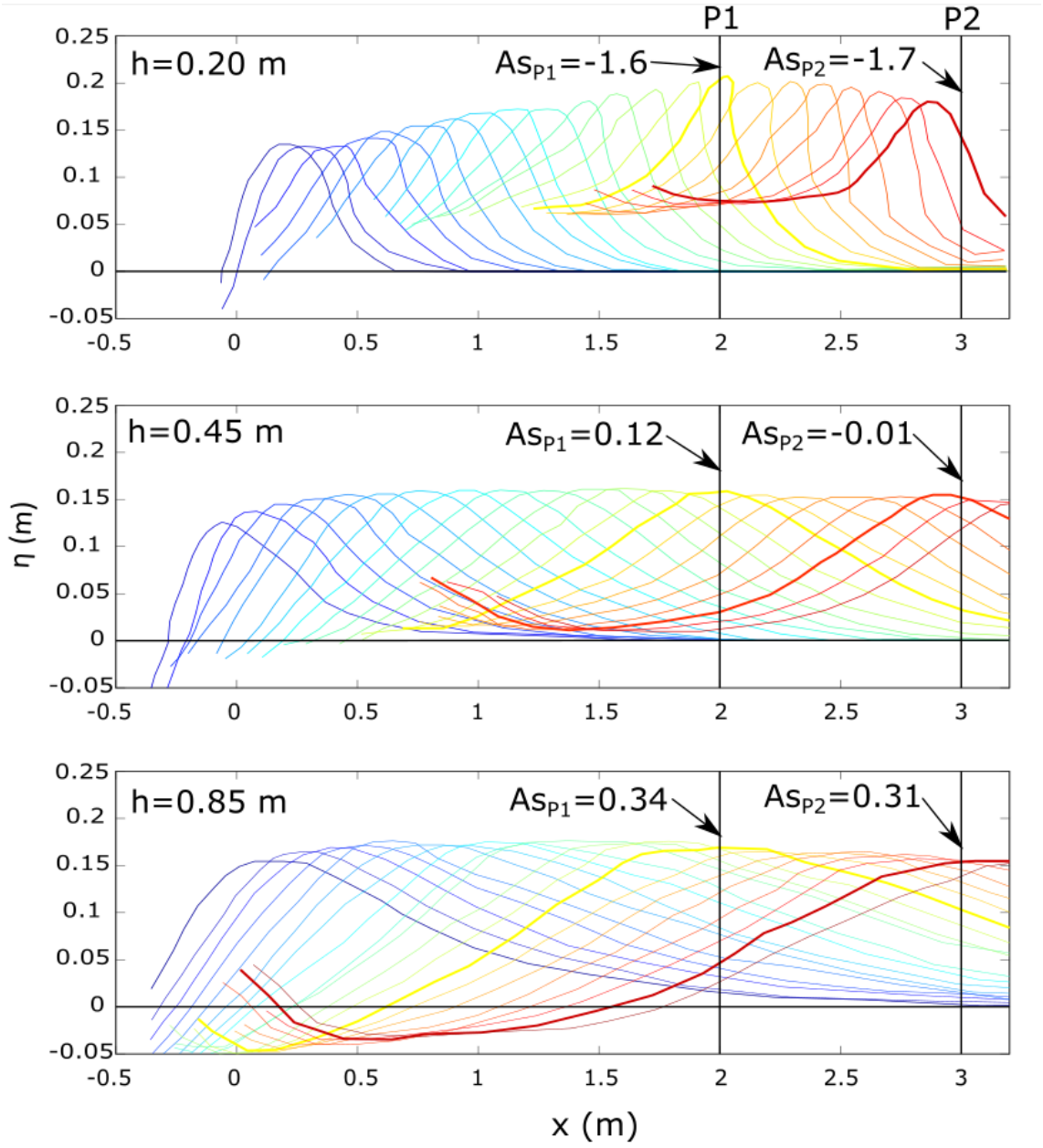

Figure 4.8: Wave traces in the near-field for three cases (h=0.2 m, h=0.45 m and h=0.65 m) with a source volume of V=1.4 m^3 and the measured wave asymmetry of those wave trace profiles shown from P1 and P2.

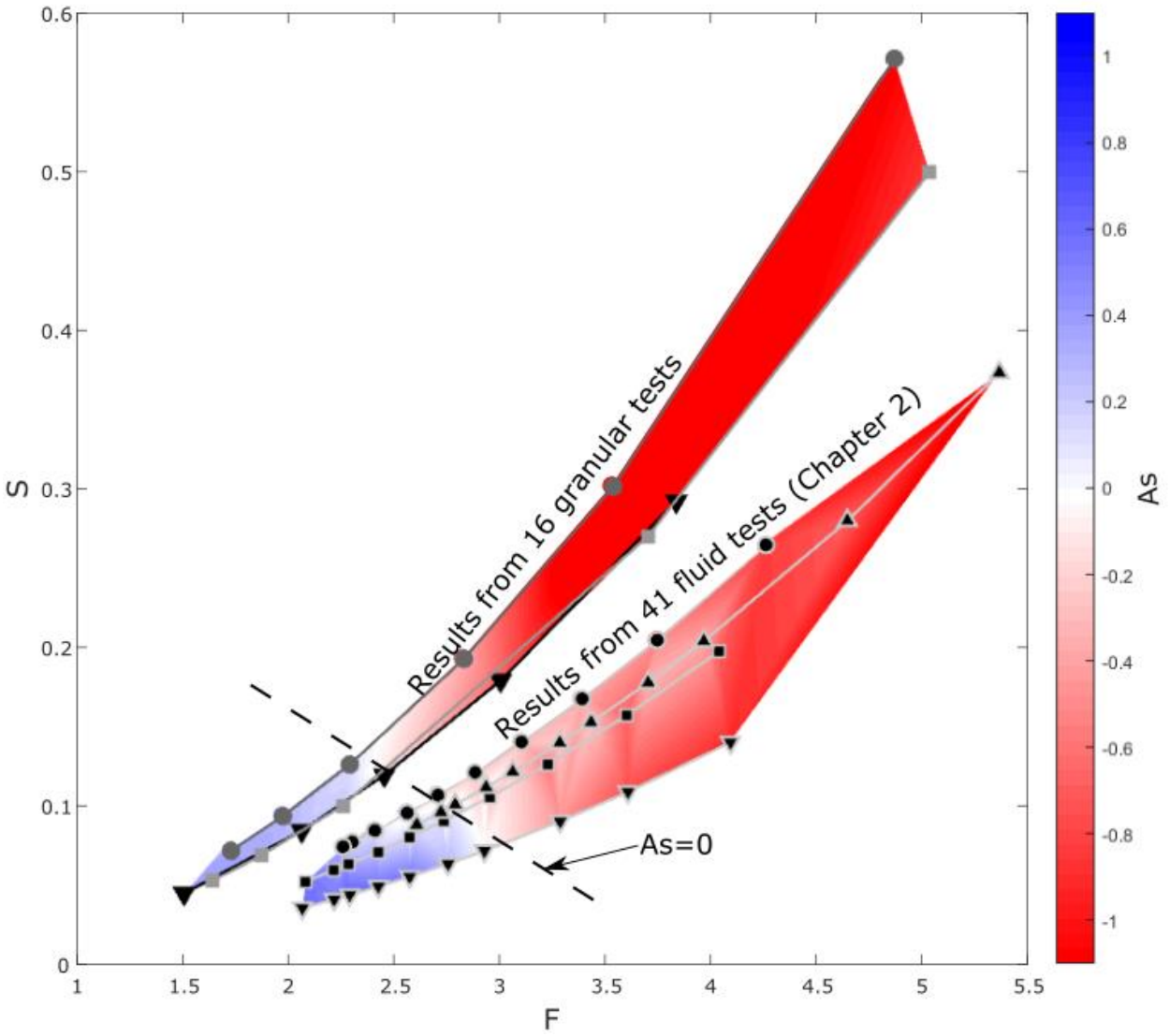

Figure 4.9: A combination of the data obtained for 41 impulse waves generated by highly mobile flows from Chapter 2 as well as 16 results from long thin granular flows indicating how the changes in landslide parameters *S* and *F* influence the wave shape in the near-field. Contours as well as the colour map indicate the measured asymmetry from P1 (x = 2 m) with a dashed line through both sets of data shows where the divide in asymmetry lies relative to the landslide parameters.

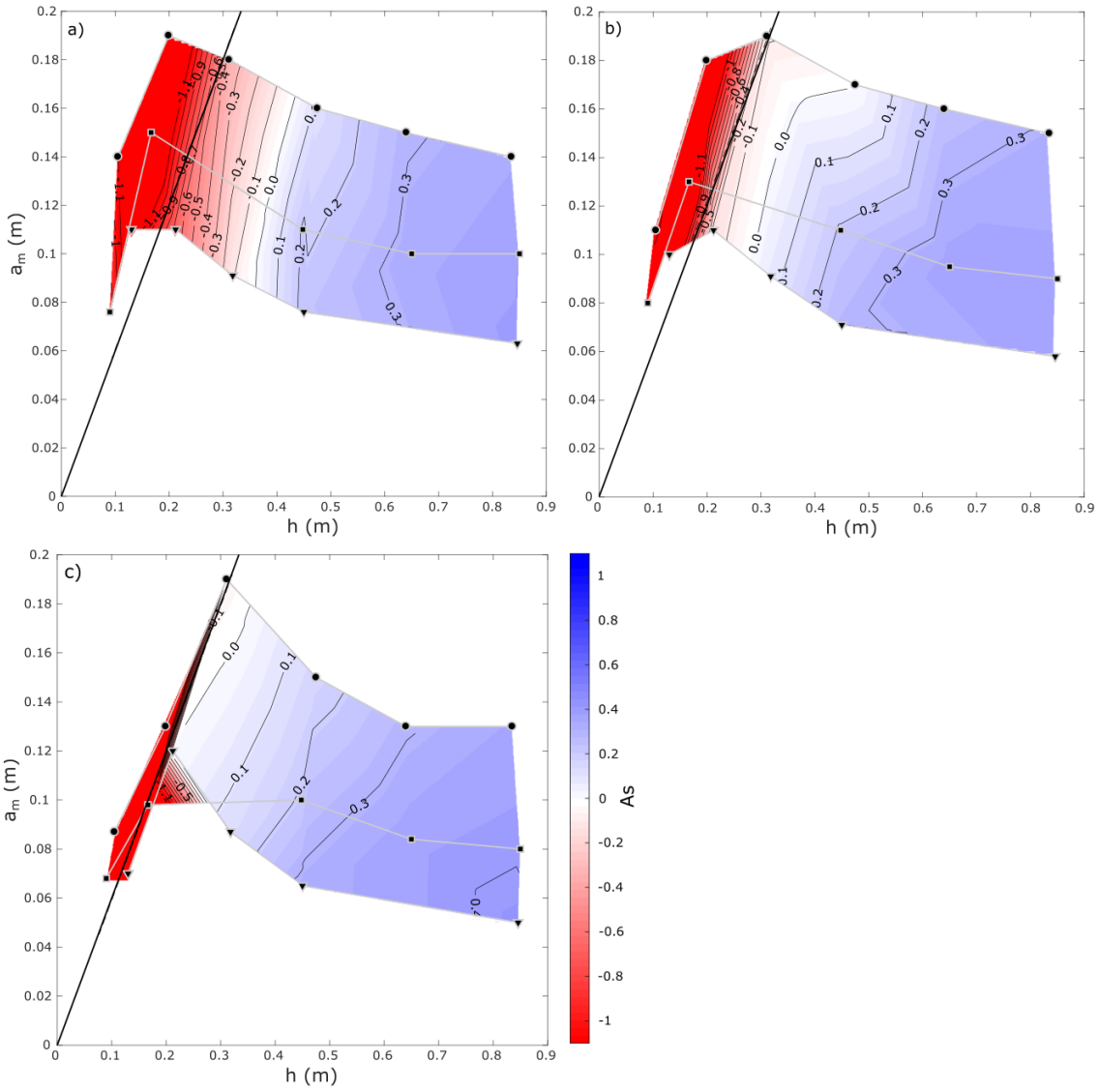

Figure 4.10: The near-field maximum amplitude as it changes with depth for each source volumes with contour lines as well as colour bar indicating the changes in asymmetry for a) P1 where *x* = 2 m b) P2 where *x* = 3 m and c) P3 where *x* = 6 m. The new breaking limit of am/h is shown as the dark black line, which initially corresponds to *As*=-0.5 at P1.

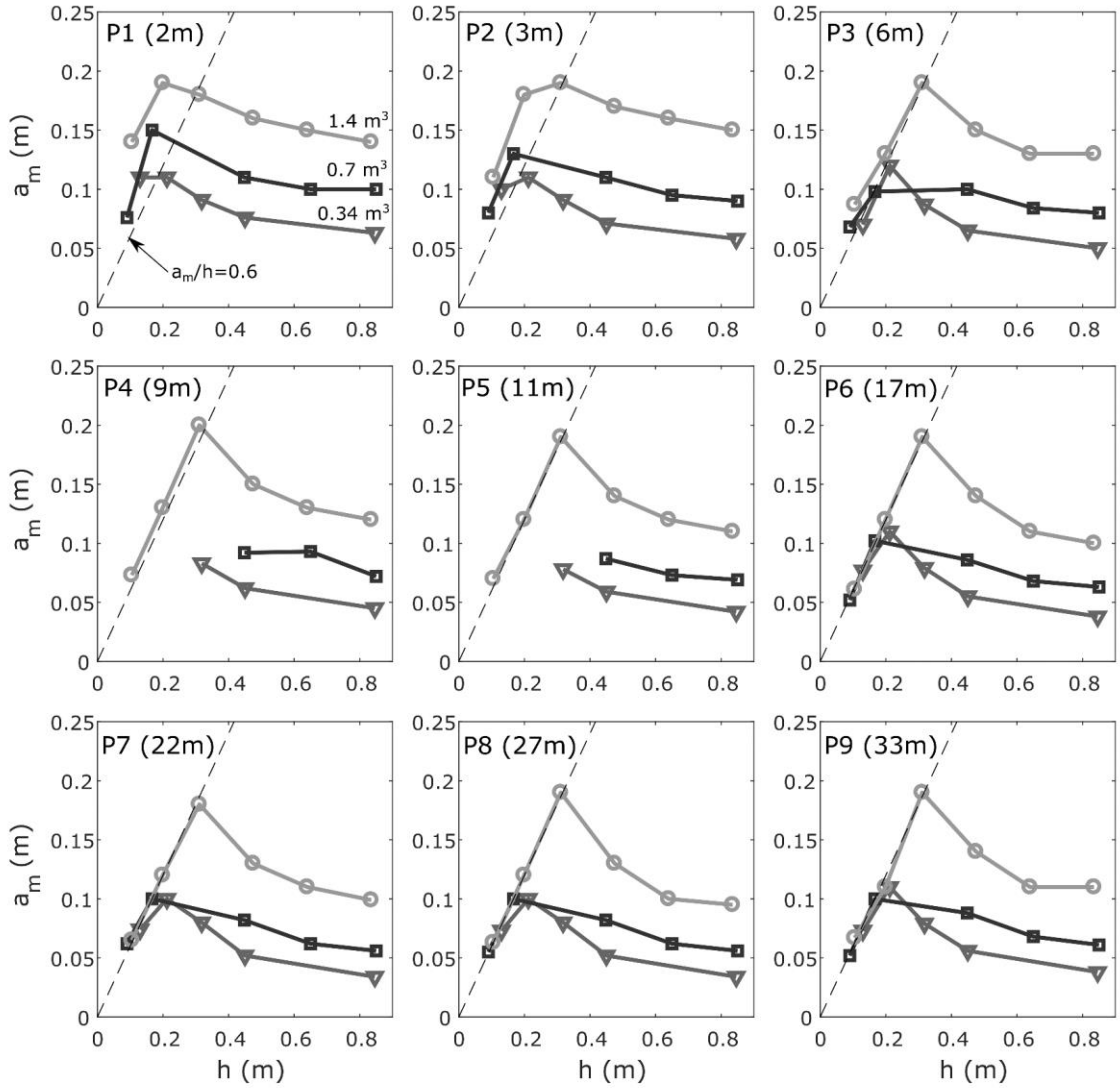

Figure 4.11: Maximum wave amplitude for each volume (0.34m^3-1.4m^3) at each probe location P1-P9 with a dashed line indicating the stable maximum wave amplitude when a_m/h = 0.6. Missing data points due to probe calibration error.

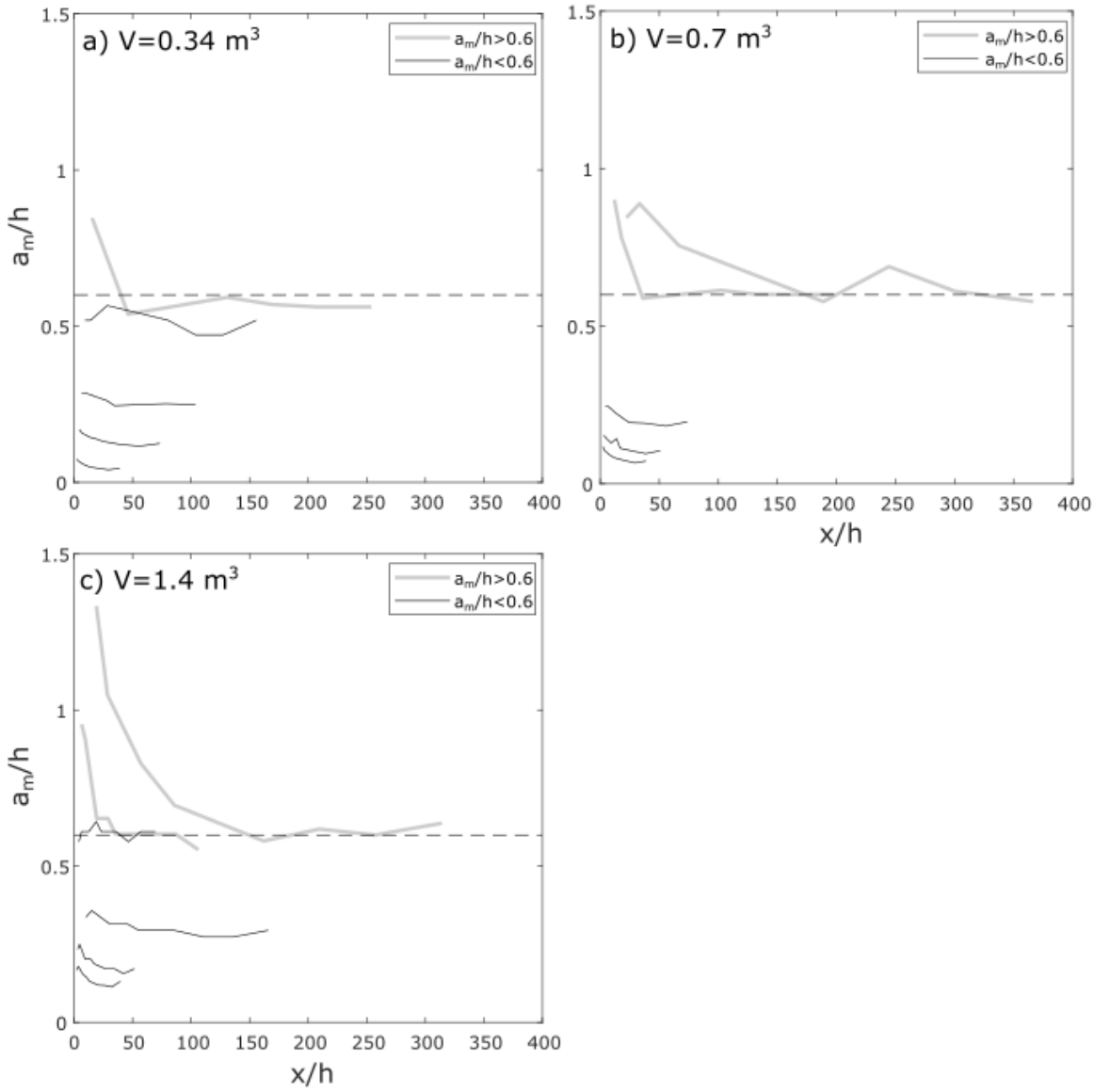

Figure 4.12: Evolution of the relative maximum wave amplitudes with relative distance for each source volume. Two distinct behaviours are noted with breaking waves shown in grey and solitary waves shown in black.

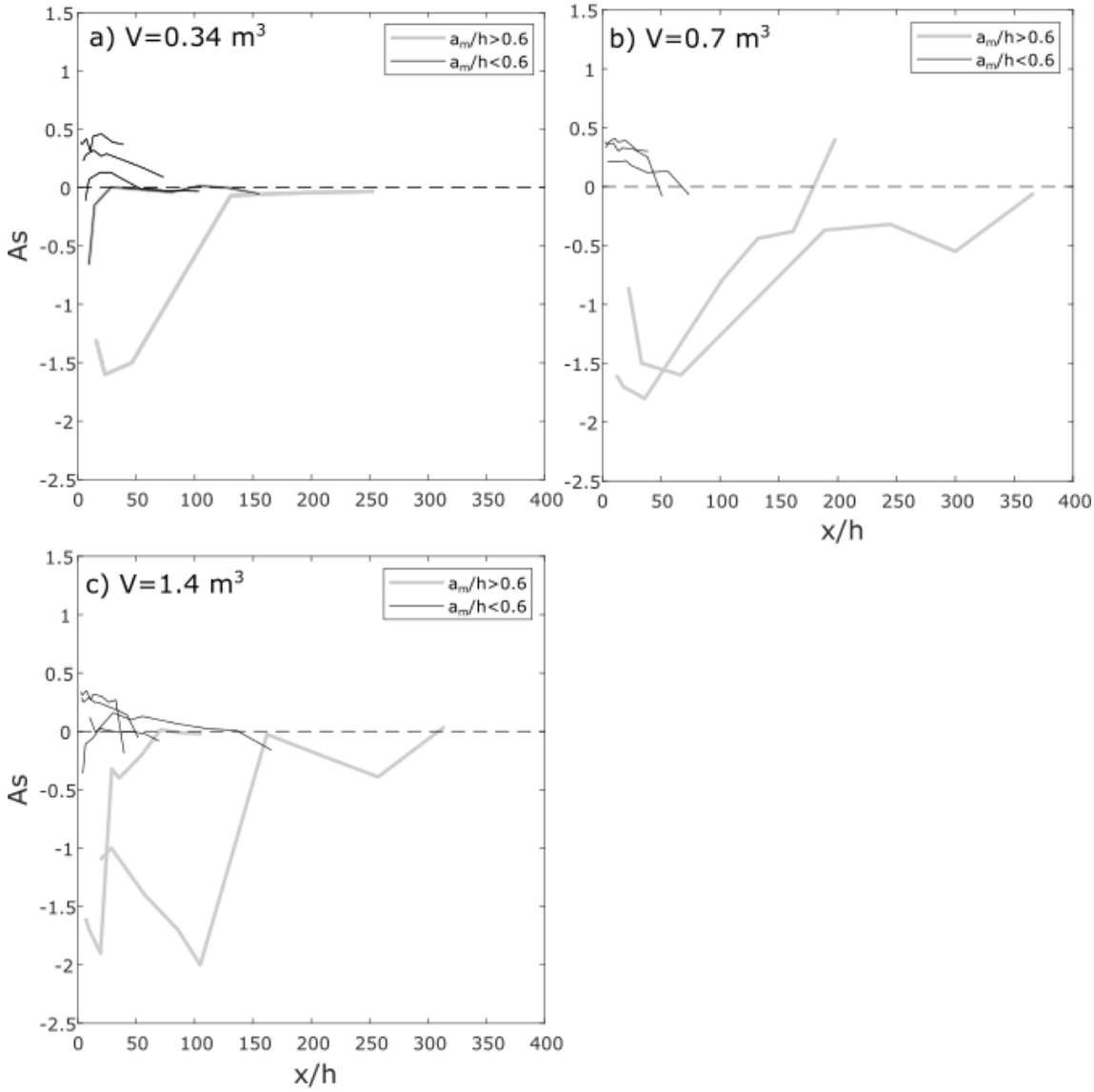

Figure 4.13: Measured wave asymmetry with relative distance for each source volume. The new breaking limit of a_m/h=0.6 divides the behaviours shown by breaking and non-breaking waves.

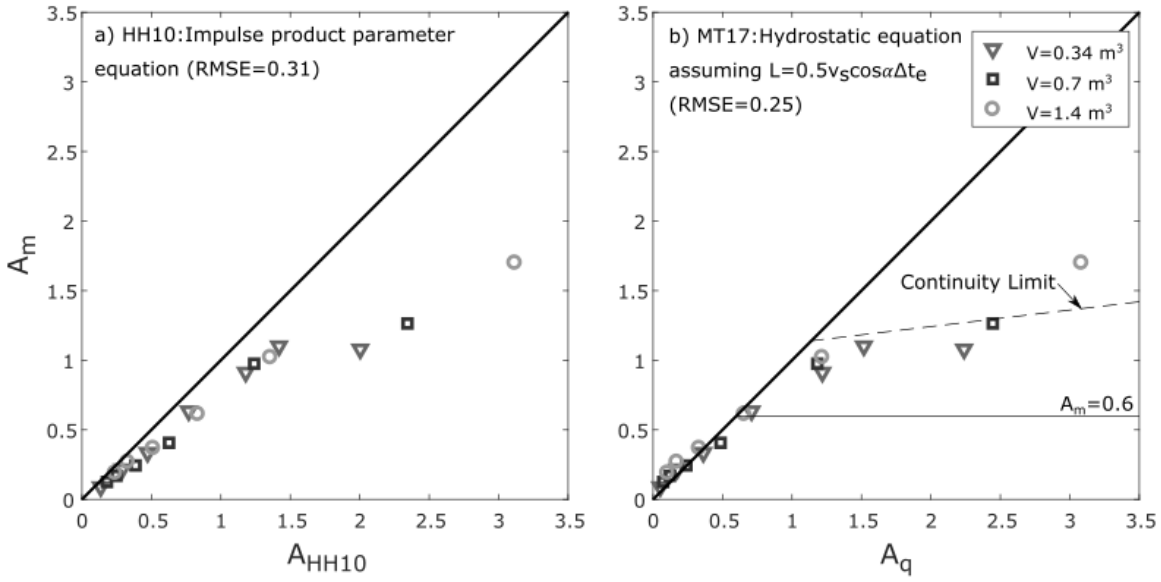

Figure 4.14: Comparison of the relative maximum amplitude obtained from the wave traces at a different *x* for each test to previously developed equations a) Equation for the impulse product parameter applied to granular landslides (Heller and Hager, 2010) ; b) Hydrostatic momentum balance equation using the simplification previously applied by Mulligan and Take (2017) to eliminate the length of forcing and time terms: where $L_e = \frac{1}{2} v_s cos\alpha \Delta t_e$. The continuity limit is shown as the dashed line and the new breaking limit is shown as the thin black line.

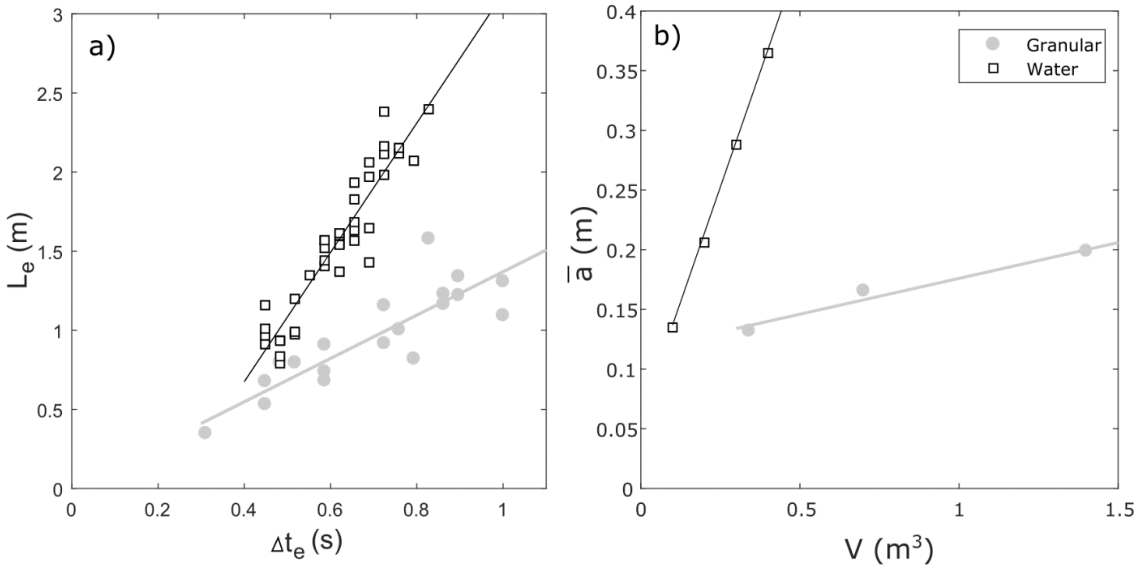

Figure 4.15: Comparison between the near-field properties of highly mobile slides, described in Chapter 2 and the long and thin granular landslides preformed in this study a) Highly mobile slides produce much larger waves in the near-field for a respective volume; b) The highly mobile slides have a much larger forcing zone and propel the wave forward for a longer period of time.

Chapter 5

Waves generated from highly mobile saturated granular flows

5.1 Introduction

The term mobility is often used to collectively describe the relative magnitude of the velocity and distal reach characteristics of a landslide. Different classes of landslides exhibit a wide range of mobility, in which velocities can be classified (e.g. Cruden and Varnes, 1996; Hungr et al. 2014) from extremely slow (< 16 mmyear^{-1}) to extremely rapid (> 5 ms^{-1}), significantly influencing the magnitude of deformation or distal reach of the landslide debris during a time period of interest. In practice, dynamic analysis of landslide motion is most commonly conducted using numerical models adopting a shallow flow approximation to predict the velocity and distal reach of the debris using either a Voellmy or frictional rheology (McDougall, 2016). In these models, the basal friction, internal friction, and the turbulence coefficient in the case of the Voellmy rheology are calibrated using data from past events to enable semi-empirical predictions of the behaviour of future landslide scenarios. In both of these rheologies, pore fluid pressure is a term of critical importance, as it directly reduces interparticle normal stresses leading to a drop in frictional resistance (e.g. Hungr, 1995) and subsequent significant increase in mobility. Porosity between grains is also important, and a recent study by Lindstrøm (2016) indicates that large voids between granular particles have a strong influence on the impact of a landslide with water.

For the case of a cascading hazard such as the generation of an impulse wave from the impact of a landslide into a body of water, the submerged distal reach of the landslide debris is not typically primary concern, but rather this characteristic directly affects the time and length scale of forcing. This in turn affects the near-field wave amplitude that can be generated from a given landslide impulse (Mulligan and Take, 2017; Zitti et al., 2015). This concept is illustrated in Figure 5.1 in which two landslides with the same thickness, velocity and impact angle enter a reservoir with the same depth, yet produce significantly different wave amplitudes in the near-field if one is highly mobile (HM) and the other has a low mobility

(LM). For the LM landslide, illustrated in Figure 5.1 as a dry granular frictional material, the flow impacts the reservoir and immediately begins to decrease in velocity. Once the wave speed exceeds the velocity of the submerged landslide, the wave is released from the influence of the landslide and propagates away from the wave generation zone. Over a comparable period of time, the HM landslide, illustrated in Figure 5.1 as a fluidised material, does not experience such a drastic reduction in velocity, permitting a much larger volume of water to be involved in the development of the first and largest wave.

The properties of the waves generated by these two different mobility scenarios have been recently investigated in Chapter 2, using water as the impacting flow material within a hypothesis that this scenario would be an upper bound of landslide mobility. However, this hypothesis has yet to be fully tested, and it is unclear whether a high-mobility saturated granular flow would produce tsunami waves that more closely resembled the dry granular flows due to a higher density than the water flow, or if the high mobility of the saturated granular flow creates behaviour more similar to the fluid flows hypothesised to be the worst-case scenario. The objective of this paper is to test this hypothesis by conducting an experimental parametric study in which a saturated source volume of 3 mm ceramic particles is released to create a high mobility saturated granular flow to compare the characteristics of the resulting tsunamis against the results of purely water flows investigated in Chapter 2 and dry granular flows of the same 3 mm diameter ceramic particles reported in Chapter 4. In so doing, the aim of this study is to clarify whether a wave amplitude equation derived from high or low mobility tsunamigenic landslides is applicable to landslides with high fluid pore pressures.

5.2 Materials and Methods

This study is comprised of a total of five new tests conducted in the Queen's University landslide flume, using saturated granular landslides to generate tsunamis. A constant source volume (V = 0.4 m^3) of 3 mm ceramic beads were released into reservoir depths (0.2 m < h < 0.6 m). The source volume was fully saturated before release which, given a void ratio (e) of 0.376, results in a bulk density (ρ_s) of 1776 kg/m^3.

Further details describing the dry granular material used in this study are described by Coombs et al. (2018). The observations from saturated granular landslides combined with results from and highly mobile and dry granular slides. Further details regarding the tests with highly mobile landslides using water as the source volume are described in detail in Chapter 2 and Chapter 3. Further details regarding the tests with dry granular landslides are described in detail in Chapter 4.

5.2.1 Landslide Flume

The Queen's University landslide flume has an aluminum box at the top of a 6.73 m long 30° slope where the source volume is held prior to release (Figure 5.2). Once the door is triggered, the material slides down the long slope and into the 33.8 m long base of the flume, which is filled with water to varying depths. The flume has a constant width and height of 2.10 m and 1.21 m for both the slope and the base. The sidewalls in the near-field are tempered glass and transition to concrete blocks at a distance of 3.7 m away from where the slope meets the base. Further details describing the specifications of the experimental setup are described in Chapter 2.

5.2.2 Cameras

The landslide thickness and velocity were measured using a Sony DSC-RX10M2 equipped with a SONY Vario-Sonnar T* Carl Zeiss 2.8/8.8-73.3 lens at 480 Hz with a resolution of 1920x1080. The thickness was measured using "Cam 1", which is rotated at 30° such that the horizontal of the images is parallel with the slope. The velocity was measured using "Cam 2", which is rotated 30° upwards such that the line of sight is normal to the slope. The entire length of the near-field was captured using "Cam 3", a Canon Rebel T5i recording at 29 Hz with a resolution of 1929x1101 pixels. Cam 3 was used to quantify the time and length of wave release. The velocities of the submerged particles were analyzed using "Cam 4", which was also a Sony DSC-RX10M2 with the same lens and resolution recording at 960 Hz. The light source for all of the cameras is a high-speed flicker free Pallite VIII.

5.2.3 Sensors

The changes in water surface elevation (η) were measured using nine wave probes 0.6 m in length at varying stations along the centreline of the flume. The probes record at 100 Hz and are accurate to $\pm$0.001 m at locations of x = 1.9, 3.1, 6.0, 8.8, 11.3, 16.8, 22.0, 26.6 and 32.5 m from the origin at the base of the landslide slope. The deposit shape was measured using a FARO Focus Laser Scanner with 3 mm resolution at two positions, shown as F1 and F2. The scans use target-based registration to register the individual scans to one another. Three target spheres were located in the field of view and used to geo-reference the data. The locations are details of the FARO Focus Laser Scanner are described by Coombs et al. (2018).

5.3 Results and Analysis

5.3.1 Landslides

The impact properties of saturated granular landslides were compared to two other landslides at opposite end of the spectrum of landslide mobility. These include highly mobile (HM), where water with a source volume of V = 0.40 m^3 is used as the sliding material, and slides with lower mobility (LM), where dry granular material with a similar source volume (V = 0.34 m^3) is used. The landslide impact velocity and thickness for the three landslide types are compared in Figure 5.3. All three landslides impact the reservoir at t = 0 s at a high velocity, ranging from 5.4 ms^{-1} to 6.5 ms^{-1} and a similar thickness of 0.037 m to 0.042 m. The landslide velocity and thickness decreases in the shortest amount of time for the HM landslide and the longest for the LM landslide. The thickness and velocity was not captured for the entire length of the landslide for the granular materials; however, the thickness and velocity 3 s after the initial impact does not influence the characteristics of the impulse wave, which are the focus of this study. The increased variability of both the velocity and thickness for the HM landslide is due to the turbulent surface of the sliding water.

The deposit shapes for the same volume of saturated granular and LM landslide can be compared for two different cases (Figure 5.4). The first case, where h = 0 m, demonstrates the longest possible runout distance (L_m) for both landslide types due to the landslide not transferring any momentum into the formation of a wave (Coombs et al., 2018; Steers et al., 2018). The LM landslide sits directly at the bottom of the slope (L_m = 1.61 m) and is relatively symmetrical about the z-axis, whereas the saturated flow travels much farther along the base of the flume (L_m = 3.32 m) and has a pitched forward front. The shape of the deposit has been quantified using the centre of mass (COM), indicated by the "+" symbol. The COM has an x-coordinate of 2.22 m and 1.23 m for the saturated granular and LM landslides respectively.

The total runout length for the saturated granular (L_m = 3.08 m) and LM landslide (L_m = 1.23 m) is marginally smaller with the addition of a reservoir (h = 0.2 m). The larger change is in the position of the COM for both landslide mobility cases (Δx = -0.99 m for saturated granular flows and Δx = -0.61 m for dry granular flows). It is hypothesized that the LM flow experiences a smaller change in COM position with the addition of a reservoir due to the original proximity to x = 0.0 m under dry conditions. The material for the LM flow is limited in the x-direction and is therefore forced vertically.

The landslide parameters of impact velocity and thickness and the total runout for each of the three landslide cases can be compared in order to determine an order of mobility. It is clear that the mobility of the saturated case is larger than the LM granular landslide; however given that the HM flows do not produce a deposit it is difficult to determine if the saturated tests conducted in this study are in fact exactly in between the HM and LM cases previously discussed in Chapter 2 and Chapter 4. A summary of the averaged thickness and velocity over the first 1 s and the total runout distance is shown in Table 5.1.

Table 5.2: Average landslide parameters for $V = 0.4$ m^3, $h = 0$ m

	Water	Saturated Granular	Dry Granular
v_s (ms^{-1})	6.24	4.79	4.61
s (m)	0.046	0.041	0.033
L_m (m)	N/A	3.32	1.61

5.3.2 Momentum Transfer

5.3.2.1 Near-field Wave Generation

The landslide impact observations indicate that each landslide type has different mobility, results in a drastically different runout distance. The role of mobility on wave generation can be investigated visually for each of the three landslides as they impact a reservoir of constant depth, $h = 0.2$ m. As observed from Cam 4, the LM granular flow produces a very small wave, which has been outlined in white in order to differentiate it more clearly. At the early stages of time ($t = 0$ s upon impact), the submerged landslide initially expands to form a large bulbous front, which propagates directly underneath the wave as it continues to push the wave forward. At $t = 0.784$ s, the wave crest overtakes the front of the submerged landslide and continues to propagate away from the front as the separation increases at $t = 1.01$ s. The cloud above the water surface is dust from the granular material, which can only be seen in this test because it was the first time they were submerged in water. The HM slide demonstrates a similar submerged behaviour, with the increase in thickness to form a bulbous front at initial stages in time (Figure 5.6). It is difficult to distinguish between the size of the submerged bubble plume and the turbulence from impact in the reservoir; however, the size of the plume is much larger in both height and length than the LM slide. The HM slide creates a very pitched forward wave with a much larger amplitude, which reaches a similar point in space as the LM landslide in approximately 60% of the time. The saturated granular landslide traps air inside in the bulbous front, which forms due to the upward displacement of the slower moving particles from the faster particles behind (Figure 5.7). The entrained air forms a pocket, which moves and changes in shape with the submerged landslide. Eventually, the

individual particles begin to settle as the forward velocity decreases and this bubble is forced to the surface. The saturated flow propagates at a rate in between the LM and HM landslides and creates a maximum wave more similar to the HM flow in both size and shape.

5.3.2.2 Particle Image Velocimetry Analysis

An analysis on the submerged landslide velocity was conducted using geoPIV-RG (Stanier et al., 2015) for waves from each type of slide at a similar *x* location, shown in Figure 5.8. In this figure, the vectors indicate an average displacement in a 2.76 x 3.67 cm grid over 0.0156 s. All three cases indicate the largest particle displacements prior to impacting the reservoir. The velocity vectors from the LM landslide are significantly smaller in comparison to the other types. This frame is after the wave has been released and the submerged landslide is coming to a halt.

The vectors in the HM landslide case demonstrates an upwards motion after the submerged particles at the front have slowed down and are being displaced by the faster moving particles behind. This creates a small zone near the base of the flume at the front as well as in the middle of the plume where very little displacement occurs. Most of the incremental displacement vectors on the impact side of the wave have reached a maximum height and are falling down to create the long tail, which is characteristic of breaking waves.

The saturated case follows very closely to the HM landslide submerged behaviour. The largest displacement vectors impact the reservoir and stay at the bottom of the submerged landslide. Once the particles begin to slow, they are displaced vertically by the faster moving particles behind. This translates to the largest forward displacement of the front occurring at a certain height above the base of the flume. On the impact side of the wave, the displacement vectors are all pointing down as the beads have lost their forward propulsion and are beginning to settle. The air pocket described earlier is in a similar position in the submerged landslide as the location of zero displacement in the bubble plume in the HM

case. Overall, the behaviour of the submerged saturated landslide is more comparable to the HM landslide and will therefore create a wave whose amplitude and shape are more closely related to the HM landslide.

The PIV data allow for the comparison of the submerged mobility of each of the three types of landslides. The mobility of the landslide which influences the size of the wave is not the complete runout distance but the effective length of forcing L_e prior to wave release. The definition of wave release is the point at which the wave speed, $c_s = \sqrt{g(a_m + h)}$, exceeds the submerged landslide velocity. The depth (h) is constant for each case; however, the maximum wave amplitude a_m varies significantly. Therefore, the cases with a higher mobility also have a higher submerged landslide velocity at the time of wave release.

5.3.3 Wave Evolution

The time series from each wave probe are shown in Figure 5.9, with the time adjusted such that the peak reaches the probe at t_{peak} = 0 s. The observations from the near-field probe (P1) indicate that waves generated by the saturated granular slide have a maximum amplitude in between those forced by the HM and LM landslides. The HM and the saturated granular slides both attenuate rapidly with distance along the flume from P2-P5 according to the breaking limit a_m/h = 0.60 described in Chapter 2. In the far-field (e.g., P6-P9) the wave amplitudes are similar for all three cases, however the wave shapes are significantly different. The changes in wave amplitude and wave shape, quantified by the asymmetry, along the flume are shown in Figure 5.10. These results indicate that the properties of waves generated by the saturated granular flows are almost exactly the same as those generated by highly mobile slides. The saturated granular and HM landslide waves decrease in maximum wave amplitude due to wave breaking, while the LM landslide has almost no change in amplitude since the near-field amplitude does not exceed the wave breaking limit. The shapes of waves generated by the saturated granular and HM consequently have highly negative asymmetry and as the waves evolve they become more asymmetrical until fully broken and the wave shape becomes symmetrical.

The maximum wave amplitude at each of the wave probes is compared for similar source volumes in varying reservoir depth for the three landslide mobility types in Figure 5.11. The influence of mobility on the size of the waves is clearly evident in the near-field at P1. As in Chapter 2, the breaking wave limit of $a_m/h = 0.6$ controls the maximum wave amplitude in the far-field. The results for the saturated granular and HM landslide waves are remarkably similar in the far-field, suggesting that it would be reasonable to use the HM landslides to predict the behaviour of the fully saturated granular landslide when interested in predicting the far-field wave properties.

5.3.4 Influence of Mobility on Time and Length Scales

The effective length of momentum transfer was measured using the images from Cam 3 and qualitatively selecting the time (Δt_e) at which the wave begins to separate from the submerged landslide. At this time, the horizontal length of the submerged landslide (L_e) was measured from the point at which the water surface intersects the flume slope to the front of the submerged landslide plume. The relationship between the time and length scales have been quantified for the 19 LM dry granular tests described in Chapter 4, the 41 HM slides described in Chapter 2 and the five saturated granular tests conducted herein (Figure 5.12). The velocity of the LM and HM landslides were averaged for all source volumes and the mean values were 4.6 ms^{-1} and 5.4 ms^{-1} respectively. Since the saturated granular tests did not vary in source volume, the velocity of 4.9 ms^{-1} averaged over the first 1 s of the landslide was applied. The results shown in Figure 5.12 indicate that the slope of each line is significantly different. This suggests that the underwater change in velocity after impact, defined as the mobility factor (ι_s), can be used to quantify the relationship between L_e and t_e over the range of landslide mobility. This is expressed as

$$L_e = \iota_s v_s cos\alpha \Delta t_e \qquad \text{(Eq. 5.1)}$$

As indicated in Figure 5.12, the saturated granular slides have a mobility factor of $\iota_s = 0.66$, that lies between the values for the HM and LM landslides. These results are encouraging, as they are the first experimental evidence of time and length scales that effect wave generation, and underscore the

importance of landslide mobility on wave generation. The observations also provide validation of previous assumptions for HM landslides (ι_s = 1) as discussed in Chapter 2 and LM landslides (ι_s = 0.5) as described in Chapter 4. These assumptions for the HM and LM landslides are approximately correct, with measured mobility factors equal to ι_s = 0.87 and ι_s = 0.45 for HM and LM landslides respectively.

5.4 Comparison of Near-field Amplitudes with Published Relationships

The momentum-based equation derived by Mulligan and Take (2017), hereafter referred to as MT17, quantifies the near-field maximum wave amplitude a_q generated by dry granular landslide as:

$$a_q = \sqrt{h^2 + \frac{2\rho_s s v_s \cos\alpha L_e}{\rho g \Delta t_e}} - h \qquad \text{(Eq. 5.2)}$$

Substituting the new velocity relationship (Eq. 5.1) into Eq. 5.2, yields

$$a_q = \sqrt{h^2 + \frac{2\iota_s \rho_s s (v_s cos\alpha)^2}{\rho g}} - h \qquad \text{(Eq. 5.3)}$$

where ι_s accounts for the landslide mobility. The measured ($A_m = a_m/h$) and predicted ($A_q = a_q$/h) values of the near-field relative maximum wave amplitude for each landslide type are shown in Figure 5.13. Overall, by including the appropriate value of the mobility factor shown in Figure 5.12, the predicted relative amplitudes are in much closer agreement with observations for saturated granular slides than if the simple assumptions applied in Chapter 2 for highly mobile slides (ι_s = 1.0) and in Chapter 4 for dry granular slides with lower mobility (ι_s = 0.5). The predictions result in root-mean-square (RMSE) errors of 0.16 for water and 0.20 for the combination of dry granular and water-saturated granular material. The mobility factor therefore expands the range of applicability of this predictive equation to landslides with a wide range in mobility.

5.5 Conclusions

An experimental study was conducted in a large-scale landslide flume, using a constant volume of saturated granular flows to generate impulse waves into varying reservoir depths. A series of high

frequency cameras were used from various angles to measure the impact velocity and thickness and the observations were compared to saturated granular slides with lower mobility (LM) using dry granular material and higher mobility (HM) flows using water of a similar volume. The HM flows have the highest velocity and thickness at impact and the LM landslides have lower velocity and thickness. The saturated granular flows have an impact velocity and thickness that is intermediate between these two end-member landslide types. The deposit shapes were created by the saturated granular and dry granular slides were also compared, for cases with and without water in the reservoir at the base of the landslide slope. In the case of no water in the reservoir, the centre of mass of the landslide deposits extend significantly father horizontally compared to when the slides land in water. When there is water in the reservoir the submarine runout distance has only a small range of variability for different water depths, however the water depth influences wave breaking and thus controls the wave amplitude.

The waves generated by three types of landslides with different mobility were compared using Particle Image Velocity analysis of the digital images and time series analysis from wave probes along the length of the flume. The observations reveal that in the near-field, waves generated by saturated granular flows have maximum amplitudes that are intermediate between the HM and LM landslide types. In the far-field, as the waves propagate away from the impact site, tsunamis generated by saturated granular flows behave essentially the same as those generated by highly mobile slides indicating the importance of mobility. The near-field wave observations were also compared to a momentum-based predictive equation developed by Mulligan and Take (2017) for dry granular landslides. A new mobility factor was developed to quantify the relationship between the time and length scales over which the momentum transfer takes place, improving the predictive equation for maximum wave amplitude to cover a wide range of landslides with different mobility.

To better quantify the effects that mobility has on the maximum near-field amplitude of landslide-generated waves, a larger experimental data set for different volumes of fully saturated granular material

and consideration of the could be considered in future studies. In addition, it would be useful to include the landslide porosity in predictive equations, to account for the flow packing density at impact with water. However, the results of the present study clearly indicate the importance of time and length scales over which tsunamis are generated, and the strong link between landslide mobility and near-field wave properties. This method can now be applied to a variety of landslide types in order to estimate the near-field maximum wave amplitude.

5.6 References

Coombs, S.P., Apostolov, A., Take, W.A., and Benoît, J. (2018). Observed increase in mobility of dry granular landslides, corresponding to increase collisional activity, quantified by a smart rock sensor. *Canadian Geotechnical Journal (submitted)*.

Cruden DM, Varnes DJ (1996) Landslide types and processes. In: Turner AK, Schuster RL (eds) Landslides investigation and mitigation. Transportation research board, US National Research Council. Special Report 247, Washington, DC, Chapter 3, pp. 36–75.

Fritz, H.M., Hager, W.H. and Minor, H.E. (2004). Near field characteristics of landslide generated impulse waves. *Journal of Waterway, Port, Coastal, and Ocean Engineering*, *130*(6), 287-302.

Heller, V. and Hager, W.H. (2010). Impulse product parameter in landslide generated impulse waves. *Journal of Waterway, Port, Coastal, and Ocean Engineering*, *136*(3), 145-155.

Hungr, O. 1995. A model for the runout analysis of rapid flow slides, debris flows, and avalanches. *Canadian Geotechnical Journal*, 32 (4): 610–623. doi: 10.1139/t95-063

Hungr, O., Leroueil, S., and Picarelli, L. 2014. The Varnes classification of landslide types, an update. *Landslides* 11: 167-194.

Kamphuis, J.W., and Bowering, R.J. (1970). Impulse waves generated by landslides. *Proc., 12th Coastal Engineering Conf.*, ASCE, REST, Va. 1. 575-588.

Lindstrøm, E.K. (2016). Waves generated by subaerial slides with various porosities. *Coastal Engineering*, 116, 170-179.

McDougall, S. 2016. 2014 Canadian Geotechnical Colloquium: Landslide runout analysis—current practice and challenges. *Canadian Geotechnical Journal*, 54(5), 605-620.

Miller, G.S., Take, W.A., Mulligan, R.P., and McDougall, S. (2017). Tsunamis generated by long and thin granular landslides in a large flume. *Journal of Geophysical Research: Oceans*, 122,653-668, DOI: 10.1002/2016JC012177.

Mulligan, R.P., Take, W.A., and Bullard, G.K. (2018). Modelling tsunami from landslides with different mobility. *Coastlab18*, Santander, Spain, May22-26, 2018.

Mulligan, R.P., and Take, W A. (2017). On the transfer of momentum from a granular landslide to a water wave. *Coastal Engineering*, *125*, 16-22.

Stanier, S. A., Blaber, J., Take, W. A., and White, D. J. (2015). Improved image-based deformation measurement for geotechnical applications. *Canadian Geotechnical Journal*, *53*(5), 727-739.

Steers, L.J., Take, W.A., and Beddoe, R.A. (2018). *Static liquefaction of loose granular landslides* (Unpublished Master's Thesis). Queen's University.

Zitti, G., Ancey, C., Postacchini, M. and Brocchini, M. (2015). Impulse waves generated by snow avalanches falling into lakes. In *Proceedings of 36th IAHR World Congress, The Hague, Netherlands, 2015* (No. EPFL-CONF-215899). IAHR.

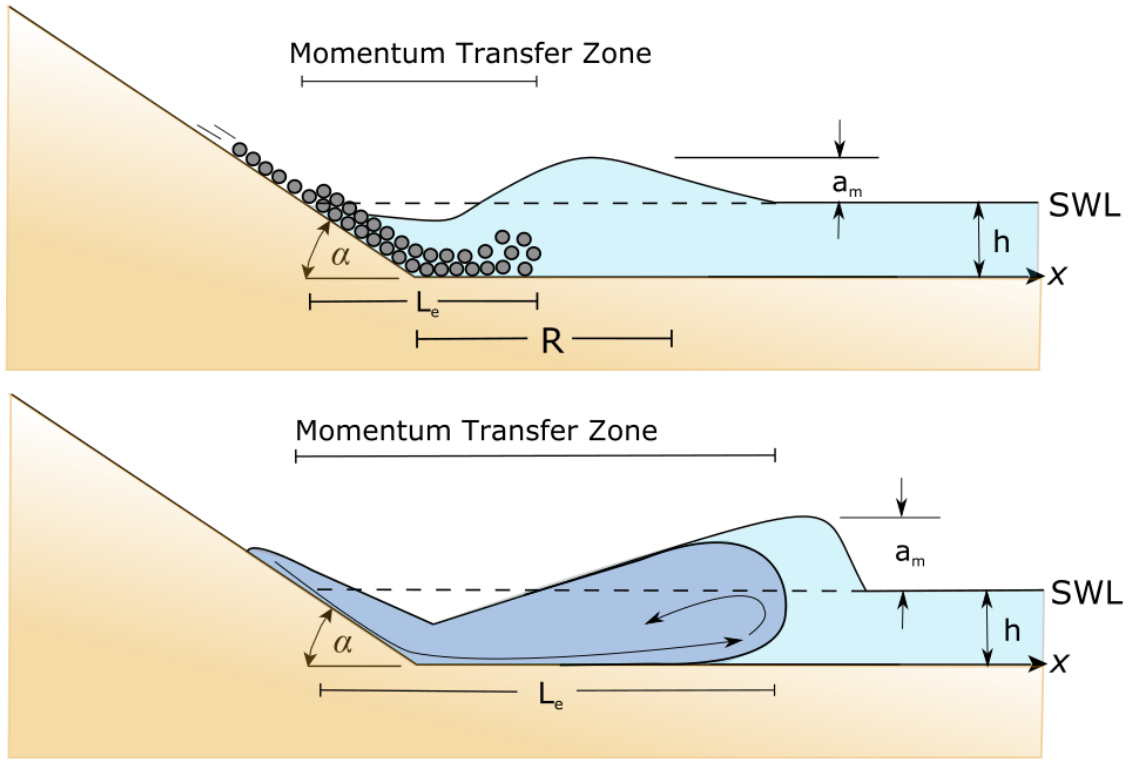

Figure 5.1: Conceptual sketch of wave generation by a granular landslide with lower mobility (top) and a debris flow with higher mobility (bottom), indicating the difference in maximum amplitude (a_m), effective length of the momentum transfer zone L_e and maximum runout distance R.

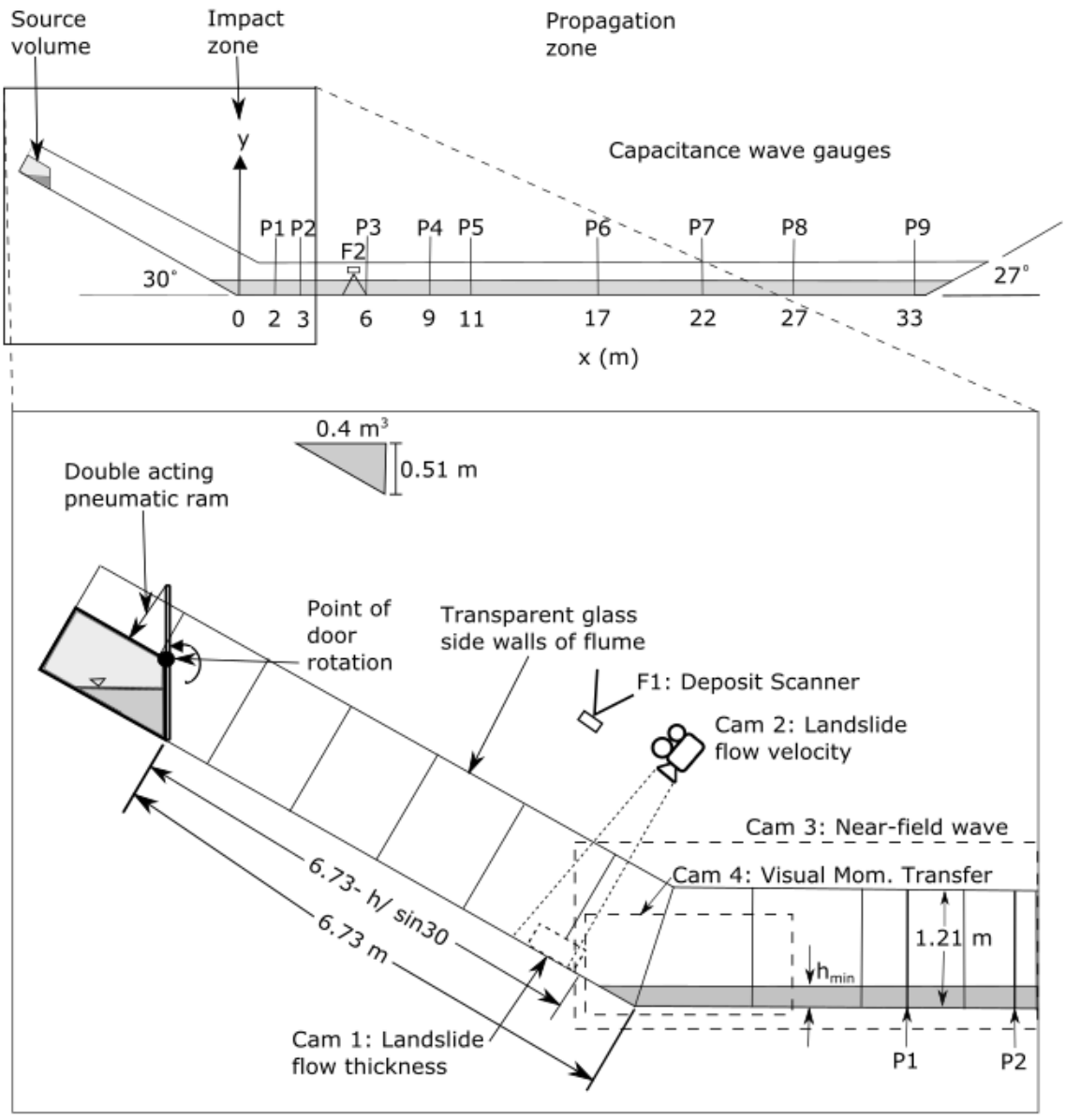

Figure 5.2: Experimental apparatus for measuring landslide generated tsunamis. The flume has nine wave probe locations from x = 1.9 m to x = 32.5 m labelled P1 to P9. The landslide slope detail (bottom) shows the field of view for each of the four cameras indicated by dashed lines and the location wave probes P1 and P2. The two locations of the deposit scanner are shown by F1 (above the deposit looking down the flume) and F2 (near the location of P3 looking up the slope of the flume).

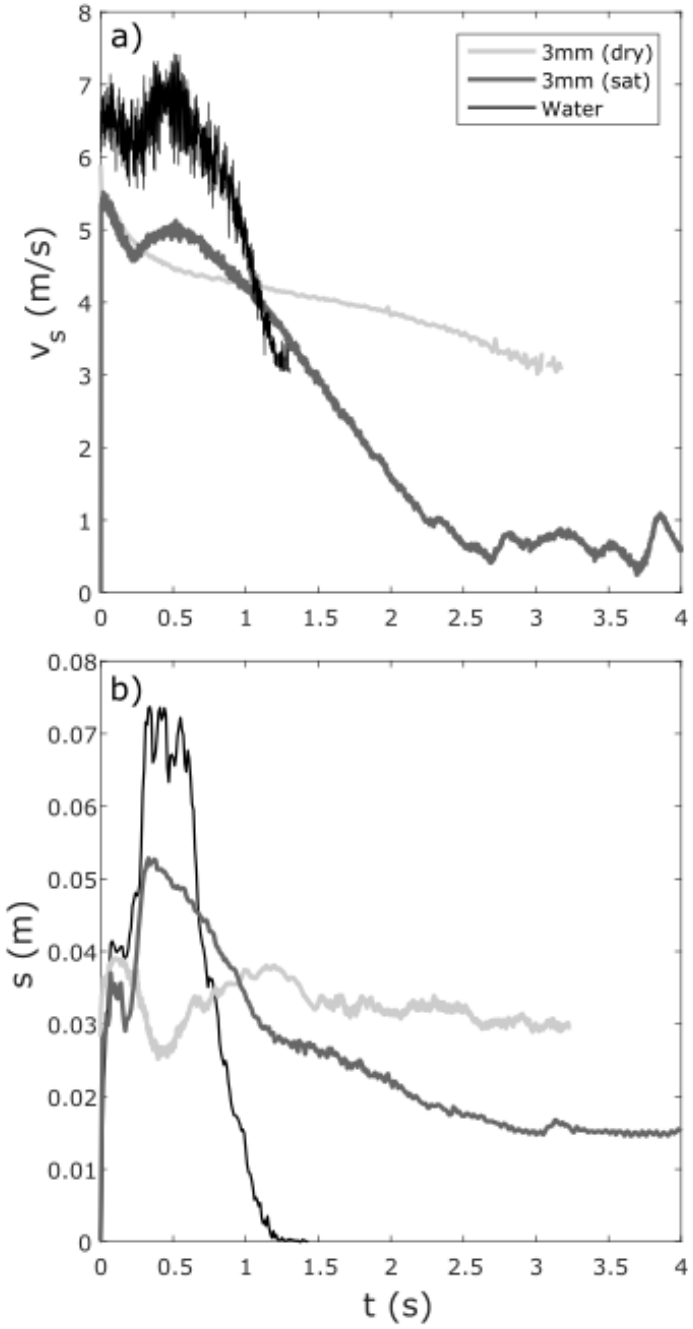

Figure 5.3: Time series variability of the landslide properties at impact for each of the three types. The velocity (v_s) is measured using PIV analysis of downward-looking images (Cam 2) and the thickness (s) is measured using side-looking images (Cam 1). The source volumes are V = 0.40 m^3 for the highly mobile (water) and saturated granular slides and V = 0.34 m^3 for the dry granular flows.

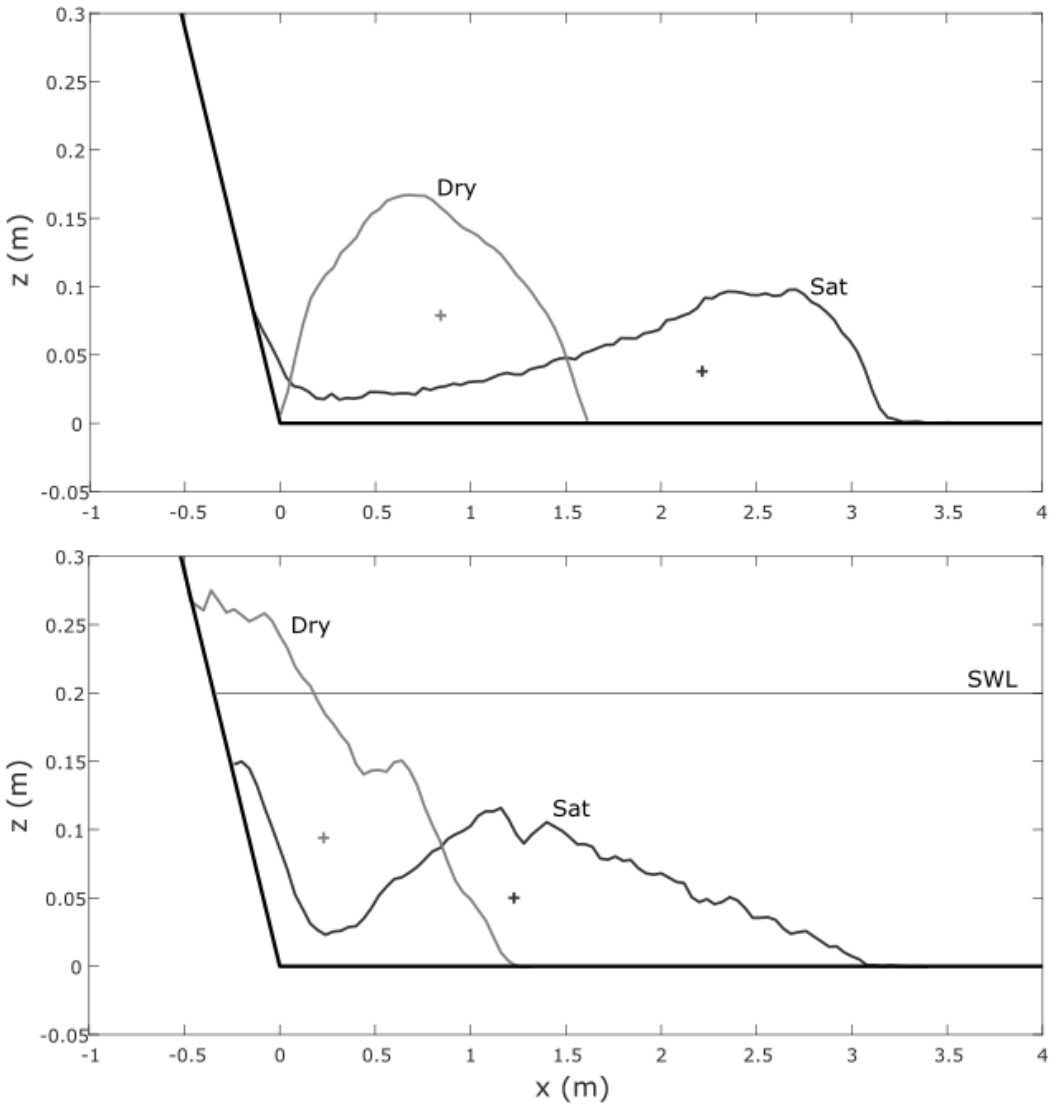

Figure 5.4: Longitudinal landslide deposit profiles for saturated and dry granular flows from experiments with V = 0.4 m^3 into reservoir water depths of h = 0 m (Steers et al., 2018; Coombs et al., 2018) and h = 0.2 m. The centre of mass for each deposit is identified by the "+" symbol.

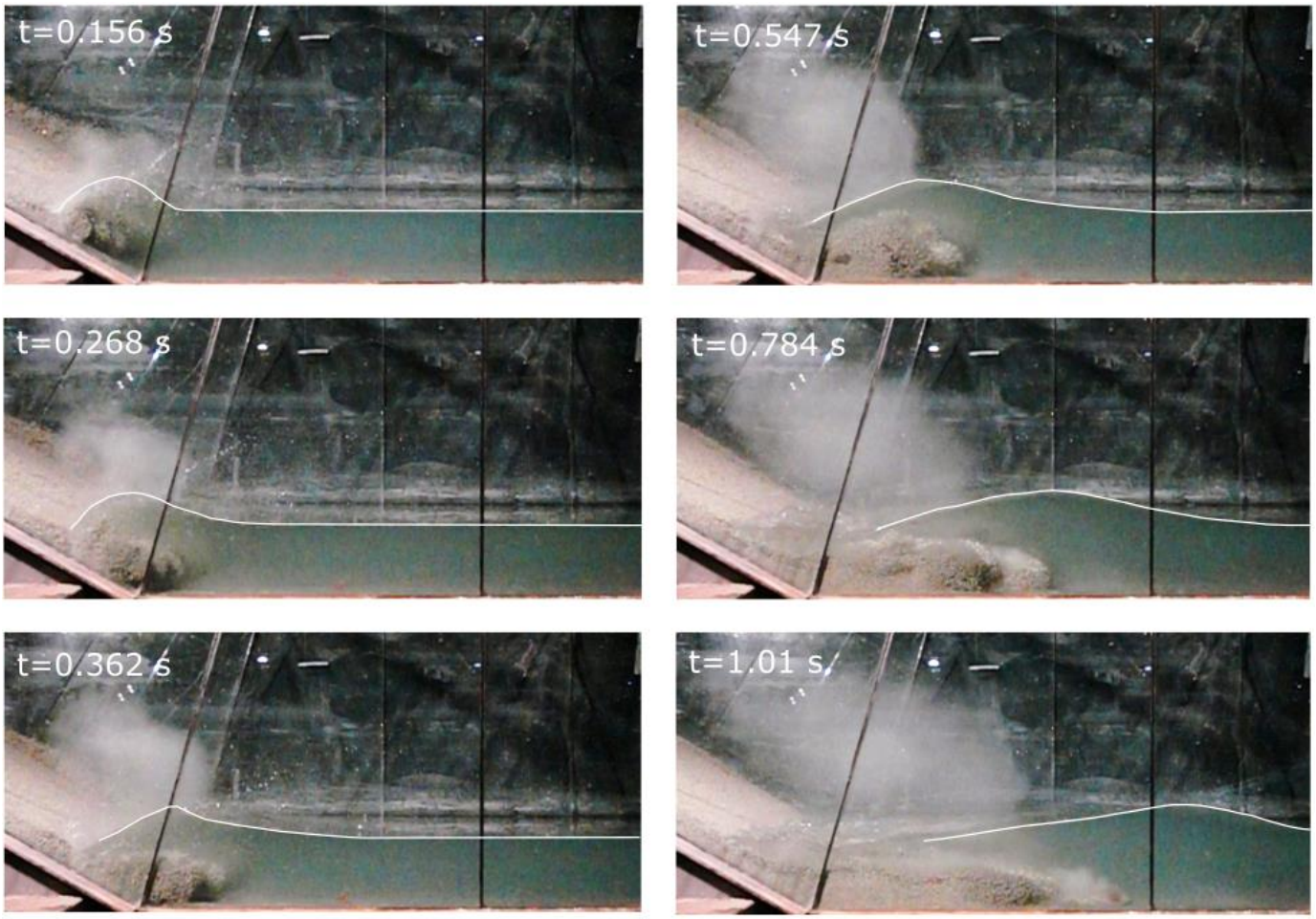

Figure 5.5: Time series of images for the dry granular landslide from Cam 4 relative to the initial point of impact where t = 0 s, for the experiment with V = 0.4 m^3 and h = 0.2 m.

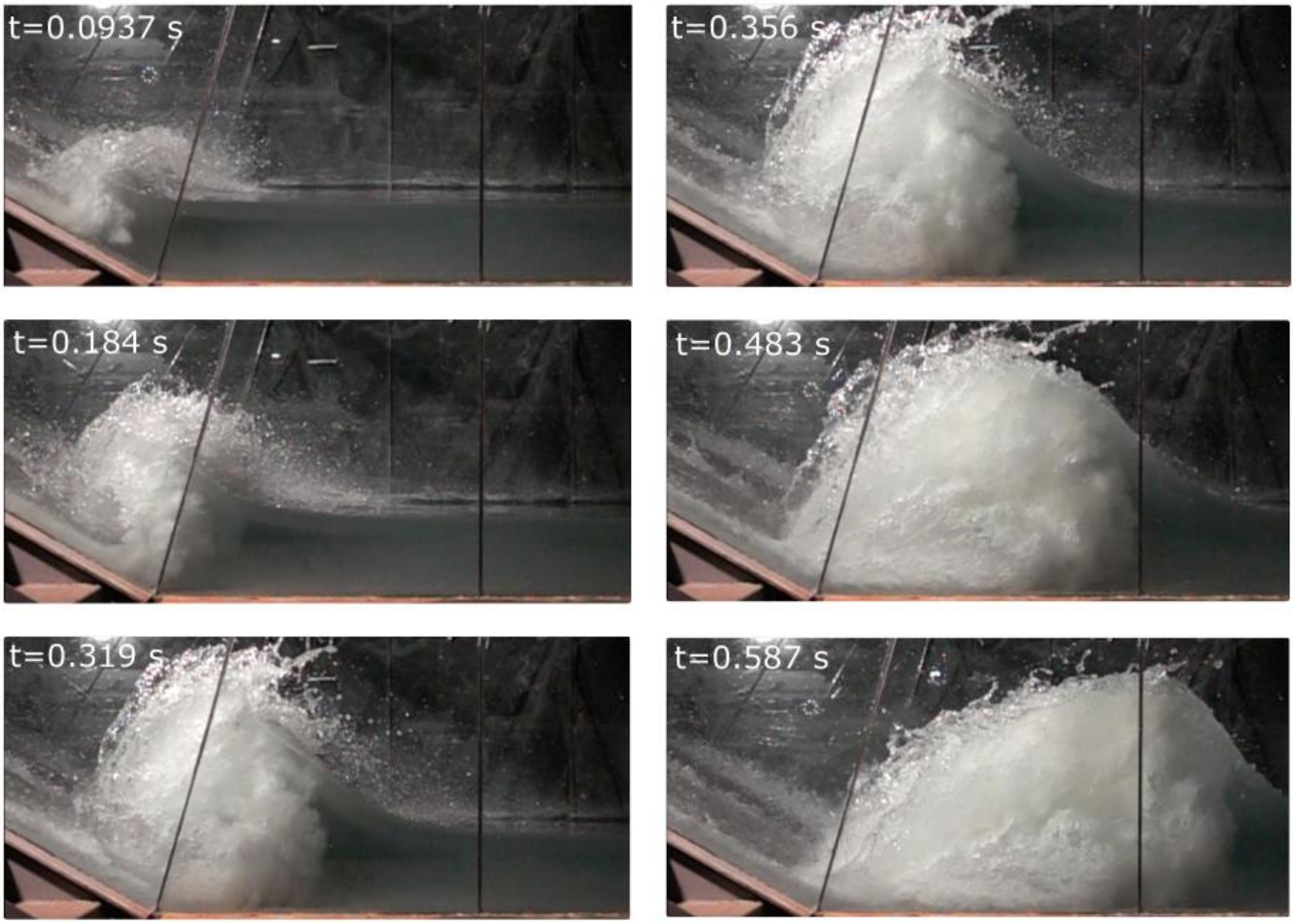

Figure 5.6: Time series of images for the highly mobile slides from Cam 4 relative to the initial point of impact where t = 0 s, for the experiment with V = 0.4 m^3 and h = 0.2 m.

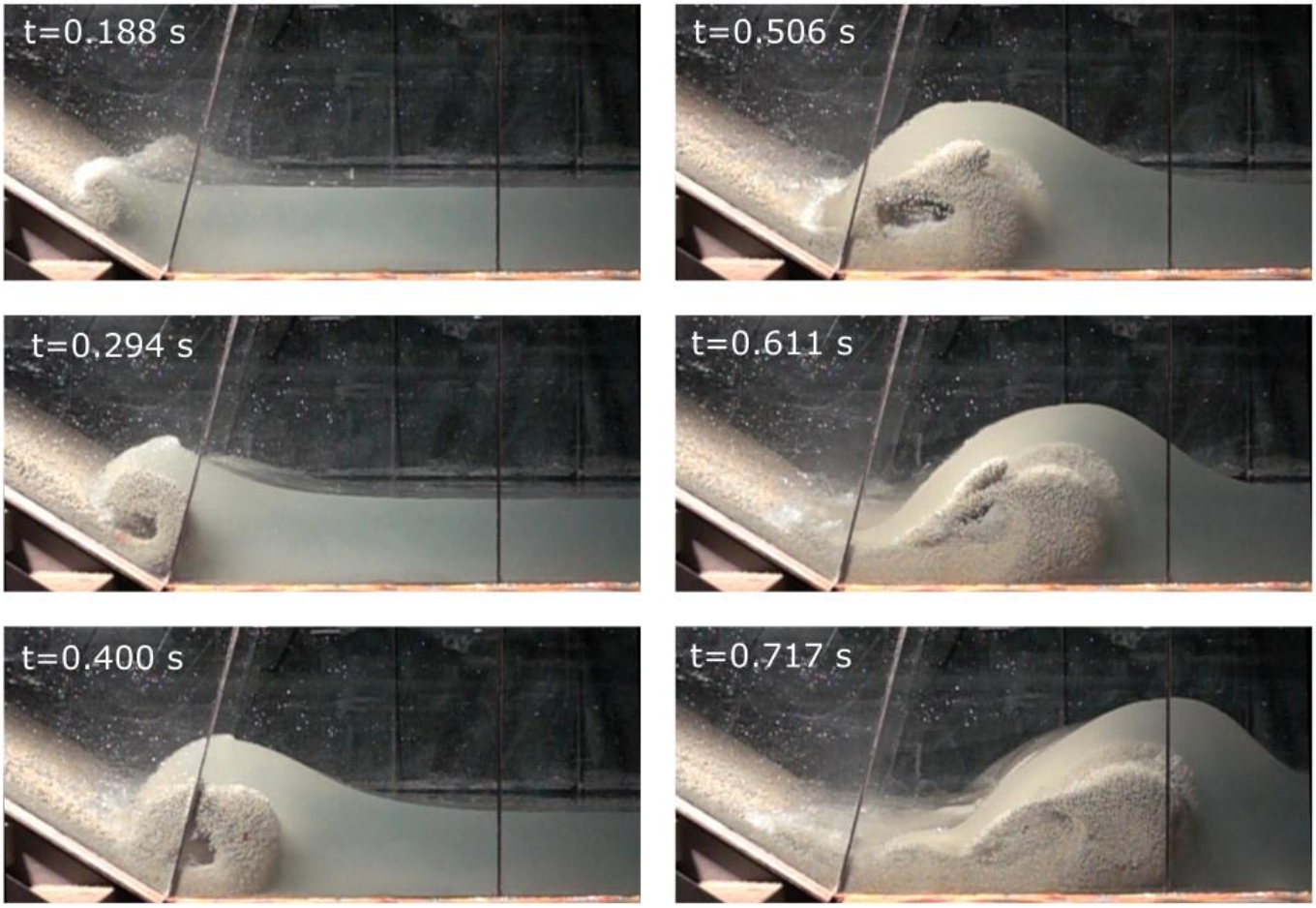

Figure 5.7: Time series of images for the fully saturated granular flows from Cam 4 relative to the initial point of impact where t = 0 s, for the experiment with V = 0.4 m^3 and h = 0.2 m.

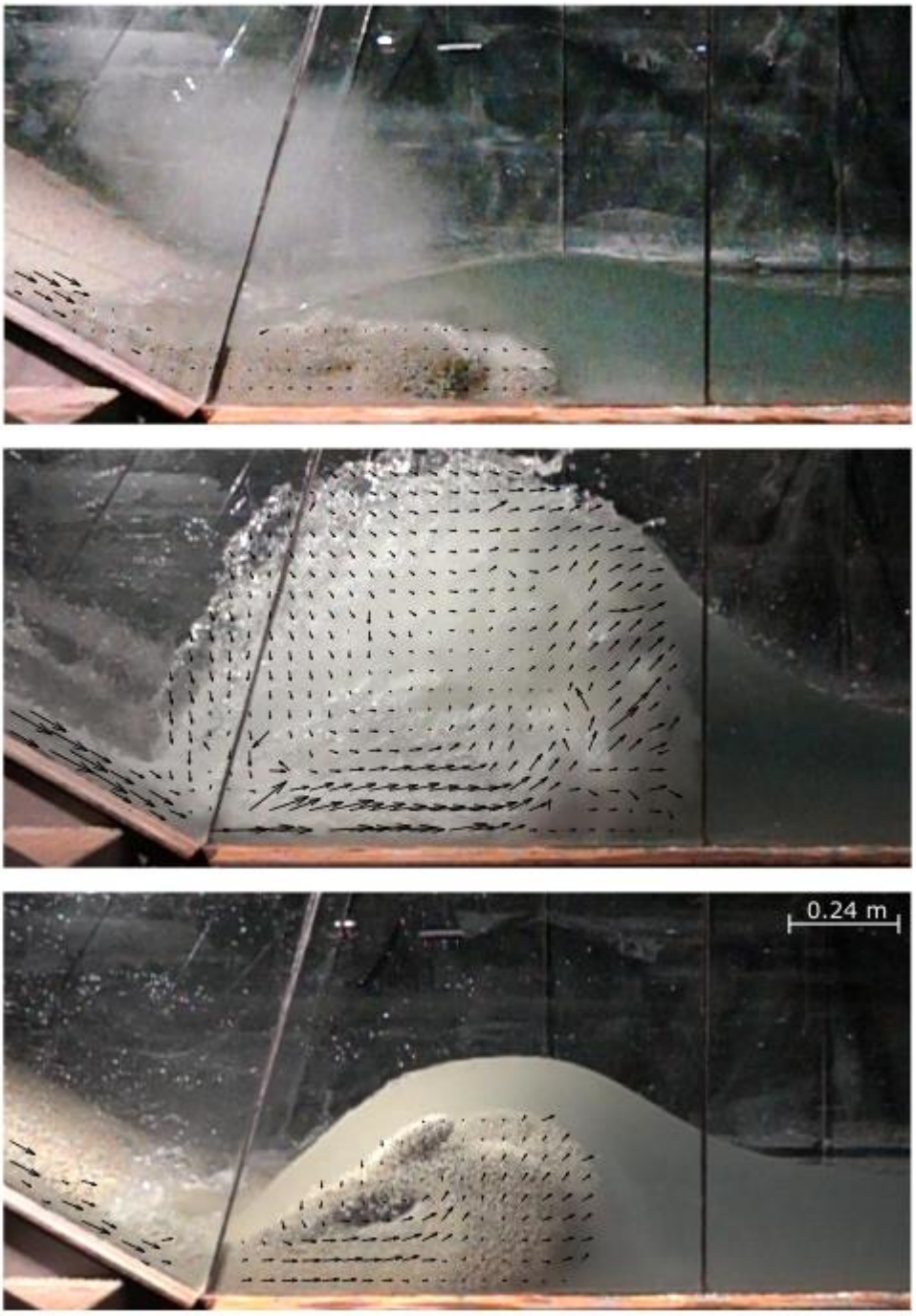

Figure 5.8: Comparison of the submerged particle motion at a similar x location for the dry granular (top), water (centre) and saturated granular (bottom) landslide types. The vectors indicate velocity obtained from PIV of particle displacement over Δt = 0.0156 s from Cam 4.

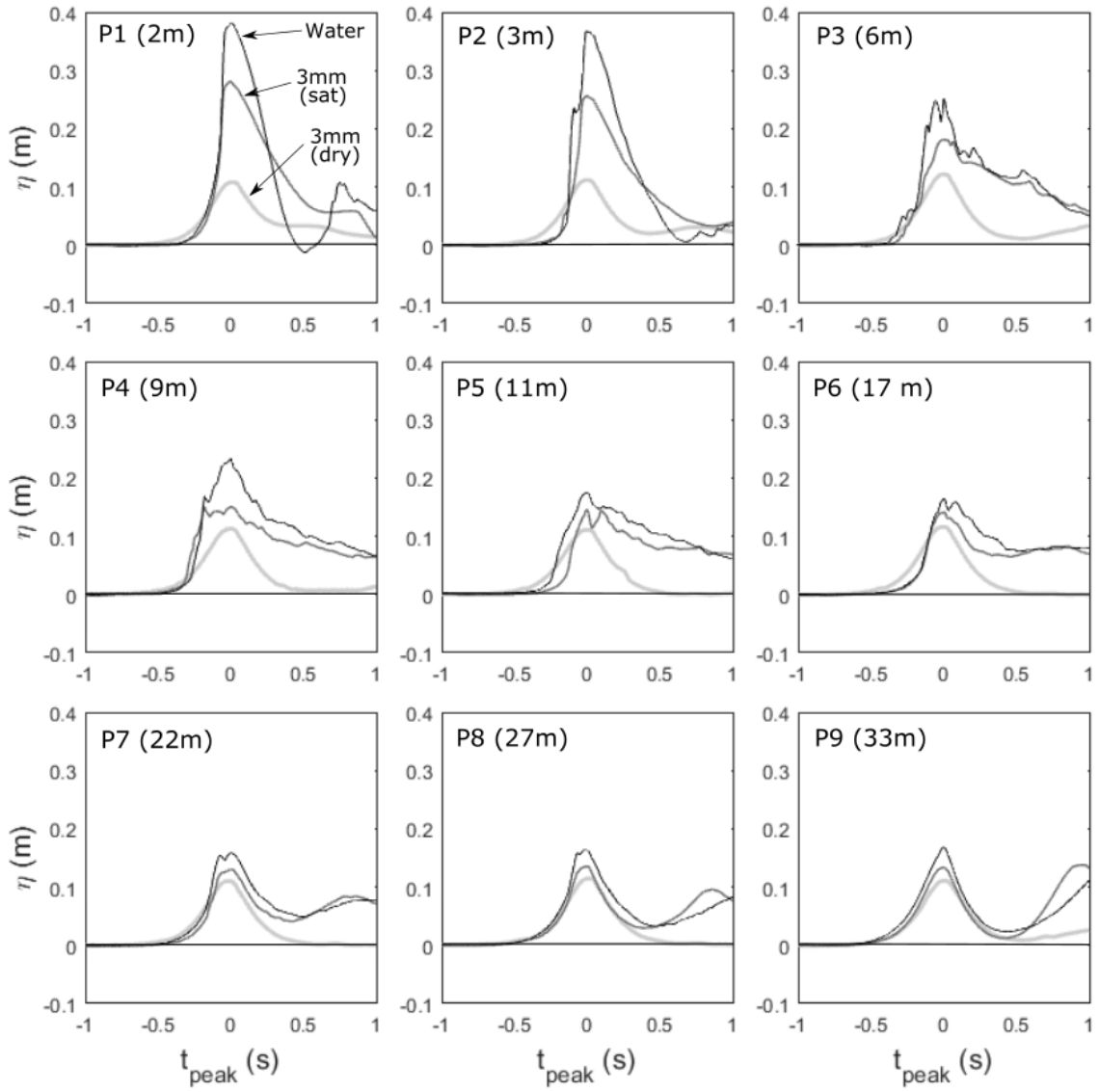

Figure 5.9: Water surface elevation profiles at wave probes for h = 0.2 m and V = 0.4 m^3 for each landslide type, indicating different wave shapes and amplitudes. The time has been adjusted such that t_{peak} = 0 s when the maximum water surface elevation passes each probe.

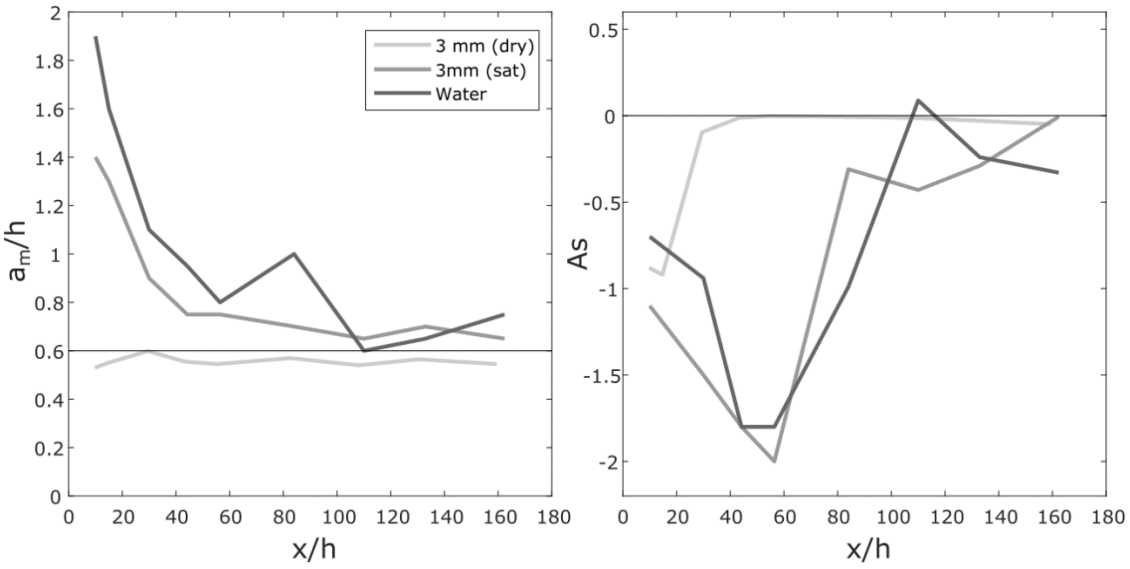

Figure 5.10: Relative maximum wave amplitude and wave asymmetry with relative distance for the three landslide types, for tests with V = 0.4 m^3 and h = 0.2 m. The solid thin black lines indicate the breaking limit of a_m/h = 0.6 (left) and perfect symmetry of As = 0 (right).

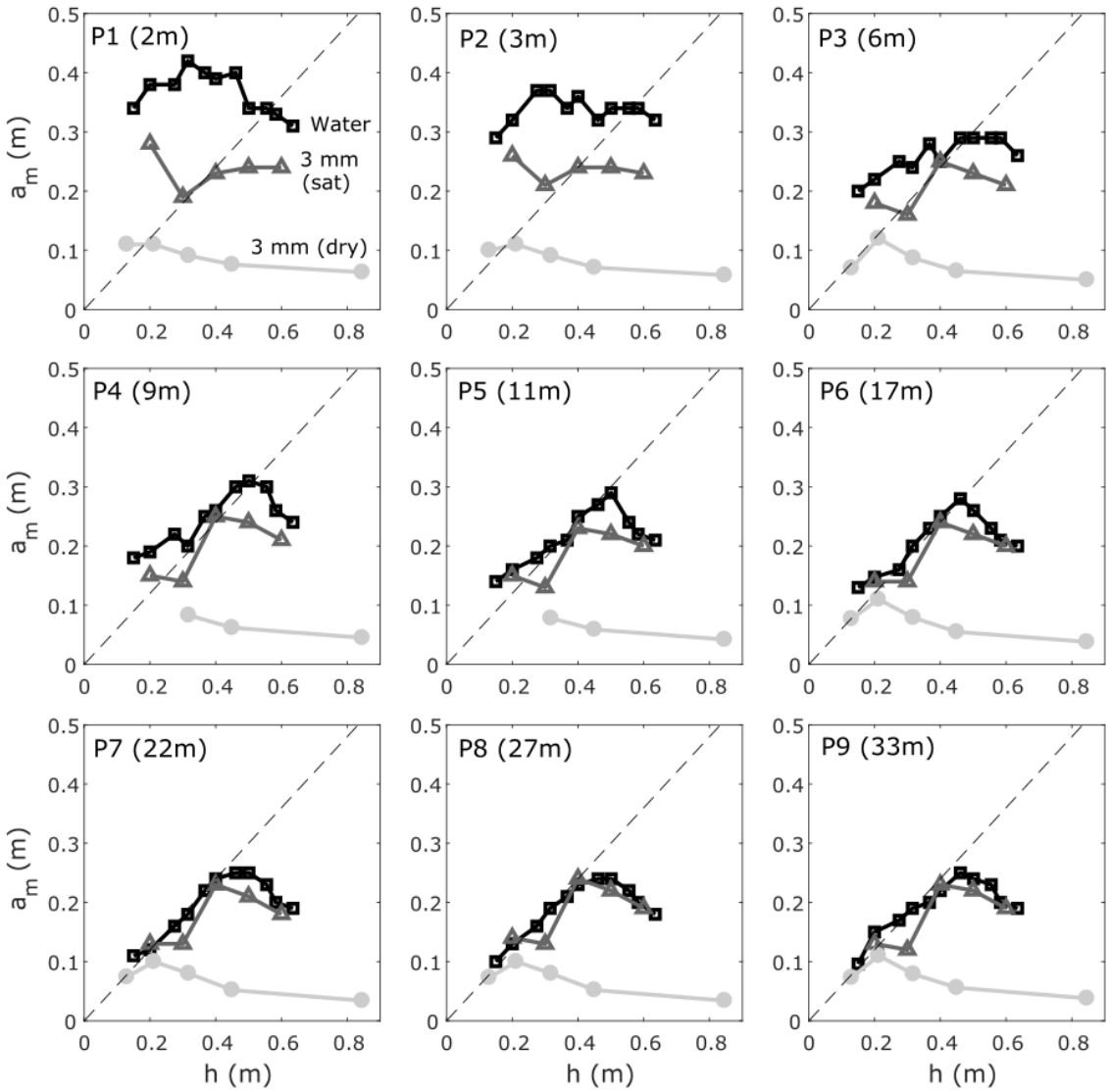

Figure 5.11: Variability in the maximum wave amplitude with water depth for the three different types of landslides. The source volumes are V = 0.40 m^3 for the highly mobile and saturated landslides and V = 0.34 m^3 for the dry granular flows, and the dashed line indicates a_m/h = 0.6.

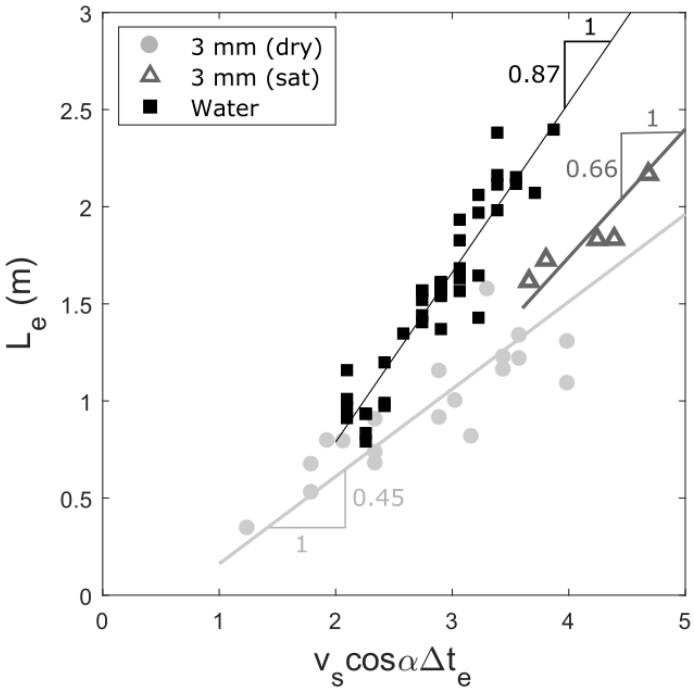

Figure 5.12: The effective length as a function of the horizontal component of velocity and the effective time, indicating linear trends with slopes that define the values of the mobility factor for each landslide type. The source volumes are V = 0.40 m^3 for the highly mobile and saturated flows and V = 0.34 m^3 for the dry granular flows.

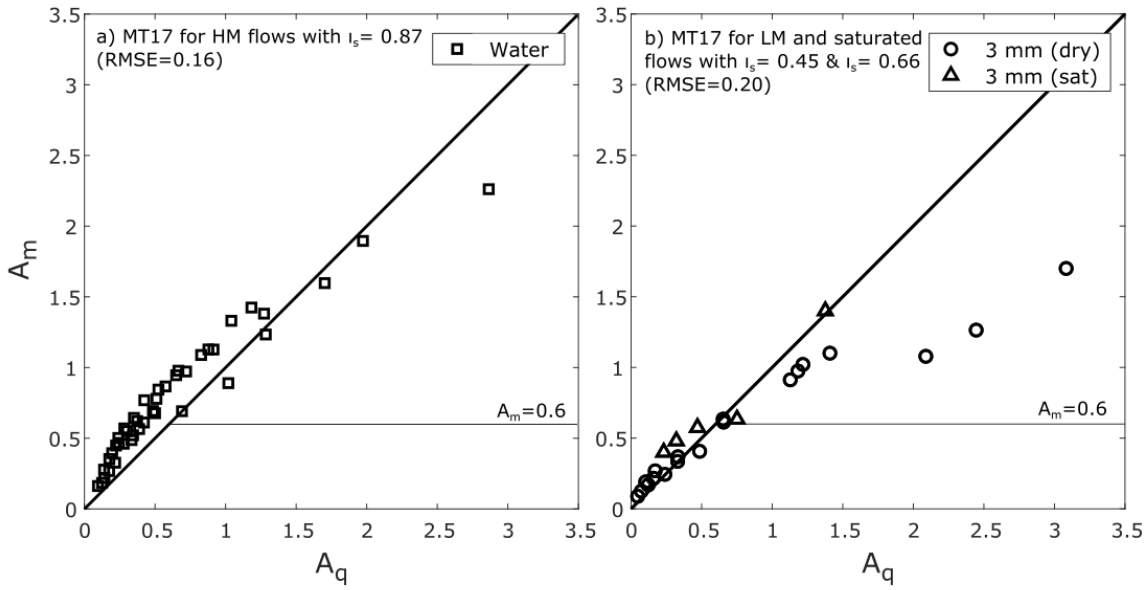

Figure 5.13: Observations of relative wave amplitude (A_m) at P1 (x = 1.9 m) compared to the estimated relative wave amplitude using the appropriate mobility factor (ι_s) for each landslide type (Eq. 5.3). Perfect correlation is indicated by the 1:1 line (thick line) and the wave breaking limit A_m = 0.6 is indicated by the thin horizontal line.

Chapter 6

Conclusion

6.1 Overview

The objective of this research was to utilize a large-scale 2D experimental flume to investigate the various processes of gravitationally accelerated landslides generating impulse waves. The initial wave generation process of three different landslide types were investigated in detail in the near-field and the wave propagation wave characteristics or amplitude and wave shape were quantified for all experiments. The following Chapter gives an outline of the key conclusions from each study as well as the overall impact and recommendations for future work.

6.2 Key Conclusions from Overall Work

6.2.1 Objective 1

The primary objective of Chapter 2 was to use water as a sliding mass, which gravitationally accelerates into a reservoir of varying depths to create a variety of impulse waves in a large-scale landslide flume. High-speed cameras were used from a side-view to measure the impact thickness and from the top-down to measure the overhead velocity in the centre of the flume. The average landslide thickness increases with each in source volume from 0.1-0.4 m^3. The use of water as the tsunami generator allowed for measurements of the bed velocity (z = 0.012 m) to be compared with changes in V and h using a Vectrino at x = 3.1 m. Nine wave probes ranging from distances of 1.9 m < x < 32.5 m determined that a_m/h = 0.6 distinguishes breaking from non-breaking waves and is also an upper bound on the far-field maximum wave amplitude. From the side-view camera, it is evident that water is much more mobile than any granular material previously studied and therefore it is not surprising that the predictive equations developed for granular material are all underestimating the size of the near-field maximum wave amplitude. Similar semi-empirical equations developed for positively buoyant material as well as a

momentum based equation, which both describe a_m in terms of a time of momentum transfer describing the length of forcing provide reasonable estimates.

6.2.2 Objective 2

The objective of Chapter 3 is to use the data obtained for Chapter 2 to devise a novel concept to quantify wave shape and use the nine probes to analyze the evolution of wave shape. Asymmetry has been applied to the wave shape measured at each of the nine wave probe locations using the 'zero-crossing' points, which has unveiled three distinct wave types: Negatively asymmetrical breaking waves, near-zero asymmetry solitary waves and positively asymmetrical deep water waves. Both near-zero asymmetry and positively asymmetrical waves slowly become close to $As = 0$ as they propagate with a very small change in a_m. Asymmetrical waves have a drastic change in wave shape, becoming more asymmetrical as they continue to break. Once $a_m/h \sim 0.6$, the waves become closer to the shape of a solitary wave and the amplitude does not change after this point. The distance each wave travels to reduce to be $a_m/h < 0.6$ and $As \sim 0$ has been quantified in order identify a zone in which different hydrodynamic properties such as: higher impact forces, increased sediment transport and increased orbital velocities can be expected. The influence of breaking waves can be captured using asymmetry to manipulate the solitary wave equation in order to account for the entire range in As that have been measured in this study. This provides an equation with inputs of a_m, h and As that will provide the entire wave shape in the near-field. Predictions of As have been quantified in terms of a_m and h to find a perfect correlation between $As = 0$ and $a_m/h = 0.6$ in the nearfield and also based on dimensionless parameters of the landslide.

6.2.3 Objective 3

The objective of Chapter 4 was to examine the applicability of the conclusions drawn from the highly mobile flows conducted in Chapter 2 to granular flows of varying volume. Similar to the highly mobile flows, the result of increasing the source volume from 0.34 m^3-1.4 m^3 on the impact parameters is increasing the average thickness. The length and time scales of forcing, which proved to be an important factor in the wave generation process, have been quantified for granular flows. A profile of the resulting

deposit shape indicates that increasing the source volume has a minor influence on the total runout and the location of the centre of mass. The wave shape has been quantified using asymmetry to find that there is not a correlation between $As = 0$ and $a_m/h = 0.6$ in the near-field. The As is rapidly changing in the near-field and may be influenced by the trailing waves. The wave breaking criterion of $a_m/h = 0.6$ does distinguish the breaking waves, which experience a rapid decrease in a_m, from the non-breaking waves in the near-field and provides an upper-bound on the far-field maximum wave amplitude. The previously developed semi-empirical and momentum based equations for granular material both provide an adequate estimate of the near-field maximum wave amplitude for the 19 tests conducted in this Chapter. The landslide mobility is quantified by a deceleration factor, which is related to the slope of the trend line describing the relationship between the length and time scales of forcing. This deceleration factor has a very large influence on the average maximum near-field wave amplitude.

6.2.4 Objective 4

Based on the previous findings, the objective of Chapter 5 is to examine the influence of mobility on the impulse waves by saturating granular flows in the expectation that it will provide a slide mobility in between the highly mobile and dry granular flows previously conducted in Chapter 2 and 4. The measured landslide characteristics indicate that the saturated flow impacts the reservoir at a similar velocity as the dry granular flow but the thickness is in between the LM and HM flows. An additional camera in the extreme near-field is used as a visual tool to examine the submerged behaviours of these three landslide types. The dry granular flow expands to form a bulbous front immediately after impact and begins to slow down rapidly. This produces a small wave, which is released from the landslide a short distance away from the impact. Comparatively, the HM flow also expands after impact at a much larger scale to turbulent ball, which extends from the base of the flume to the crest of the wave. The wave is much larger and asymmetric, and reaches the end of the field of view in a fraction of the time. The saturated granular flow produces a wave more similar wave to the HM flow in both size and shape. The saturated granular material traps air upon impact, which creates a pocket that changes in shape with the

submerged landslide. The bulbous front of the saturated granular flow is smaller than the HM flow and the wave reaches the end of the field of view at a time in between the LM and HM flows. A PIV analysis of the submerged particles highlights the similarities between the HM and saturated granular flow. Each flow displaces the slower moving particles at the front upwards, which creates the large bulbous front. The size of the displacement vectors can also be compared to see that these two more highly mobile flows slow down after impact much slower than the dry granular flow. The distinction between breaking and non-breaking waves holds true for the saturated granular flows with the saturated flows and the HM flows becoming more similar in a_m with increasing distance from impact. A linear relationship between the length of forcing and the time of wave release provides a 'deceleration factor', which can be applied to the momentum based equation for all three landslide types. The length and time scales of forcing for the saturated granular flows, as hypothesized, is in between the LM and HM flows. The momentum based equation can be applied to a range in landslide mobilities with reasonable accuracy to estimate the near-field maximum wave amplitude as long as there is an understanding of how fast the material will decelerate after impact.

6.3 Potential Impact

This study has provided data collected from a series of experimental tests, which has provided insight into the wave transition behaviour from the near-field to the far-filed. In smaller scale experimental studies, the varying behaviour from breaking to non-breaking waves has been attributed to 'scale effects' due to a very shallow water depth (Heller, 2011). The breaking limit of $a_m/h = 0.6$ has shown to apply for the 3 types of landslide generating waves, which propagate over a constant depth varying from $0.09\ \text{m} < h < 0.5\ \text{m}$. The wave breaking limit for impulse generated waves in a constant depth can be applied to future tests to test to validity in three-dimensions.

The wave shape has been quantified for impulse waves generated by a variety of landslides. All waves change shape to become closer to a symmetrical solitary wave with $a_m/h = 0.6$ and $As = 0$ in the far-field.

A rudimentary estimation on the distance each breaking wave requires in order to transform into a solitary wave can be used to indicate a ‘danger-zone’ for increased impact forces. The asymmetry can be used along with the near-field maximum amplitude to modify the solitary wave equation and be used as a boundary condition for numerical models. Numerical models can account for three-dimensional wave decay, changes in water depth, as well as wave refraction and diffraction specific to a certain site.

A reasonable estimate of the maximum near-field wave amplitude must be used as an input into the modified solitary wave equation. Despite the good correlation between the estimations from previously developed semi-empirical formulae to specific datasets, they cannot be applied to varying types of impacts due to differences in length and time scales. If a time scale is included, highly mobile slides can be analyzed similar to positively buoyant material. The momentum-based equation has shown more versatility to multiple types of impacts; however, it does rely on parameters that are difficult to quantify in the field (e.g length and time scales of forcing).

6.4 Recommendations for Future Work

The results from the current study have provided important advances in the study of landslide-generated tsunamis. This study has also unveiled some new questions and more uncertainty pertaining to the wave generation zone and can provide others data to validate numerical models.

6.4.1 Flume Facility

In order to increase the applicability of the momentum based equation to field cases, the deceleration factor relating the length of forcing and the time of forcing must be quantified. It is hypothesized that the deceleration factor is related to the porosity upon impact. The porosity can be changed by varying the saturation level of the source volume, using more widely graded particle size distribution, and varying the granular flow type from dense shearing flow to dilute collisional flow. Multiple tests conducted with the same experimental setup quantifying the porosity using a side-view high frame-rate camera for various volumes, bead sizes and saturation levels could provide more detail on the momentum transfer zone.

Field cases of landslides have a large variation in impact parameters. Thicker and slower moving flows can be used to expand the current prediction method for the near-field wave shape. This can be achieved using the same experimental method using the source volume box re-positioned to be farther down the slope.

6.4.2 Numerical

The immediate next steps from a numerical standpoint is to model the wave propagation along the entire length of the flume using a numerical model such as SWASH with an input from the modified solitary wave equation. These results can then be compared with the measured data from each of the wave probes to give an indication as to the effects of not including a trough in the model input. The entire dataset collected in this study can be used to validate numerical models describing the entire process of impulse-generated waves. The results from Chapter 2 specifically provide a very simple input, which does not have any internal shear. The use of numerical models will expand the applicability of this research to multiple areas and have the largest influence on increasing the accuracy of risk assessments in the future.

6.5 References

Heller, V. (2011). Scale effects in physical hydraulic engineering models. *Journal of Hydraulic Research*, *49*(3), 293-306.